Development of the Next Generation High-Sensitivity CdZnTe Imaging Gamma-Ray Spectrometer for Planetary Science Applications

by

Suzanne F. Nowicki

A dissertation submitted in partial fulfillment
of the requirements for the degree of
Doctor of Philosophy
(Applied Physics)
in The University of Michigan
2013

Doctoral Committee:

Professor Roy Clarke, Co-Chair
Ann Parsons, NASA, Co-Chair
Professor Timothy Chupp
Research Scientist Shaun Clarke
Stanley Hunter, NASA
Professor Çagliyan Kurdak

Baby Milo.

To My Grandparents

ACKNOWLEDGEMENTS

I owe sincere thankfulness to my research advisor, Dr. Ann Parsons, who gave me the amazing opportunity to be part of her team, here at NASA Goddard Space Flight Center. Ann has shown great support, understanding and encouragement. I would also like to show my gratitude to the rest of our team: Dr. Jeffrey Schweitzer, (almost Dr.) Julia Bodnarik, Dr. Tim McClanahan, Dr. Min Namkung, Dr. Richard Starr, Dr. Larry Evans, Samuel Floyd and Dr. Jacob Trombka.

This dissertation would not have been possible without the help, guidance and great knowledge of Dr. Stanley Hunter. I am thankful for his patience and for the great conversations I had with him (although in many cases, it lead to additional work). I would also like to thank the rest of the astrophysics team: Bert Nahory, William Daniels, Philip Goodwin, Dr. Seunghee Son, Dr. Mike Dion, Teresa Sheets and Dr. Georgia DeNolfo.

I would like to show my gratitude to my co-advisor and the director of the Applied Physics program at the University of Michigan, Prof. Clarke and Prof. Kurdak who made this Ph.D possible. I would also like to thank to other members of my committee, Prof. Chupp and Dr. Clarke.

It would not have been easy to assemble my laboratory computer and fix my laptop without the great help of Sandy Kramer and Sherry Hawkins. I would like to thank them for their help.

I want to thank my great friends, Steve and Sonya Wahi-Miller, who have been like a second family for me here. I am thankful to my other friends here at NASA

Goddard Space Flight Center, Nicolas Gorius, Valeria Cottini, Erwan Mazarico and Caroline Freissinet for their help, moral support and for the coffee breaks that kept me awake when needed.

I am greatful to Mona and her husband, Dominique, her daughter Wendy and her family who have welcomed me at their dinner table more times than I can count. The holidays would not have been the same without them.

Most importantly, I am so thankful for the love of my family. From across the Atlantic, they have shown support and encouragement throughout the years. My strength comes from them, especially from my mom, who has taught me to become independent like her and has been an example; my dad, my sister Yoanna, my cousin and her daughter, Myriam and Morgane, my other cousin and his family, Emmanuel, Sabrina and Salomé. You may be far away but you will always be close to my heart. My family is the most important thing in the world so I would like to also thank Henri, Irène, Eric, Carole, Ethan, Adélie and Yann; Michael, Yaël, Eliana and Joseph; Rémi, Maryse, Jean-Claude, Marie-Judith and Alice; Elizabeth, Stanislas, Mathilda and her family; Francis, Danielle and their family. Heuria and Aurélie, you are like my sisters, and I want to thank you for that. Burçin, Steve and I miss you. You are always welcome to our house.

Last but not least, I want to thank Stephen Anderson for his love and support. We have shared the past five years and a half together and there are many more to come. I know it is not always easy to put up with a French girl like me but you have managed to do it so well. Like you always say, we are stronger together.

I cannot finish this acknowledgement section without mentioning my wonderful furry dog Milo. “You’re a good boy Baby!”

Merci à tous!

TABLE OF CONTENTS

LIST OF FIGURES

Figure

LIST OF TABLES

Table

LIST OF APPENDICES

Appendix

LIST OF ABBREVIATIONS

3-DTI Three-Dimensional Track Imager

ADC analog-to-digital converter

AdEPT Advanced Energetic Pair Telescope

ASIC application-specific integrated circuit

BAT Burst Alert Telescope

CdZnTe cadmium zinc telluride

DA detector array

D-T deuterium-tellurium

DM detector module

FPGA field-programmable gate array

FWHM full width at half maximum

GGAO Goddard Geophysical and Astronomical Observatory

GRS gamma-ray spectrometer

GSFC Goddard Space Flight Center

HPGe high purity germanium

HV high voltage

ID inside diameter

IGS imaging gamma-ray spectrometer

IR infrared

LEND Lunar Exploration Neutron Detector

LAT Large Area Telescope

LRO Lunar Reconnaissance Orbiter

MCNP-PoliMi Monte Carlo N-Particle Polytechnic of Milan

MCNPX Monte Carlo N-Particle eXtended

MWD micro-well detector

NaI(Tl) sodium iodide dpped tellurium

OD outside diameter

PC personal computer

PCB printed circuit board

PNG pulsed neutron generator

PING Probing *In situ* with Neutrons and Gamma rays

PVC polyvinyl chloride

TIGRE Tracking and Imaging Gamma-Ray Experiment

TPC time projection chamber

USB Universal Serial Bus

ABSTRACT

Development of the Next Generation High-Sensitivity CdZnTe Imaging Gamma-Ray Spectrometer for Planetary Science Applications

by

Suzanne Nowicki

Chairs: Roy Clarke and Ann Parsons

The Probing *In situ* with Neutrons and Gamma-rays (PING) instrument, developed at NASA Goddard Space Flight Center (GSFC) by the neutron/gamma-ray group, is a technology used to determine the subsurface elemental composition of a planet. It uses a pulsed neutron generator to excite the solid materials of a planet and measures the resulting neutron and gamma-ray emissions with its detector system. A key objective of NASA is to develop instruments with reduced mass, volume and power consumption. The NASA GSFC neutron/gamma-ray group is currently developing the Imaging Gamma-Ray Spectrometer (IGS), the next generation light and compact high resolution and sensitivity instrument on PING. The spectroscopic and imaging performance of pixelated CdZnTe detectors as the innovative technology for IGS were investigated. This technology gives IGS the advantages of low mass and low power imaging with large field of view and high-resolution spectroscopy.

The spectroscopic performance of a large volume single crystal pixelated CdZnTe detector was studied by designing a detector box to readout a large volume of the detector. The crystal showed a single pixel energy resolution of 1.4% FWHM at

662 keV. However, above about 2 MeV, simulations have shown that the electron cloud formed in the detector becomes larger than the size of the pixel of the detector. Using digital system processing to read out the system, it is possible to calibrate the adjacent pixels responsible for cross talk and correct for incomplete charge collection.

Simulations have shown that with a pixel pitch of 1.72 mm, pixelated CdZnTe detectors have an angular resolution of 16° at 662 keV using backprojection reconstruction. A planetary science demonstration configuration was modeled and two methods were developed in this study to reject gamma rays from a source placed above the detectors using Compton imaging techniques: the full-energy Compton rejection method and the imaging ratio method. The second technique, the imaging ratio method, has shown that the gamma rays coming from the source placed above the detectors can be eliminated from the energy spectrum so that the residual is consistent with fluctuations in the background thus improving the sensitivity of the detectors to the gamma rays originating from the planet below.

Finally, this work has shown that pixelated CdZnTe detectors have the advantages of high-resolution spectroscopic performance, room-temperature operation thus eliminating the need for a cryogenic cooler, and Compton imaging capabilities to reject secondary gamma rays originating from the spacecraft or environment. Simulations have demonstrated that it is possible to reject a significant fraction of the gamma rays coming from a point source above the detectors thus increasing the sensitivity of the measurement to the planet surface below. Therefore, an array of pixelated CdZnTe detectors is a good candidate to meet the goals of reduced mass, volume and power consumption as imposed by the NASA requirements. However, the size of the electron cloud remains a problem at high energy and contributes to energy resolution degradation. In order to study the spectroscopic and imaging performance of pixelated CdZnTe detectors at high energy, it is necessary to increasing the detection volume of CdZnTe detectors. In the near future, we will receive an array of 2×2

pixelated CdZnTe detectors that we are going to 1) characterize using a monoenergetic beam of 6.129 MeV gamma rays at the 6 MeV Gamma Facility and 2) study at our test facility at GGAO in a planetary science demonstration configuration.

CHAPTER I

Introduction

To enable low-cost missions, planetary science has a critical need for miniaturized instruments with *in situ* sensors that can be deployed on surface landers, rovers and airborne platforms. A key objective of NASA is to develop instruments with reduced mass, volume and power consumption. The NASA Goddard Space Flight Center (GSFC) neutron/gamma-ray group is currently developing the Imaging Gamma-Ray Spectrometer (IGS), the next generation light and compact high resolution and sensitivity instrument. The IGS is developed as part of the Probing *In situ* with Neutrons and Gamma-rays (PING) Instrument. This technology, also developed at NASA GSFC by the neutron/gamma-ray group, uses a pulsed neutron generator to excite the solid materials of a planet and measures the resulting neutron and gamma-ray emission with its detector system. This technique is used to determine the elemental composition of a planet. The PING instrument is designed to land on the surface of a planet; however, due to its light weight and small volume and power consumption, the IGS can also be used on airborne platforms.

The innovative element of the IGS is the array of pixelated CdZnTe detectors that provides the advantages needed to reduce mass, volume and power consumption. The pixelated CdZnTe detector technology and advantages are presented in this chapter.

1.1 The Probing *In situ* with Neutrons and Gamma-rays (PING) Instrument

Current techniques do not allow the study of the bulk subsurface composition of any condensed body in the solar system unless a digging method is used. Fast neutrons have the ability to penetrate through various materials to large depths (on the order of 10 to 100 cm). Therefore, using fast neutrons as an excitation source to probe the surface of a planet or an object would remove the need to drill into the solid surface. Combining a pulsed neutron generator (PNG) with gamma-ray and neutron detectors is a technique that has been used for decades in oil well logging [22] as well as explosives detection [39]. However, we are working to adapt this technology to the geometry, power, mass and volume constraints imposed by space flight applications.

The main characteristics of three of the state-of-the-art gamma-ray spectrometers (GRSs) used for planerary exploration are summarized at the beginning of this chapter. The first one is the GRS on Lunar Prospector that orbited the Moon. The second one is the GRS on MESSENGER that is currently orbiting Mercury. Finally, the third one is the GRS on Dawn which is currently on its way to Ceres, the largest asteroid of the asterdoid belt. An introduction to PING which is under development at NASA/GSFC follows. The PING instrument is composed of three main components:

1) a Deuterium - Tritium (D-T) PNG that emits fast neutrons of 14.1 MeV to excite the materials at and below the planet or object's surface,

2) a gamma-ray spectrometer to measure the characteristic gamma rays from the excited elements and

3) neutron detectors to measure the properties of the resulting thermal and epithermal neutrons.

1.1.1 Gamma-Ray Instrumentation for Current and Past Missions

Specific objectives of the GRSs are to map abundances of O, Si, Fe, Ti, U, Th, K, Mg, Al, and Ca to depths of about 20 cm [19]. Gamma rays are produced in the surface of the body by the decay of long-lived radioactive elements and by cosmic ray interactions. When galactic cosmic rays collide with nuclei in the surface of the body, they produce a shower of energetic particles such as neutrons and protons. Neutrons are responsible for most of the gamma-ray production. The energy of these gamma rays is characteristic of each isotope with which the neutrons have interacted and the intensity of the gamma rays produced by nuclear reactions varies in proportion to the concentration of the elements and the flux of particles that cause the nuclear reactions. Analyzing the data acquired by the GRSs described below provides the energy and intensity of the gamma rays produced.

The characteristics of the GRSs of Lunar Prospector, MESSENGER and Dawn are presented in Table 1.1. It compares the detector type, energy resolution, volume and mass for each instrument. The anticoincidence shield is used to minimize spacecraft contribution to the response of the GRSs. Dawn is of particular interest for us because it uses a CdZnTe detector array thus increasing flight history of CdZnTe material. Because it is a new technology demonstration, it is coupled to a BGO detector that has a longer history in planetary science. It is important to notice that the energy resolution achieved with the Dawn CdZnTe array is not as good as the energy resolution achieved with pixelated CdZnTe detectors. The reason is that the CdZnTe array of Dawn uses coplanar CdZnTe detectors. It will be explained later in chapter IV how it is possible to achieve better energy resolution using pixelated CdZnTe detectors.

Table 1.1: Lunar Prospector, MESSENGER and Dawn GRS's characteristics

	Lunar Prospector	MESSENGER	Dawn
Detector type	BGO	N-type coaxial Ge detector	Coplanar CdZnTe array mounted on top of BGO
Detector size	7.1 cm diameter × 7.6 cm length	5 cm diameter × 5 cm length	BGO: 7.6 cm wide × 7.6 cm long × 5 cm thick - CdZnTe: 4 × 4 detector array of 0.75 cm^3 unit (12 cm^3 total)
FWHM energy resolution	10.5 % at 662 keV	0.26 % at 1332 keV	2.7 % and 10.5 % at 662 keV for CdZnTe and BGO, respectively
Anticoincidence shield	borated-plastic sintillator	borated-plastic sintillator	borated-plastic sintillator
Instrument mass (kg)	8.6	9.2	10
Power consumption (W)	3	23	9

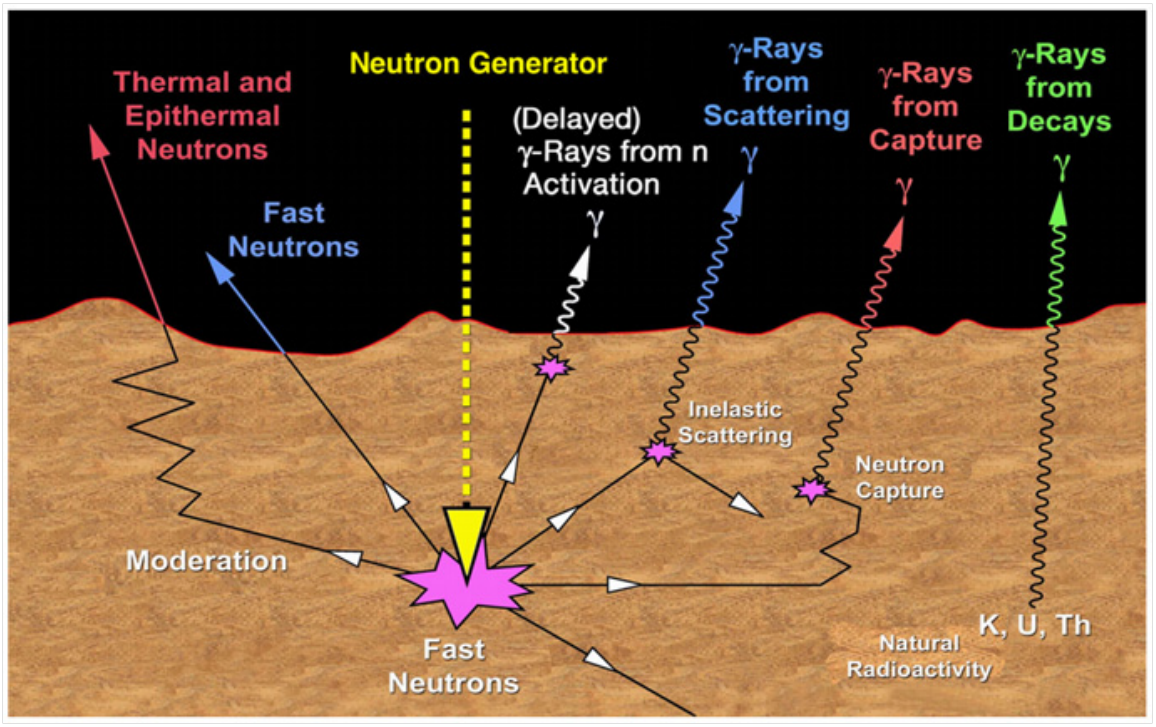

Figure 1.1: Example of the different types of interactions that can be undergone by neutrons [34].

1.1.2 The PNG

The D-T PNG emits fast neutrons of 14.1 MeV at a rate up to 10^8 n/s to excite the materials at and below the planet or object's surface. As will be described in more detail in Chapter II, neutrons can undergo several types of interactions, some of them resulting in the emission of gamma rays and/or neutrons as illustrated in Fig. 1.1. Gamma rays and neutrons are then recorded using gamma-ray and neutron detectors and spectra are analysed to determine the elemental composition of the surface of planets. Results from previous work undertaken at NASA GSFC using PING can be found literature [34].

1.1.3 The Gamma-Ray Detectors

By measuring the gamma-ray energies and area under the peak of the gamma-ray lines that are produced by the different types of reactions illustrated in Figure 1.1, it is possible to study the bulk subsurface composition of the soil. The energy resolution of the gamma-ray spectrometer is therefore a key to identifying each element present in the spectrum and measuring with accuracy their abundances. Figure 1.2 shows the elements (in red and blue) from the periodic table that can be detected by measuring the characteristic gamma-rays. In red are the natural radioactive elements and in blue are the elements that will become radioactive if excited by high-energy neutrons.

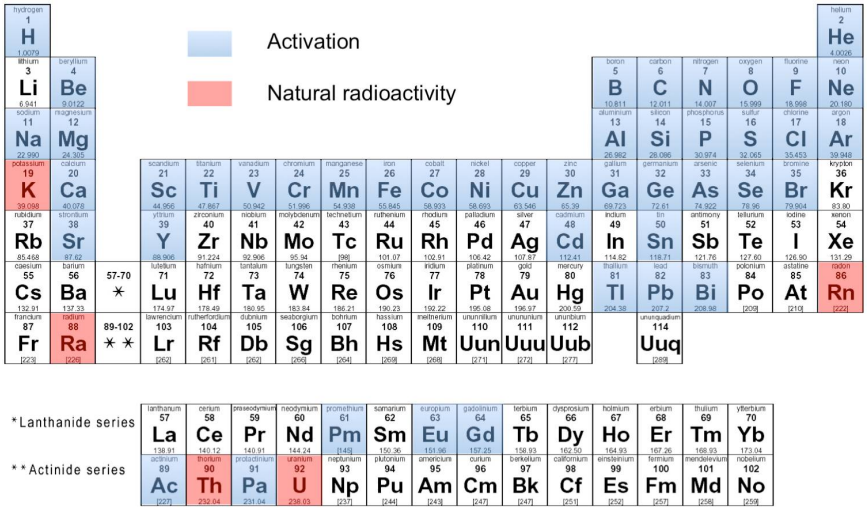

Figure 1.2: Elements from the periodic table that can be detected using PING.

1.1.4 The Neutron Detectors

Neutron detectors on PING are used in a similar manner that they are used in Lunar Exploration Neutron Detector (LEND) on Lunar Reconnaissance Orbiter (LRO) [29]. High-energy neutrons penetrating in the soil are slowed down and absorbed by nuclei of elements in the soil. Some of the neutrons that are not captured by the soil escape, creating a leakage flux of neutrons. The distribution of neutron energies is a measurement of how much they were slowed down before escaping. This distribution

depends on the composition of the soil and mostly on the content of hydrogen. The hydrogen content can be related to water. The neutron detectors are used to measure the thermal and epithermal neutron distributions. It is possible with the measurements provided by LEND on LRO to determine the areas with low level of epithermal neutrons which signals more hydrogen and give the scientists the possibility to look for deposits of water ice on the Moon [29].

1.2 The Imaging Gamma-Ray Spectrometer

The IGS is the next generation compact high-sensitivity gamma-ray imaging spectrometer used as the gamma-ray detector for PING. The innovative technology for IGS is the pixelated CdZnTe detector. This technology gives IGS the advantages of low-mass and low-power imaging with large field-of-view and high-resolution spectroscopy. These advantages are obtained:

1) at room temperature, thus eliminating the need for a cryogenic cooler,

2) without an anticoincidence shield to reduce the background, and

3) without a collimator to reject secondary gamma rays from the spacecraft or environment.

Eliminating the need for cryogenic cooler, anticoincidence shield, and collimator further reduces the overall instrument cost, mass, volume, and power.

1.2.1 Advantages of Pixelated CdZnTe Detectors

Pixelated CdZnTe detectors have three main advantages:

1) high density (5.86 g/cm^3) resulting in high stopping power. As shown in Figure 1.3, the photon cross sections for Compton scattering, photoelectric absorption and pair production for CdZnTe are higher than in Ge.

2) high energy resolution at room-temperature operation. CdZnTe has a wide bandgap (1.6 eV) that results in low probability of thermal excitation of electrons

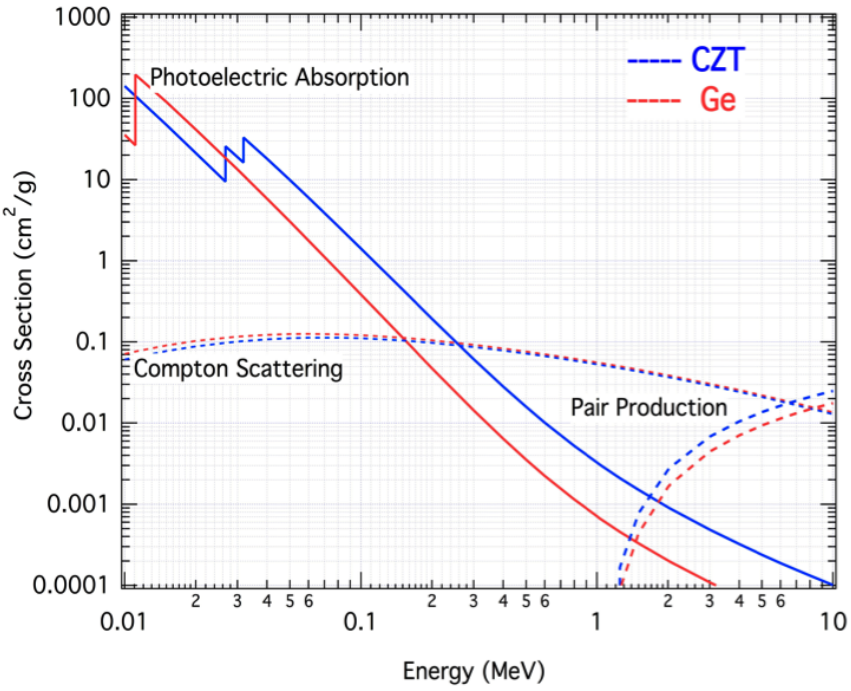

Figure 1.3: Photon cross sections for Compon scattering, photoelectric absorption and pair production comparison for CdZnTe and Ge.

from the valance band to the conduction band at room temperature and results in very good energy resolution (about 0.5% FWHM at 662 keV). Better energy resolution can be achieved with high purity germanium (HPGe), which has a narrower bandgap (0.7 eV), but requires the use of cryogenic cooling to reduce the thermal excitation. Figure 1.4 compares the response of NaI(Tl), HPGe and pixelated CdZnTe detector to a ^{137}Cs source and shows that the energy resolution of CdZnTe approaches that of HPGe. However, the mass, volume and power of a CdZnTe instrument will be reduced since it does not require the cryogenic system or background shielding needed for HPGe.

3) gamma-ray imaging using Compton scattering. The anode of the CdZnTe detector is pixelated with an 11 $\times$ 11 array of pixels and the cathode on the opposite side of the detector is planar as shown in Figure 1.5. The x and y coordinates of each gamma ray interaction is determined by the pixel coordinates under which the interaction occurs. The z coordinate is determined by the cathode to anode

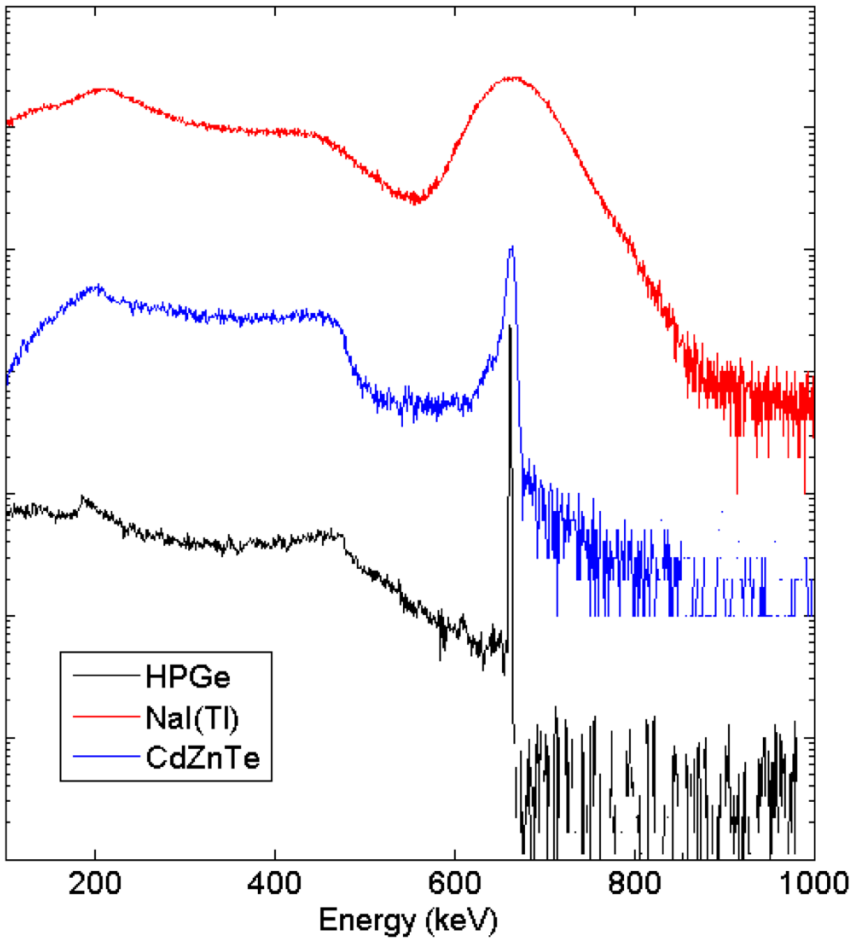

Figure 1.4: NaI(Tl), HPGe and pixelated CdZnTe detector response to a ^{137}Cs source.

amplitude ratio or by electron drift timing measurements. By locating the interaction in 3D inside the detector, Compton imaging techniques can be used to determine the incident direction of gamma rays without the need for a heavy collimator to eliminate background. Thin CdZnTe detectors with planar electrodes on each side of the crystals are used in the Swift-BAT instrument [4]. However, the use of a coded aperture mask is used to image gamma rays in the 20 - 200 keV energy range. Pixelated detectors provide imaging capabilities to CdZnTe detectors eliminating the need for a heavy coded aperture mask.

Figure 1.5 illustrates a two-interaction event in a CdZnTe detector. The sequence shows a Compton scattering followed by a photoelectric event. By measuring the

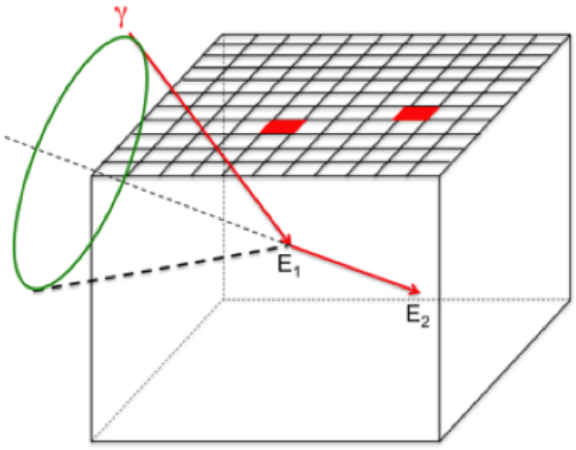

Figure 1.5: Compton scattering followed by a photoelectric event in a CdZnTe detector. The Compton scattering formula can be used to restrict the direction of the initial gamma ray to the surface of a cone.

3D locations and energies of the Compton and photoelectrons in the detector, the Compton scattering formula can be used to restrict the direction of the initial gamma ray to the surface of a cone. The cones for multiple events will overlap and give a probability distribution for the location of the gamma-ray source. Pixelated CdZnTe detectors thus form a high-resolution imager.

The penetrating nature of gamma rays allows for investigations below the surface or behind foreground material at depths of about 30 to 50 cm. Therefore, gamma-ray spectroscopy and imaging capabilities provided by pixelated CdZnTe detectors allow one to investigate the elemental composition and mapping of a material about 10^3 order of magnitude deeper than infrared (IR) or x-ray instruments. Furthermore, having a spectrometer that works at room temperature advance the current state of the art technologies (such as HPGe detectors) and will place GSFC in a better position to win future instrument proposals.

1.2.2 Thesis Scope

Pixelated CdZnTe detectors give IGS the advantages of low mass and low power imaging with large field of view and high-resolution spectroscopy. These advantages

are obtained at room temperature thus eliminating the need for a cryogenic cooler, without an anticoincidence shield to reduce the background, and without a collimator to reject secondary gamma rays from the spacecraft or environment. Indeed, with their pixelated arrays, CdZnTe detectors can identify tracks left by charged particles and use Compton imaging techniques to distinguish gamma rays coming from above, from the spacecraft for example, to those coming from below, from the planet.

It is necessary for planetary exploration to detect elements such as oxygen. Neutron activation on oxygen results in the production of a 6.129 MeV gamma-ray line with 67% probability. In order to characterize and calibrate the IGS at this energy, which is a region where there is a lack of gamma-ray sources, we designed and built the NASA GSFC 6 MeV Gamma Facility. The facility uses neutron absorption on oxygen to provide a quasi-monoenergetic source of 2.742, 6.129 and 7.117 MeV gamma rays suitable for characterization and optimization of a wide range of gamma-ray instruments for planetary science and imaging telescopes for astrophysics. Comparison to a ^{238}Pu/^{13}C source with similar 6.129 MeV gamma-ray rate shows that the 6 MeV Gamma Facility has a reduced low-energy gamma-ray continuum by a factor of 30 and a 6.129 MeV gamma-ray rate 100 times higher.

The spectroscopic performance of a large volume single crystal pixelated CdZnTe detector was studied by designing a detector box to readout a large volume of the detector. A digitizer system with 24 channels was put together to readout the system. It is capable to digitize each preamplifier output at a rate of up to 100 MHz. The spectroscopic performance of the crystal was studied with a source of ^{137}Cs. However, above 2 MeV simulations have shown that the electron cloud formed in the detector becomes larger than the size of the pixel and is collected by multiple pixels. This effect is also known as charge sharing effect. Due to the weighting potential cross talk on the adjacent pixels, the spectroscopic performance of the detector is reduced. Using digital system processing to readout the system, it is possible to calibrate the

adjacent pixels responsible for cross talk and correct for incomplete charge collection.

The Doppler effect, the energy and position resolution of pixelated CdZnTe detectors are contributing factors to the angular resolution of the detectors. These effects were studied. Simulations were undertaken to measure the angular resolution of pixelated CdZnTe detectors at 662 keV with a 1.72 mm and 3.44 mm pixel pitch using backprojection reconstruction. A planetary science demonstration configuration was modeled and Compton imaging techniques were used to reject gamma rays from a source placed above the detectors using full-energy Compton rejection method and imaging ratio method.

CHAPTER II

Theory

In situ planetary science exploration requires the use of penetrating radiation to probe the surface and subsurface of a planet or an object in order to remove the need to drill into the solid surface. In PING, fast neutrons are used as an excitation source to probe the surface. Neutrons can undergo several types of interactions, some of them resulting in the emission of gamma rays and/or neutrons. The first part of this chapter introduces three important neutron reaction types: radiative capture, elastic scattering reactions and inelastic scattering reactions. The second part of this chapter presents the modes of interactions of gamma rays with matter. Gamma rays can interact through three major ways: photoelectric effect, Compton scattering and pair production. The last two processes can be used in pixelated detectors to image the direction of incoming gamma-rays. An introduction to Compton and pair production imaging techniques is given in this chapter.

2.1 Neutron Interactions

Penetrating radiation such as gamma rays and high-energy neutrons provide a way to probe below the microscopic layer that is available to x-ray and IR instruments without digging the surface. Indeed, because neutrons carry no charge, they can easily interact with the nucleus of an atom. A neutron can undergo many types

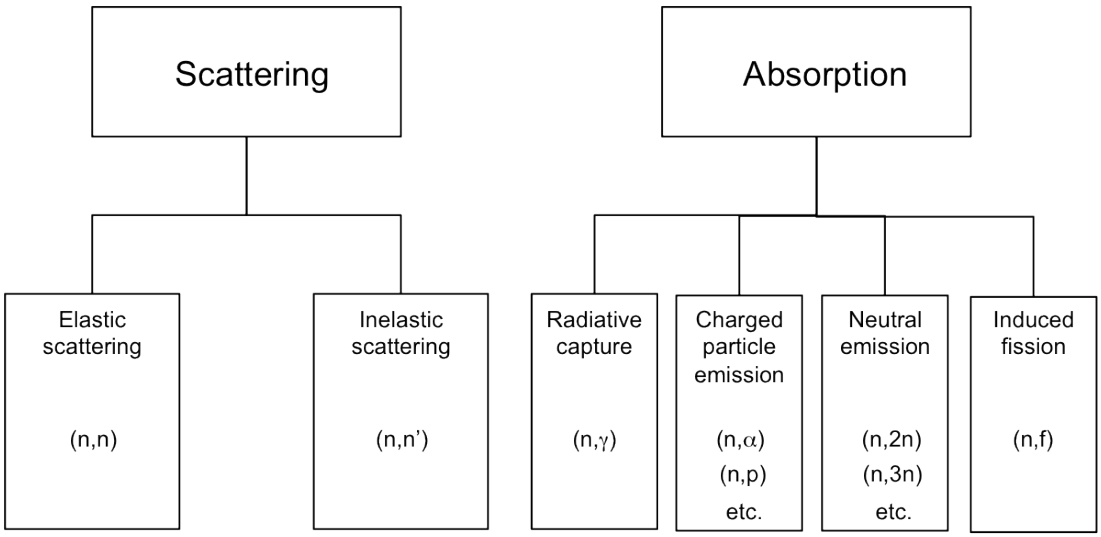

Figure 2.1: Neutron interaction types.

of interactions and can travel many centimeters of a material before it interacts. Figure 2.1 shows the important reactions that a neutron can undergo in matter. For this work, we will not consider the case of neutron induced fission because the materials studied here do not contain any elements with Z higher than 100.

Here, we are interested in the neutron reactions that lead to gamma-ray emission. We will first discuss the case of radiative capture. As described in Chapter I, the PING instrument includes a D-T neutron generator that emits neutrons with energy of approximately 14.1 MeV. The cross section for radiative capture increases with decreasing neutron energy. It is most likely that the neutrons emitted from the PNG will undergo several scatters before they get captured. Elastic scattering will be the subject of the second part of this subchapter. Inelastic scattering involves the excitation of nuclear levels and can also lead to the emission of gamma rays. Inelastic scattering will be discussed at the end of this subchapter.

2.1.1 Radiative Capture

In radiative capture, the neutron is absorbed by the nucleus. During the absorption, the nucleus rearranges its structure and the emission of a gamma ray follows.

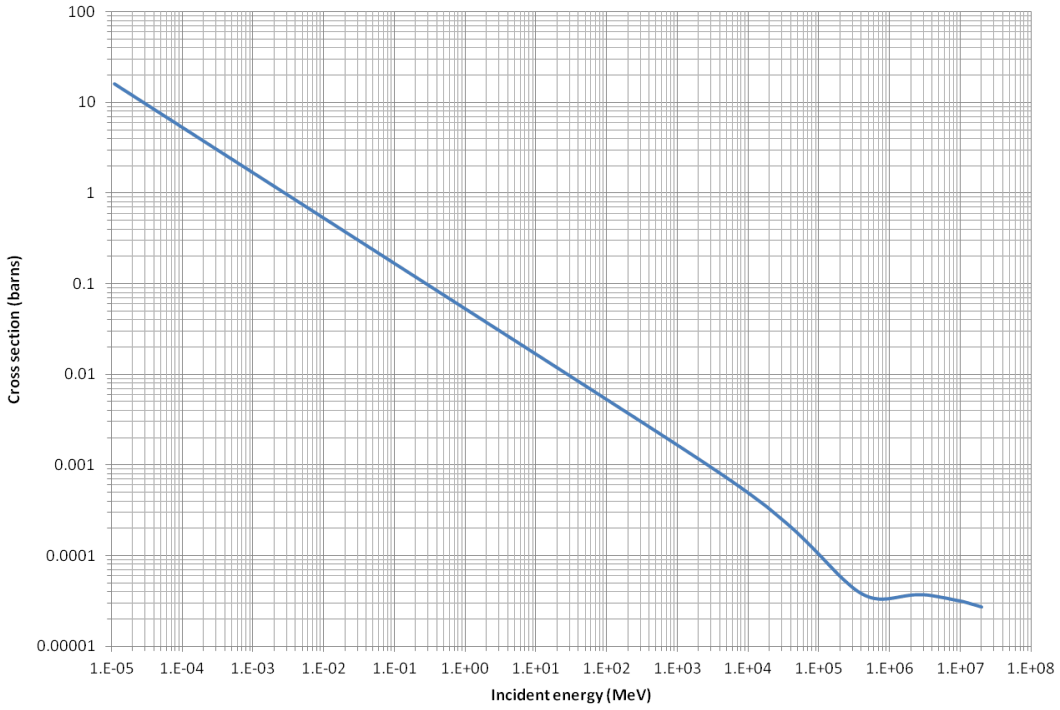

Figure 2.2: Radiative capture cross section for H. [10]

One of the most important elements to detect in planetary science is hydrogen. The radiative capture cross section of H as a function of the incident neutron energy is shown in Figure 2.2 [10]. The cross section increases as the energy of the neutron decreases. If the neutron energy is high, for example 14.1 MeV in the case of a D-T neutron generator, the neutron loses energy by scattering several times before being captured by hydrogen. The energy of the gamma ray emitted by this reaction is about 2223 keV.

2.1.2 Elastic Scattering

During the interaction, a fraction or all of the energy of the neutron is transferred to the target nucleus. The neutron and the target nucleus are deflected with angle θ and α, respectively. An illustration of an elastic scattering event is shown in Figure 2.3.

We have seen that the cross section of radiative capture increases with decreasing

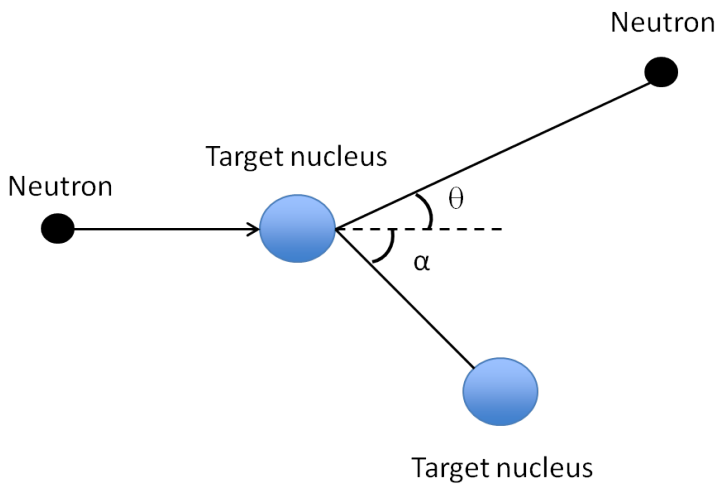

Figure 2.3: Illustration of an elastic scattering event.

neutron energy. In PING, the initial neutron energy emitted by the PNG is 14.1 MeV. Therefore, the neutron will lose energy by scattering several times before being captured. Using the kinematics of elastic scattering, it is possible to calculate the number of collisions undergone by a neutron before reaching 0.025 eV, also referred to as thermal energy, at which a radiative capture is most likely to happen. It can be shown that for a neutron of energy E, the average energy loss after one collision is:

$$\langle E_{loss} \rangle = \frac{2EA}{(A+1)^2} \tag{2.1}$$

For hydrogen A=1, the average energy loss is equal to $E/2$. In general, for a neutron with initial energy E_0, after n collisions the energy of the neutron becomes:

$$E_n = E_0 \left[\frac{A^2+1}{(A+1)^2} \right]^n \tag{2.2}$$

The number of collisions required for a neutron with initial energy E_0 to reach an energy E_n is:

$$n = \frac{ln\left(\frac{E_n}{E_0}\right)}{ln\left(\frac{A^2+1}{(A+1)^2}\right)} \tag{2.3}$$

From this equation and for a neutron of 14.1 MeV, an average of 30 collisions is required to reach an energy of 0.025 eV (thermal neutron) on H (A=1). Therefore, the time at which the gamma rays from radiative capture will be emitted will depend on the time it takes the neutrons to undergo enough collisions to reach a sufficiently low energy to be captured. On the contrary, gamma rays issued from inelastic scattering, as will be described in the next section, are promptly emitted, on average a few ps after the emission of the 14.1 MeV neutron from the PNG. When studying the complex composition of materials such as granite for example, it is useful to separate the inelastic reactions from the capure reactions by time because the likelihood of an overlap between two peaks or more is reduced. Techniques have been developed in order to acquire gamma-ray spectra at different times during a neutron pulse period [34]. Figure 2.4 shows different gamma-ray acquisition time windows and the main reactions that occur during these time windows. A characteristic HPGe spectrum is shown as an example for two different acquisition windows in order to illustrate the different gamma-ray lines observed during these time windows.

2.1.3 Inelastic Scattering

In the case of inelastic scattering, the conservation of kinetic energy does not apply anymore. When the neutron collides with the nucleus, the nucleus undergoes an internal rearrangement into an excited state from which it eventually releases radiation. The average energy loss is no longer an easy expression to write because the energy levels of the target nucleus are involved. If the incoming neutron does

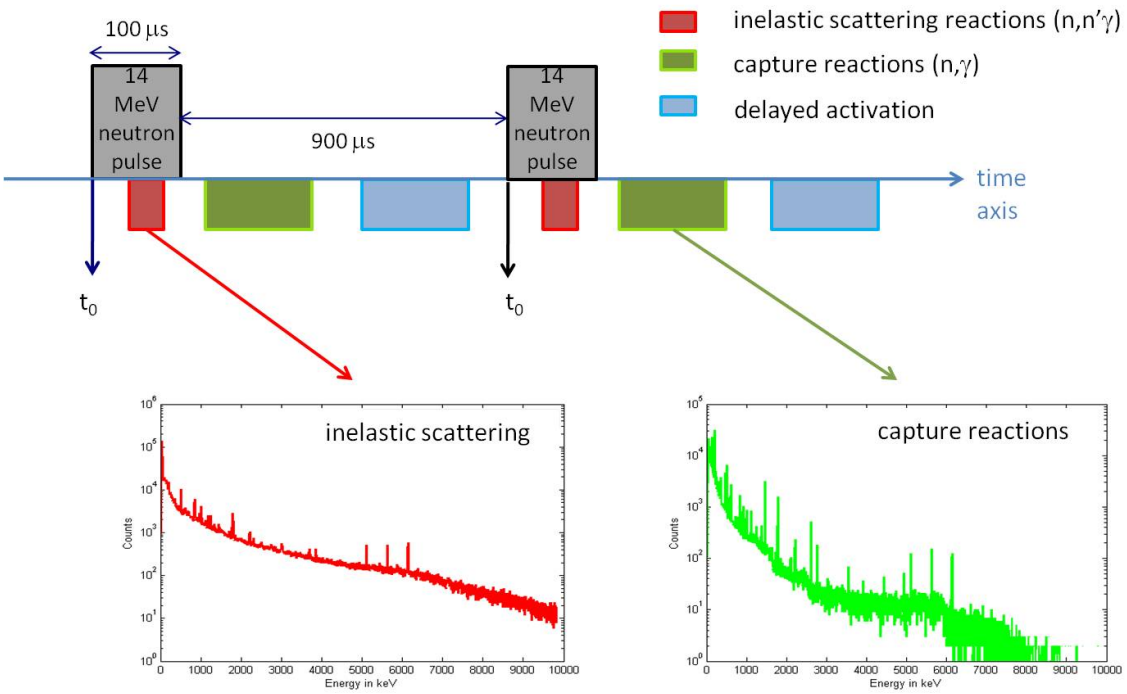

Figure 2.4: Example of PNG time configuration and gamma-ray time acquisition windows.

not provide sufficient energy to reach the energy level of the excited states, inelastic scattering is impossible. The hydrogen nucleus does not have excited states, so only elastic scattering or neutron capture reactions can take place.

2.2 Gamma-Ray Interactions

2.2.1 Cross sections

Figure 2.5 shows the photon cross sections in CdZnTe material. Below about 300 keV, the photoelectric effect is dominant. Between 300 keV and about 6 MeV, Compton scattering is the dominant process. Above 7 MeV, pair production becomes the main process in CdZnTe.

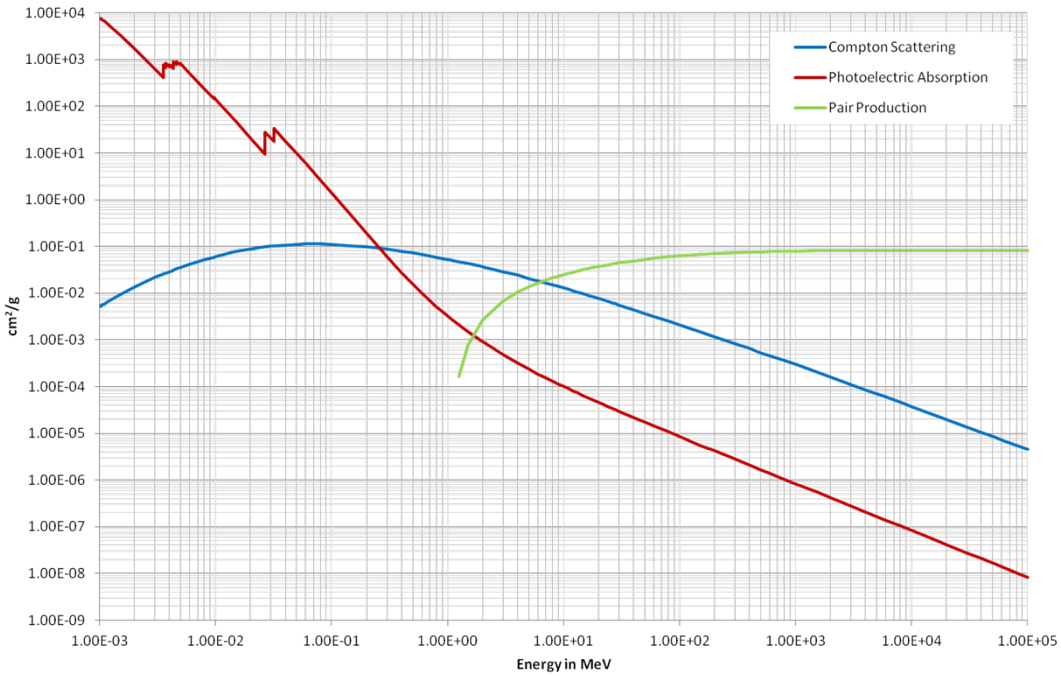

Figure 2.5: Photon cross sections in CdZnTe material. [30]

2.2.2 Photoelectric Effect

In the photoelectric effect, a photon of energy $h\nu$ interacts with an electron of an absorber atom and is absorbed. The photoelectron is ejected from its bound shell with an energy:

$$E_e = h\nu - B_e \tag{2.4}$$

where B_e is the binding energy of the ejected electron. Total absorption can only take place if the electron is bound to an atom [18]. Therefore, the most tightly bound electrons have the greatest probability of absorbing a photon which is incident upon an atom. The ejection of the photoelectron creates a vacancy in an inner shell that is filled through capture of free electrons from the medium or from the rearrangement of the atom and a characteristic x-ray is emitted. Characteristic x-rays can also undergo absorption before leaving the atom. In this case, an Auger electron is released from

the atom with an energy equal to the difference between the x-ray energy and the binding energy of the electron.

2.2.3 Compton Scattering

In Compton scattering, the gamma-ray photon interacts with an electron of the matter and is deflected through an angle θ with respect to its original direction as illustrated in Figure 2.6. Using the laws of conservation of energy and momentum, one can show that:

$$h\nu' = \frac{h\nu}{1 + \frac{h\nu}{m_e c^2}(1 - cos\theta)} \tag{2.5}$$

where $m_e c^2$ is the rest-mass energy of the electron (0.511 MeV).

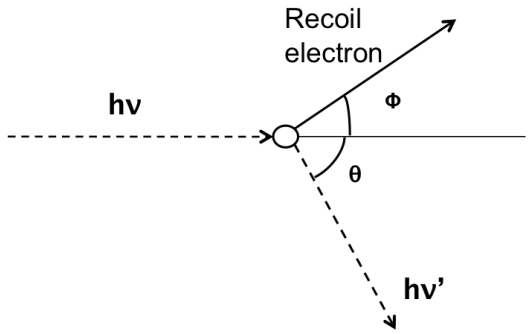

Figure 2.6: Illustration of a Compton scattering event.

2.2.3.1 Compton Imaging

If the scattered photon undergoes a photoelectric effect and the positions and the energies of the two consecutive interactions are known, the position of the photon from the source can be limited to the surface of a cone as illustrated in Figure 2.7. By looking at the overlap location of multiple cones, one can determine the direction

of the source photon. This technique is used with pixelated CdZnTe detectors to determine the direction of gamma-ray sources.

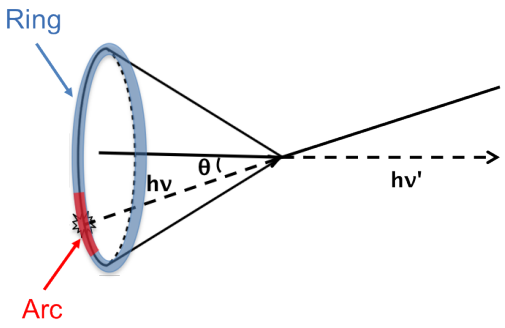

Figure 2.7: Illustration of a backprojection cone in a Compton scattering event. The cone can be measured if the interaction locations and energy of the source and scattered photons are known.

Another technique consists to track and measure the energy losses of Compton recoil electrons and combine it with the direction and energy of the Compton scattered gamma ray. This way, the incident direction of each photon is determined. Due to the uncertainty in the track of the recoil electron and the energy of the scatterd photon, there is an uncertainty in the caculated angle theta. Therefore, the position of each photon is limited to the surface of an arc as shown in Figure 2.7. This technique results in an improved sensitivity compared to the traditional Compton ring camera techniques. An example of such a Compton camera is the Tracking and Imaging Gamma Ray Experiment (TIGRE) that uses multi-layers of thin silicon to measure the energy losses of Compton recoil electrons and a CsI detector to measure the energy of the Compton scattered gamma rays [7].

2.2.4 Pair Production

Above incident photon energies of twice the rest-mass energy of an electron (1.02 MeV), pair production becomes increasingly important. In a pair production event, the photon is completely absorbed and is replaced by an electron-positron pair whose total energy is equal to the initial energy $h\nu$ of the photon:

$$h\nu = E_- + m_e c^2 + E_+ + m_e c^2 \tag{2.6}$$

where E_- and E_+ are the kinetic energies of the electron and the positron respectively, and $m_e c^2$ is the rest-mass energy of the electron. The pair production process can occur in the nuclear field but also in the electron field. In the latter case, the effect is also known as the triplet production because in addition to the creation of an electron-positron pair, an electron is ejected from the atom. From the conservation of energy and momentum, it can be shown that the threshold energy of the photon is:

$$k_t = 2\left(1 + \frac{m_e}{m_r}\right) m_e c^2 \tag{2.7}$$

where k_t is the minimum energy of the photon, m_e and m_r are the masses of the electron and the target, respectively. Therefore, in the case of a pair production occuring in the nuclear field ($m_e \ll m_r$), the minimum photon energy is $2m_e c^2$ and in the case of a pair production in the electron field (m_e=m_r), the minimum energy of the photon is $4m_e c^2$. If pair production occurs in the field of the nucleus, due to the heavy mass of the nucleus compared to the photon, the momentum transferred to the nucleus is very difficult to measure. On the contrary, if pair production occurs in the field of the electron, it is possible to measure the momentum transferred to the electron. Therefore, if pair production in the field of the electron occurs and the three momenta of the electrons and the positron are measured, it is possible to reconstruct the direction of the incoming photon.

In order to understand if it is possible to use pixelated CdZnTe detectors to track the electron positron from a pair prodution event, the energy distribution between

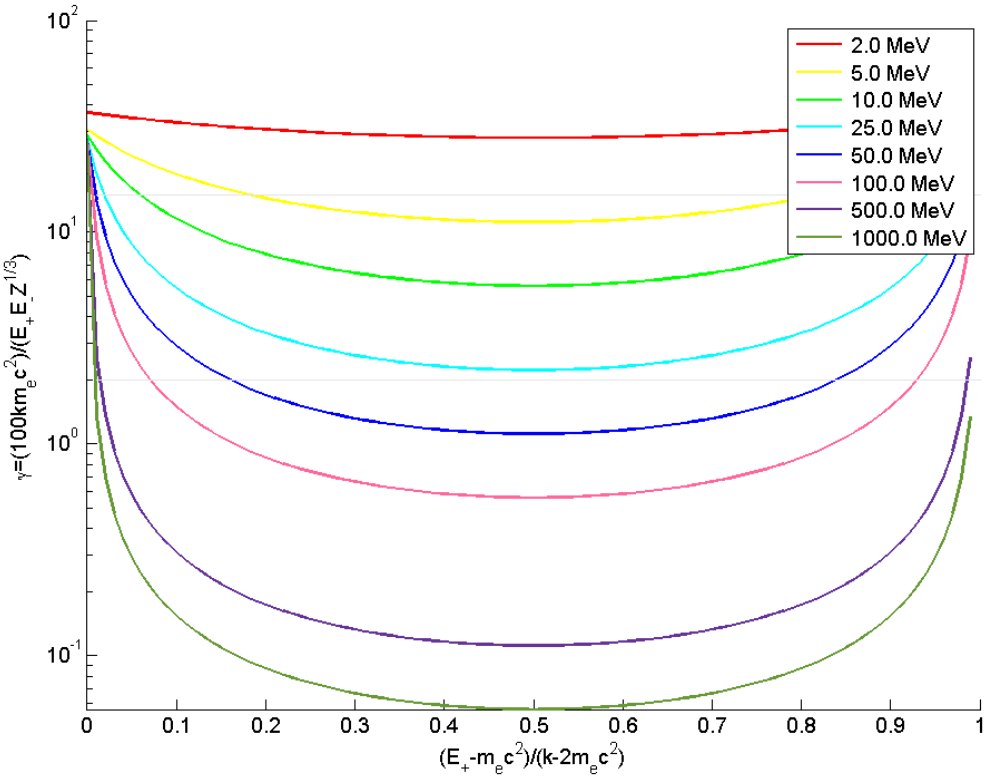

Figure 2.8: The effect of screening is described by the function γ [6, 5]. Function γ as a function of fractional energy of the positron in CdZnTe for various initial photon energies.

the electron and the positron were studied.

The differential pair production cross section can be calculated from the equations given by Bethe and Heitler in reference [6]. The cross section is a complicated function that can be simplified if all energies are large compare with the rest mass of the electron $m_e c^2$. The screening of the atomic potential by the outer electrons also affects the cross section. For example, at high energies, the radius from the nucleus at which the interaction occurs increases and eventually exceeds the distance from the K-electron shell to the nucleus. In this case, the effective nuclear charge is reduced because of screening by the charge of the atomic electrons. The function γ determines the effect of screening [6, 5]. Figure 2.8 shows the function γ as a function of fractional

energy of the positron in CdZnTe for various initial photon energies. If γ is equal to 0, the screening is defined as complete. In this case, the differential pair production cross section is determined entirely by the atomic radius. If γ is between 0 and 15, the screening is defined as partial and finally, if γ is above 15, there is no screening effect.

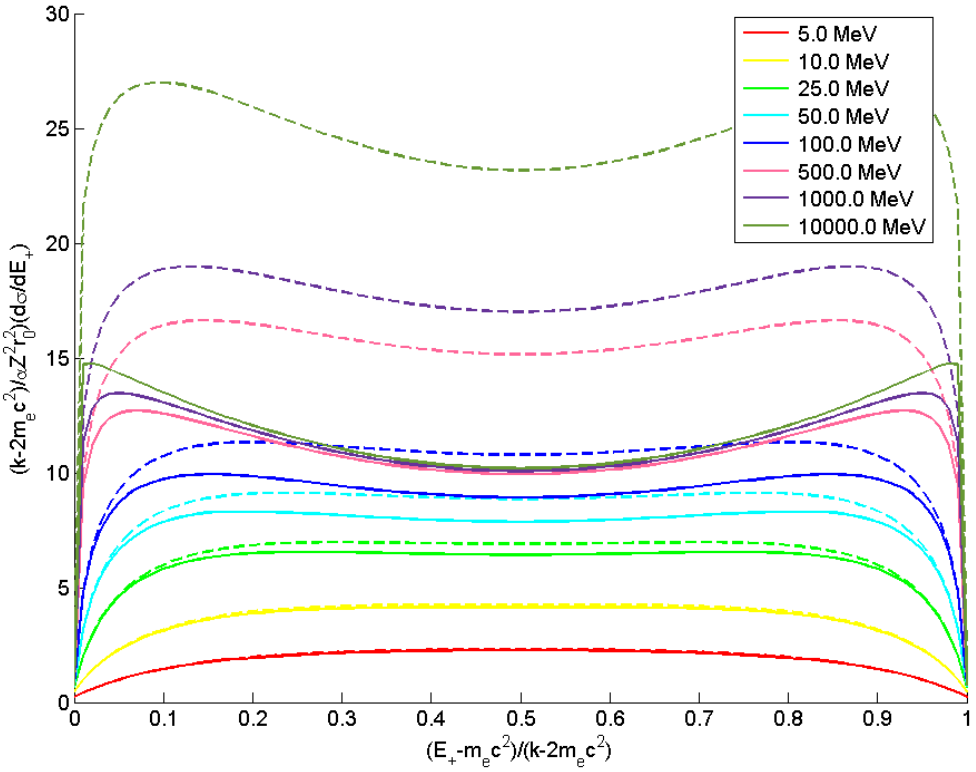

Figure 2.9: Differential pair production cross section with screening corrections (solid lines) and without (dashed lines) as a function of fractional energy of the positron in CdZnTe for various initial photon energies.

Figure 2.9 shows the differential pair production cross section as a function of fractional energy of the positron in CdZnTe for various initial photon energies. This figure includes the cross section calculations with (solid lines) and without (dotted lines) screening corrections. The screening effect does not influence the symetry of the energy distribution between the electron and the positron but it reduces the differential pair production cross section. The equations used to calculate the differential

pair production cross sections can be found in Appendices A and B.

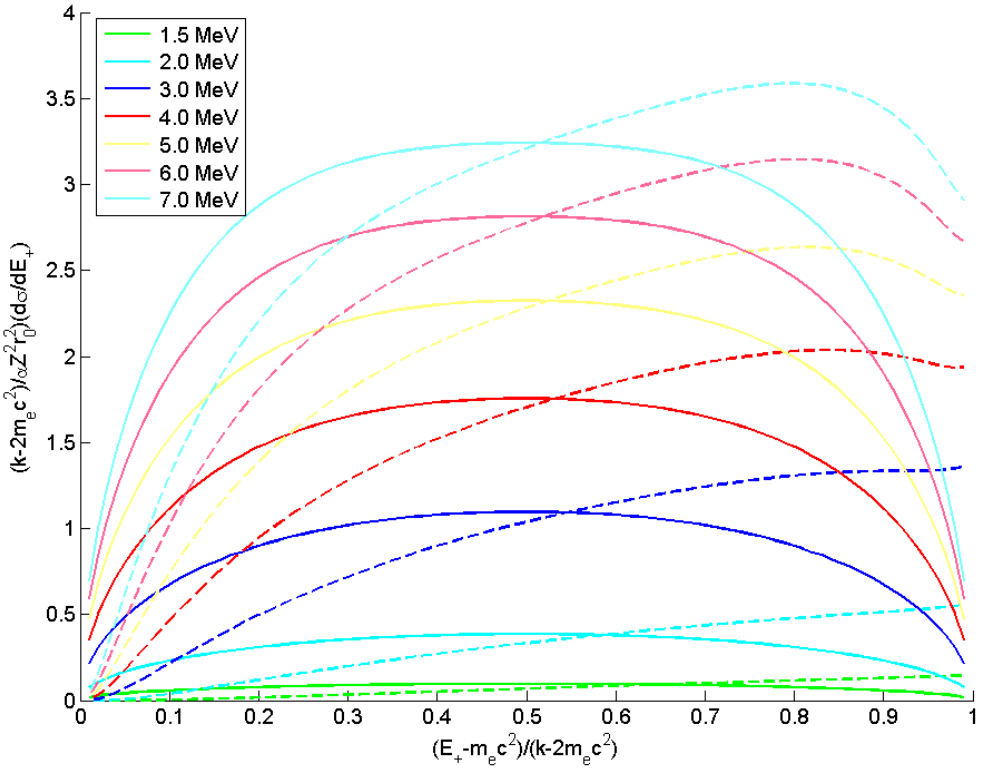

Figure 2.10: Differential pair production cross section with Born's first approximation (solid lines) and without (dashed lines) as a function of fractional energy of the positron in CdZnTe for various initial photon energies.

For the calculations of the differential pair production cross sections shown in Figure 2.9, the condition of the Born first approximation $Z/137\beta \ll 1$ where β=v/c with v the velocity of the particles and c the speed of the light, was assumed to hold for both the electron and the positron. Therefore, the theory is in error for small energies of the positron and the electron, which occurs for photon energies near threshold ($2m_e c^2$). Exact calculations [6] were used to calculate the differential pair production cross section as a function of fractional energy of the positron in CdZnTe and is shown in Figure 2.10. It can be seen from this figure that the distribution using the exact formulas is asymmetrical. Indeed, the positron is repelled by the nucleus

while the electron is attracted. Therefore, the probability of transferring more energy to the positron is higher at low energies. The asymmetry becomes less important as the energy of the photon increases because the radius from the nucleus at which the interaction occurs increases. The exact formulation used to calculate the differential pair production cross section at low energy can be found in Appendix C.

2.2.4.1 Pair Production Imaging

It is possible to measure the incident direction of each photon through the pair production process by tracking and measuring the momentum, direction and the energy losses of both the electron and positron. Here we describe two examples of pair telescopes for the high- and medium-energy gamma-ray range.

The Large Area Telescope (LAT) [20] on the Fermi Gamma-ray Space Telescope is an imaging, wide field-of-view, high-energy gamma-ray telescope, covering the energy range from about 20 MeV to more than 300 GeV. The LAT is a pair-conversion telescope with a precision converter-tracker and calorimeter, each consisting of a 4×4 array of 16 modules, a segmented anticoincidence detector that covers the tracker array, and a programmable trigger and data acquisition system. The converter-tracker has 16 planes of high-Z material in which gamma rays incident on the LAT can convert to an electron positron pair. The converter planes are interleaved with position-sensitive detectors that record the passage of charged particles, thus measuring the tracks of the particles resulting from pair conversion. This information is used to reconstruct the directions of the incident gamma rays. Each tracker module has 18 (x, y) tracking planes, consisting of 2 layers (x and y) of single-sided silicon strip detectors. The 16 planes at the top of the tracker are interleaved with high-Z converter material, tungsten. Incident photons preferentially convert in one of the tungsten foils, and the resulting electron and positron particles are tracked by the silicon strip detectors through successive planes.

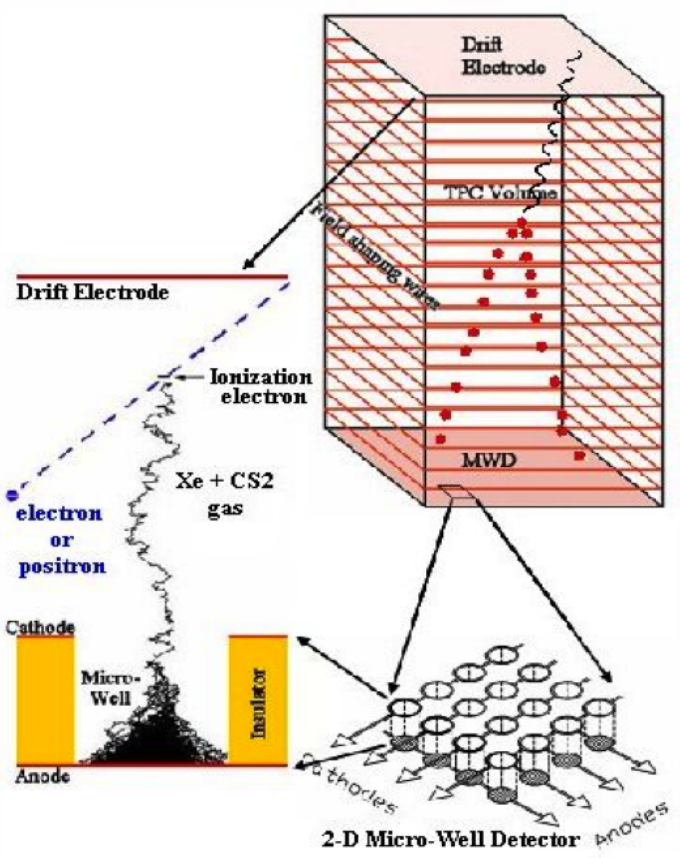

Figure 2.11: Schematic of the 3-DTI showing the TPC volume and MWD. The electron positron pair from a gamma-ray pair conversion in the TPC traverses the gas leaving a trail of ionization charge that drifts toward the MWD array and into individual wells [25].

The primary purposes of the calorimeter is to measure the energy deposition due to the electromagnetic particle shower that results from the electron positron pair produced by the incident photon. Each calorimeter module has 96 CsI(Tl) crystals, with each crystal of size 2.7 cm $\times$ 2.0 cm $\times$ 32.6 cm. The crystals are optically isolated from each other and are arranged horizontally in 8 layers of 12 crystals each. Each calorimeter module layer is aligned 90° with respect to its neighbors, forming an x, y hodoscopic array.

The Advanced Energetic Pair Telescope (AdEPT) [25] developed at NASA GSFC in the Astroparticle Physics Laboratory, image gamma rays in the relatively unexplored medium-energy range, from about 5 to 200 MeV, via the electron positron pair

process. The enabling technology for AdEPT is the Three-Dimensional Track Imager (3-DTI), which combines a time projection chamber (TPC) and a 2-D micro-well detector (MWD). The MWD is a gas proportional counter to readout the signal in 2 dimensions. Charged particles, including the electron positron pair from pair production, traversing the TPC volume leave a trail of ionization charge that drifts into the wells of the MWD, which provides the x- and y-coordinates of the charge. The z-coordinate is determined from the relative time of arrival of the signals. Figure 2.11 is a schematic of the 3-DTI showing the TPC and the MWD.

The quasi-monoenergetic 6 MeV Gamma facility provides the possibility to study pair production imaging with pixelated CdZnTe detector at 6 MeV. From Figure 2.10 we can see that at 6 MeV the cross section is higher when the fractional energy of the positron is about 0.9, which corresponds to an energy of about 5 MeV. In this case, the electron has an energy of 1 MeV. Figure 2.12 shows the range of electrons in CdZnTe material as a function of energy. It shows that an electron of 5 and 1 MeV has a range of 6.1 and 1.2 mm in CdZnTe material, respectively. Our detector's pixel pitch is 1.72 mm. Therfore, in the most probable case, the positron track corresponds to about 3.5 pixel pitch lengths while the electron track is less than the pixel pitch. It would therefore not be possible in this case to reconstruct an image. For comparison, the electron range in Ar is also shown. The range is about 4 orders of magnitude higher at 4 MeV. Therefore, in the low energy range, close to the threshold of the pair production process, a gas, such as Ar which is used in AdEPT, is required for pair production imaging. At higher energies, it becomes possible to image the tracks of the pair in CdZnTe; however, the probability that the initial gamma ray escapes the detector increases. Our current detectors are relatively small, 6 cm^3 per unit and therefore pair productin imaging at higher energies becomes possible only if an array of detectors is used.

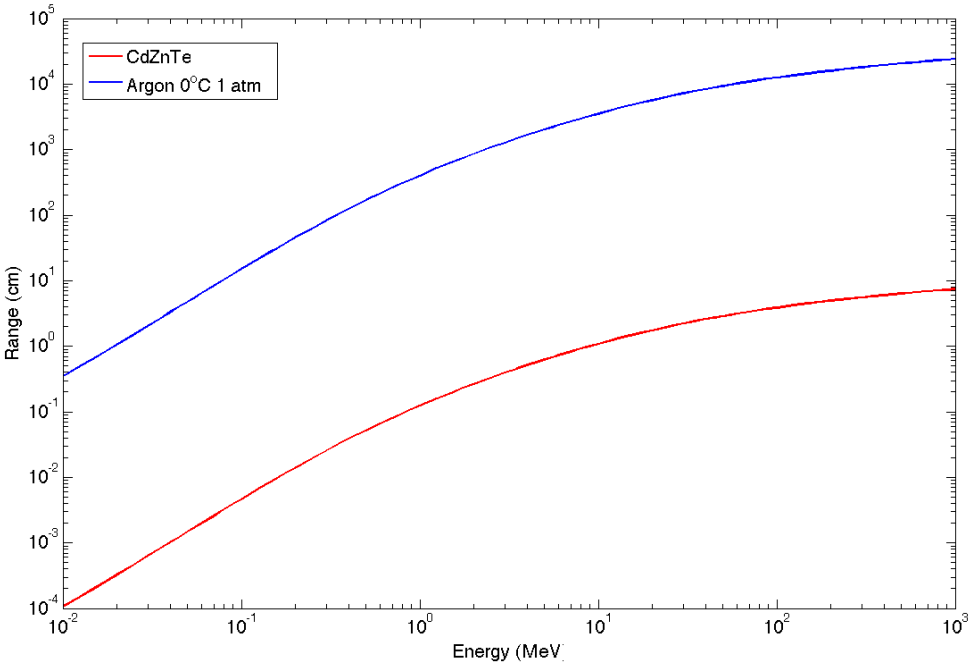

Figure 2.12: Electron range in CdZnTe material and Ar.

CHAPTER III

The Quasi-Monoenergetic 6 MeV Gamma Facility

The 6 MeV Gamma Facility has been developed at NASA GSFC to allow in-house characterization and testing of a wide range of gamma-ray instruments such as pixelated CdZnTe detectors for planetary science and Compton and pair-production imaging telescopes for astrophysics [32]. The 6 MeV Gamma Facility utilizes a circulating flow of water irradiated by 14 MeV neutrons to produce gamma rays via the ^{16}O(n,p)^{16}N $\rightarrow$ ^{16}O* $\rightarrow$ ^{16}O + γ reaction. The facility provides low cost, in-house source of 2.742, 6.129 and 7.117 MeV gamma rays, near the lower energy range of most accelerators and well above the 2.614 MeV line from the ^{228}Th decay chain, the highest energy gamma ray available from a natural radionuclide. The 7.13 s half-life of the ^{16}N decay allows the water to be irradiated on one side of a large granite block and pumped to the opposite side to decay. Separating the irradiation and decay regions allows for shielding material, the granite block, to be placed between them, thus reducing the low-energy gamma-ray continuum.

The comparison between high purity germanium (HPGe) spectra from the facility and a manufactured source, ^{238}Pu/^{13}C, shows that the low energy continuum from the facility is reduced by a factor 30 and the gamma-ray rate is 100 times higher at 6.129 MeV. Systems such as the one developed by Kroupa *et al.* [28] also provide monoenergetic gamma-ray lines above 3 MeV but such systems do not provide shielding

against low-energy gamma rays, such as the 2.2 MeV line from neutron capture on hydrogen. By shielding these other lines, significant reduction in Compton continuum can be observed compared to manufactured sources such as $^{238}Pu/^{13}C$.

3.1 Design

The quasi-monoenergetic 6 MeV Gamma Facility has been developed at an existing oudoor facility, the Goddard Geophysical and Astronomical Observatory (GGAO) where a large block of granite is being used as shielding material in order to reduce the low-energy gamma-ray background. It was possible to leverage the cost of the project by using the existing equipment that the GGAO outdoor test site offers. The first paragraph of this section gives a brief overview of the GGAO site.

3.1.1 Goddard Geophysical and Astronomical Observatory

PING tests are conducted at a unique test facility at GGAO [9] site on a known sample material in the same geometry as that of future solar system in situ applications. The site provides two large (1.8 m $\times$ 1.8 m $\times$ 0.9 m), well characterized basalt and granite formations installed outdoors in the middle of a very large open area as shown in Figure 3.1. Instrumentation tests are conducted by placing the PNG and gamma-ray and neutron detectors on top of one of the large rock formations to measure the characteristic gamma rays and epithermal and thermal neutrons that come from the rock sample as the result of the neutron interactions. The meter-scale size of our samples ensures that the 14 MeV neutrons emitted by the PNG interact primarily in this sample, with very few interactions occurring in other materials in its environment. Due to the radiation safety hazard, all tests are conducted remotely from inside a building located about 60 m away (shown in the top of Figure 3.1). The GSFC Radiation Safety Office mandates that no personnel be located within a 45 m radius safety perimeter during PNG operation. The facility includes buried electri-

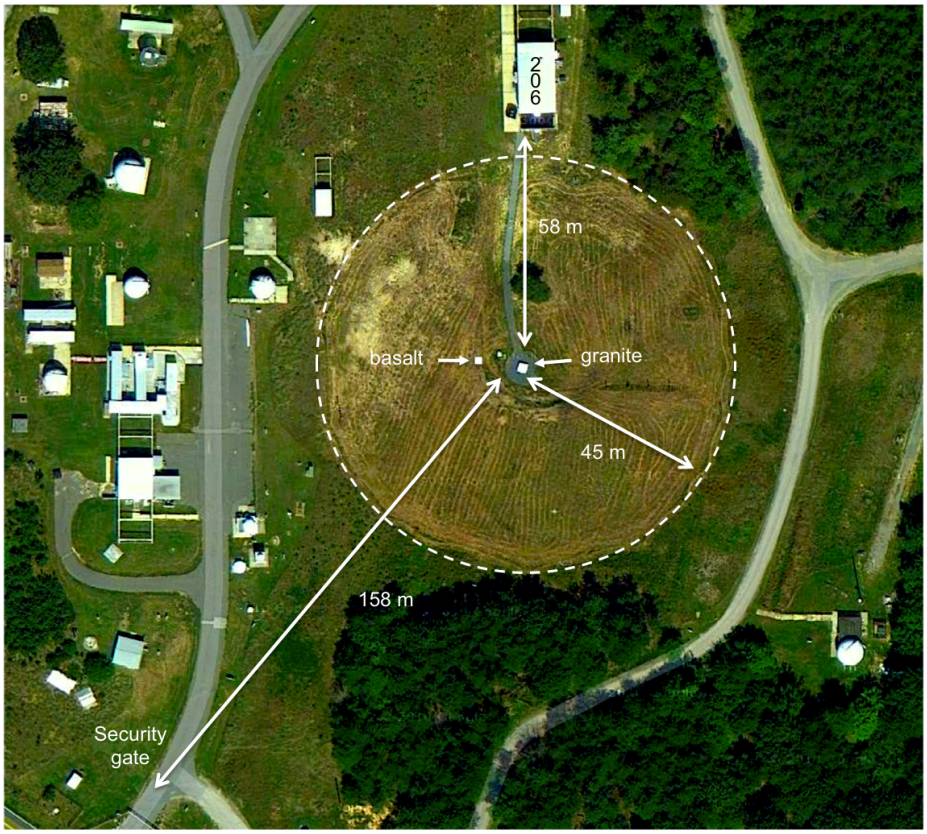

Figure 3.1: Aerial view of the GSFC/GGAO test site showing the 45 m radius safety perimeter (white dashed circle) defined by the GSFC Radiation Safety Office. The remote operation's building (Building 206) is shown at the top of the image. The granite block supporting the 6 MeV Gamma Facility is located at the center of the large field and the basalt block is nearby to the left.

cal power and ethernet communications cables connecting the computers inside the building to power outlets and LAN ports next to the formations. A gravel path has been installed between the operations building and the two gravel pads surrounding the formations, making it easier to transport equipment to these rock samples.

3.1.2 Concept

Gamma rays are generated via the ^{16}O(n,p)^{16}N reaction using the 14 MeV neutrons from the PNG to activate oxygen in a volume of water continuously circulated around the granite block. The cross-section for the ^{16}O(n,p)^{16}N reaction is 4.2×10^{-2}

barns at 14 MeV [11]. The ^{16}N decays via beta decay with a 7.13 s half-life [11] to ^{16}O* that rapidly de-excites producing gamma rays with energies of 2.742, 6.129, and 7.117 MeV. As seen in Figure 3.2, the respective probabilities associated with these gamma-ray energies are 0.82%, 67%, and 4.9% and no gamma ray produced 28% of the time [11]. These gamma rays are also available from manufactured sources, such as ^{238}Pu + ^{13}C ($\alpha + {}^{13}\mathrm{C} \rightarrow {}^{17}\mathrm{O} \rightarrow {}^{13}\mathrm{O}^{*} \rightarrow {}^{13}\mathrm{O} + \gamma$), however, the low-energy gamma ray and neutron emission from these source decreases the relative intensity of 6 MeV gamma rays. A ^{238}Pu/^{13}C source with 6.129 MeV gamma-ray rate comparable to the NASA/GSFC Gamma Facility would have a total activity of ∼43 Ci, far too strong a source for safe laboratory use.

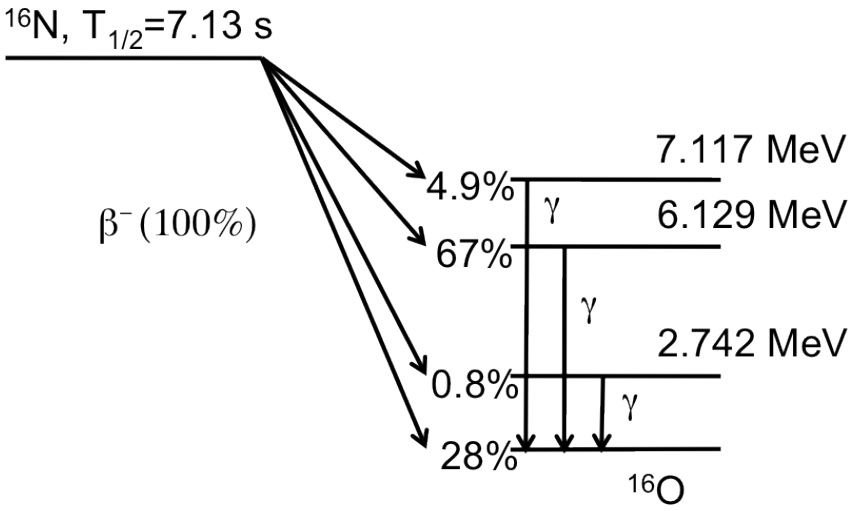

Figure 3.2: ^{16}N beta decay level scheme. Photons of 2.742, 6.129, and 7.117 MeV are produced from the de-excitation of the excited states of ^{16}O with probability of 0.82%, 67%, and 4.9%, respectively and no gamma ray produced 28% of the time [11].

The 7.13 s half life of the ^{16}N decay to ^{16}O* allows the water to be irradiated on one side of the granite block and then piped to the gamma emission loop on the opposite side of the block shown schematically in Figure 3.3 (a). The 1.8 m thick granite block provides shielding from most of the neutrons and protons generated by the PNG and the ^{16}O(n,p)^{16}N reaction as well as gamma rays produced by other prompt

neutron reactions in the granite and soil elements. The 6 MeV Gamma Facility, as shown in Figure 3.3 (b), consists of a closed loop of polyvinyl chloride (PVC) pipe supported by a steel framework resting on the granite block. The closed loop has two major components: the 'neutron activation loop' and the 'gamma emission loop'. The input and output of the activation and decay loops are connected by the 'supply pipe' and the 'return pipe'. The return pipe contains the in-line circulation pump, TACO Model 2400-50, and flow rate meter, Omega Model FTB-1307. PVC pipe was chosen to construct the facility because of its low cost and simple solvent assembly. The geometries of the two loops are described below and the simulated production of ^{16}N in the neutron activation loop and the calculated 6.129 MeV gamma-ray rate from the emission loop are presented in section 3.2.

3.1.3 The Neutron Activation Loop

The neutron activation loop, as seen in Figure 3.4, consists of 15 m of 4.1 cm (1.5 inch nominal) inner diameter (ID) flexible PVC pipe. This flexible pipe is wrapped around the PNG support structure in two layers with 7 inner layer and 6 outer layer coils. The PNG is positioned so that the neutron emission plane of symmetry is centered in the activation coil to maximize the production of ^{16}N across the coil. The PNG is operated in a continuous mode to provide a neutron flux of 10^7 n/s. The volume of the activation loop is $\sim 1.98 \times 10^4$ cm^3. At a flow rate of 2L/s the water dwells in the region of intense neutron flux of the PNG for $\sim$9.9 s. The activated water flows out of the activation loop, labeled 'B' in Figure 3.3, through the $\sim$250 cm long, 4.1 cm (1.5 inch nominal) ID rigid PVC supply pipe to the input of the gamma emission loop, labeled 'C'.

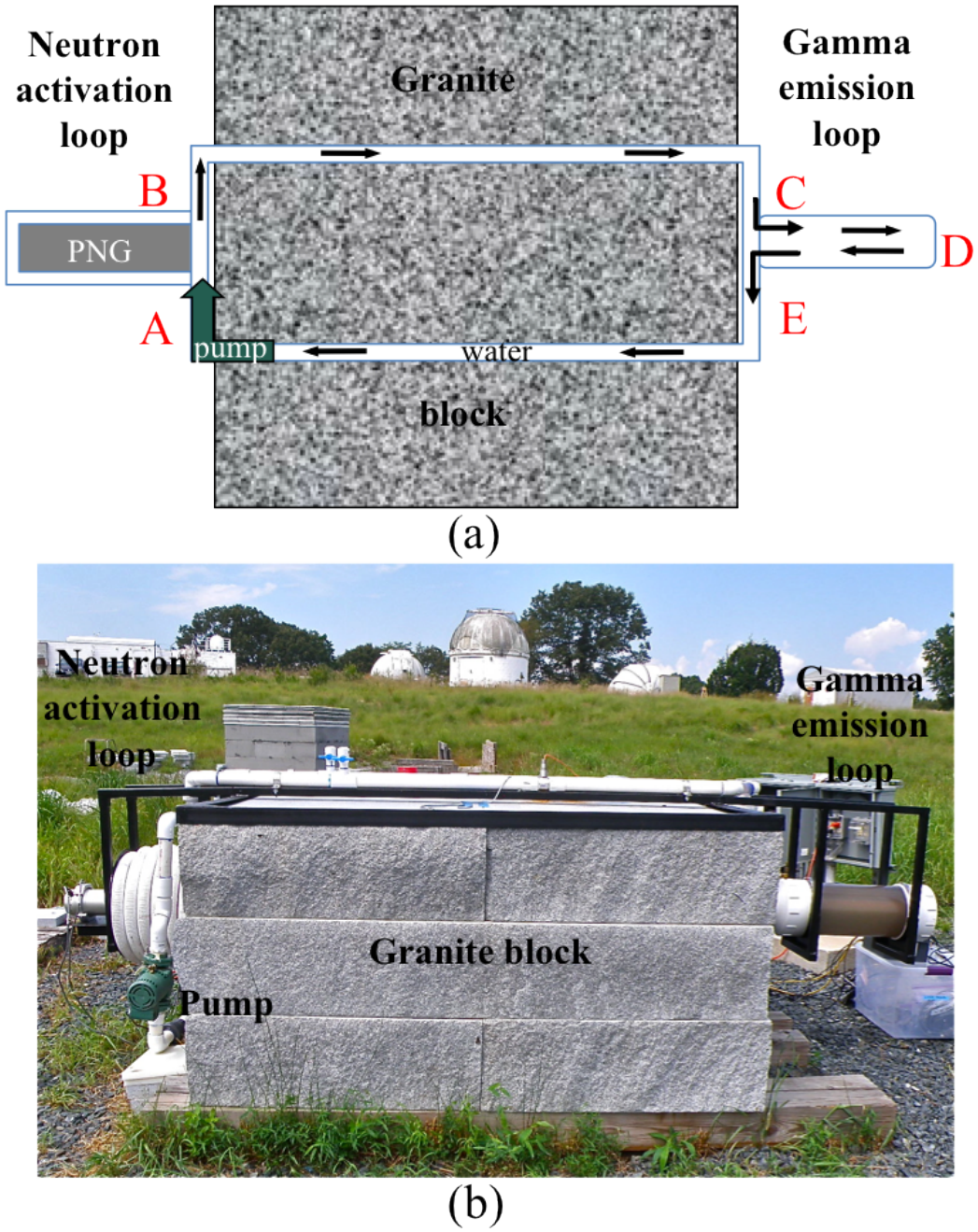

Figure 3.3: Schematic, top view (a) and side view picture (b) of the 6 MeV Gamma Facility. The closed loop of PVC pipe is suspended from a steel frame resting on top of the granite block. The major components of the facility include the neutron activation loop and the gamma emission loop. The inlet and outlet of the activation loop are denoted by 'A' and 'B' respectively. Similarly, 'C' and 'E' refer to the inlet and outlet of the decay loop. The point 'D' is the front end of the inner coaxial pipe of the decay loop.

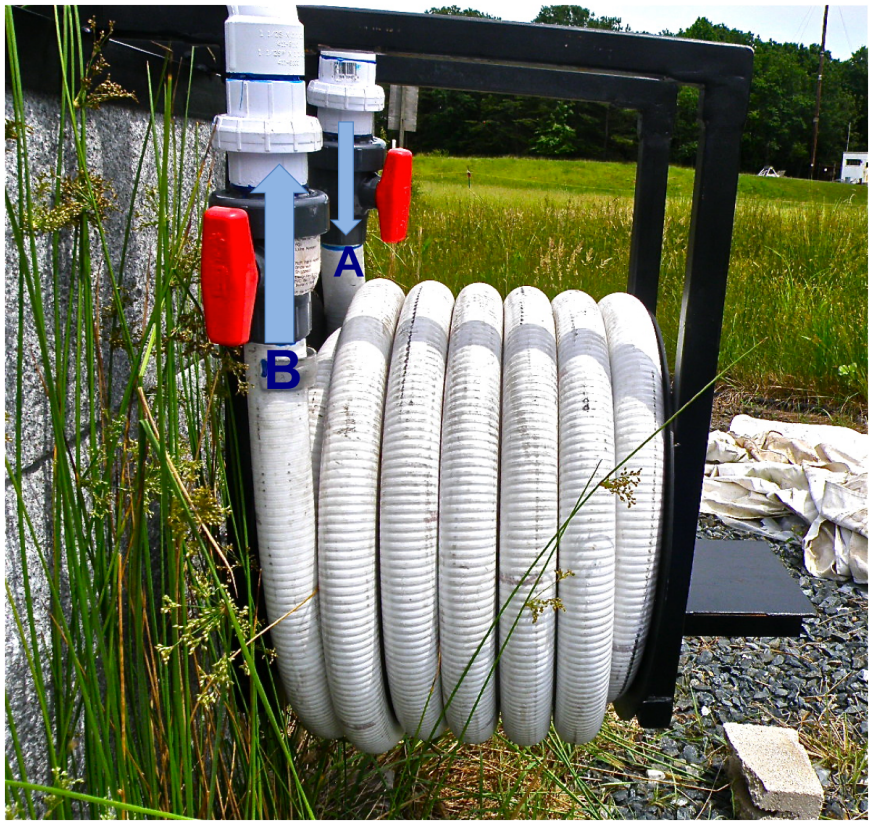

Figure 3.4: The neutron activation loop consists of 13 coils of flexible PVC pipe wrapped around a steel structure. The steel structure includes a horizontal shelf to position the PNG tube in the center of the activation loop. The red handled valves on the inlet, 'A', and outlet, 'B', of the activation loop are the connections to the supply and return pipes, respectively. The arrows indicate the direction of the water flow.

3.1.4 The Gamma Emission Loop

The gamma emission loop, as seen in Figure 3.5, has a coaxial design. The irradiated water flows through the inner, 4.1 cm (1.5 inch nominal) ID, 4.8 cm outer diameter (OD), rigid PVC tube, labeled 'C' in Figure 3.3, which ends ∼2 cm before the inner face of the curved front end cap, labeled 'D'. In this way, the water with the highest level of activation comes out at the front surface of the cylinder, 'D', minimizing the self-attenuation of the water (2.77×10^{-2} cm^{-1} at 6 MeV [30]) and maximizing the gamma-ray flux. The water then flows back through the outer, 20.2 cm (8 inch nominal) ID, clear PVC tube ∼65 cm long, towards the back end cap and

out the return pipe, labeled 'E'. The increase in pipe cross-sectional area results in a factor of ∼22.9 slower flow velocity in the outer tube. At a flow rate of $2{\times}10^3$ cm^3/s, the water dwells in the inner and outer tubes for ∼0.41 s and ∼9.8 s respectively. The PVC wye (3 inch nominal ID) at the back of the decay loop provides the coaxial input, 'C', to the gamma decay loop and output, 'D', to the ∼250 cm long, 4.1 cm (1.5 inch nominal) ID rigid PVC return pipe to the input of the irradiation loop, 'A'.

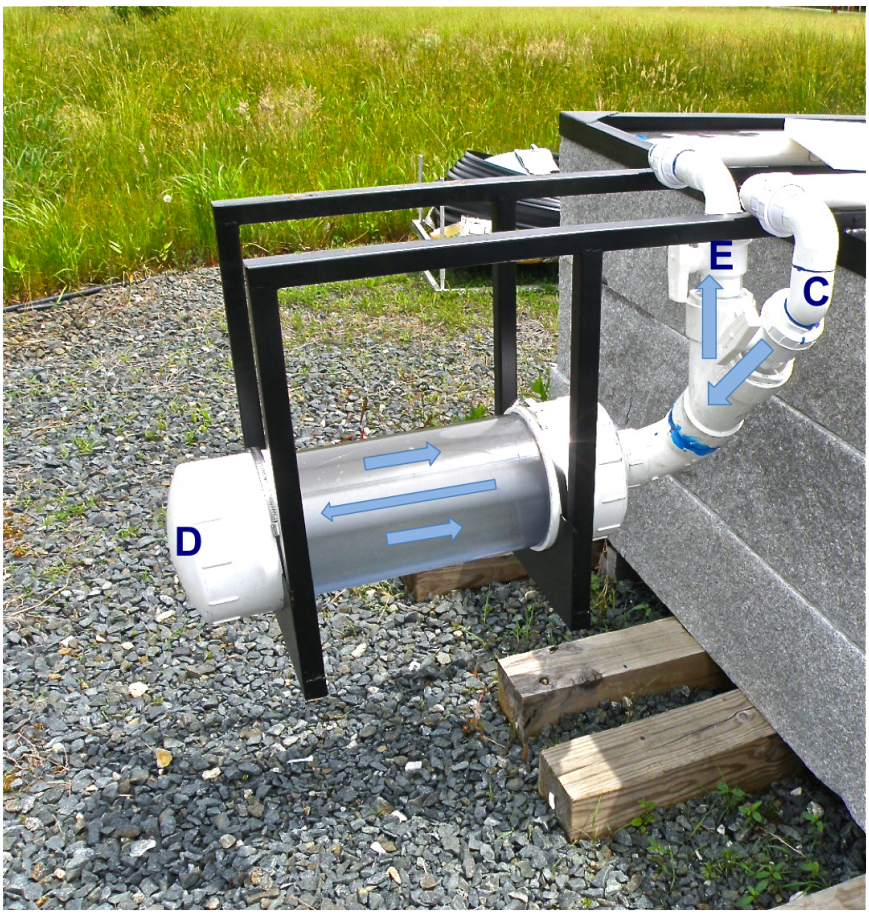

Figure 3.5: The gamma emission loop consists of two coaxial PVC pipes. The activated water enters through the straight leg of the wye fitting, 'C', and flows through the inner pipe to within 2 cm of the front cap on the left of the emission loop, 'D'. The water flows back through the large diameter tube towards the end cap and out through the angled leg of the wye, 'E', and returns to the irradiation loop. The white handled valves on the straight and angled legs of the wye are the inlet and outlet of the emission loop and the connections to the supply and return pipes, respectively. The arrows indicate the direction of the flow.

3.2 Simulation Results

The water is continuously circulated between the irradiation and decay loops to achieve steady-state gamma-ray emission. The activity of the gamma-ray emission loop was simulated as a function of the flow rate to estimate the optimum flow-rate and to determine the required capacity of the circulating pump and flow meter. This was done using a two-step simulation process.

3.2.1 ^{16}N Production Rate

The production rate of ^{16}N in the neutron activation loop for the ^{16}O(n,p)^{16}N reaction was simulated using Monte Carlo N-Particle eXtended (MCNPX) [35]. The coils of the activation loop surrounding the PNG tube were modeled as a series of water filled PVC tori. The steel structure, granite block and soil were not included in the simulation because only the isotopes of ^{16}N from the neutron activation loop are transported to the gamma emission loop. The simulation model and the probability of ^{16}N produced per neutron per cm^3 for each torus estimated by MCNPX can be seen in Figure 3.6. The volume weighted average production probability of ^{16}N across the entire activation loop is 2.4×10^{-7} ^{16}N/n/cm^3.

The estimated relative error for each measurement point given by MCNPX is defined as one standard deviation of the mean divided by the estimated mean [41]. The average relative error is 0.035%, which is too small to be seen on the plot on Figure 6.12.

3.2.2 6.129 MeV Gamma-Ray Production Rate

The activity of the source was estimated as a function of time by solving the following differential equations:

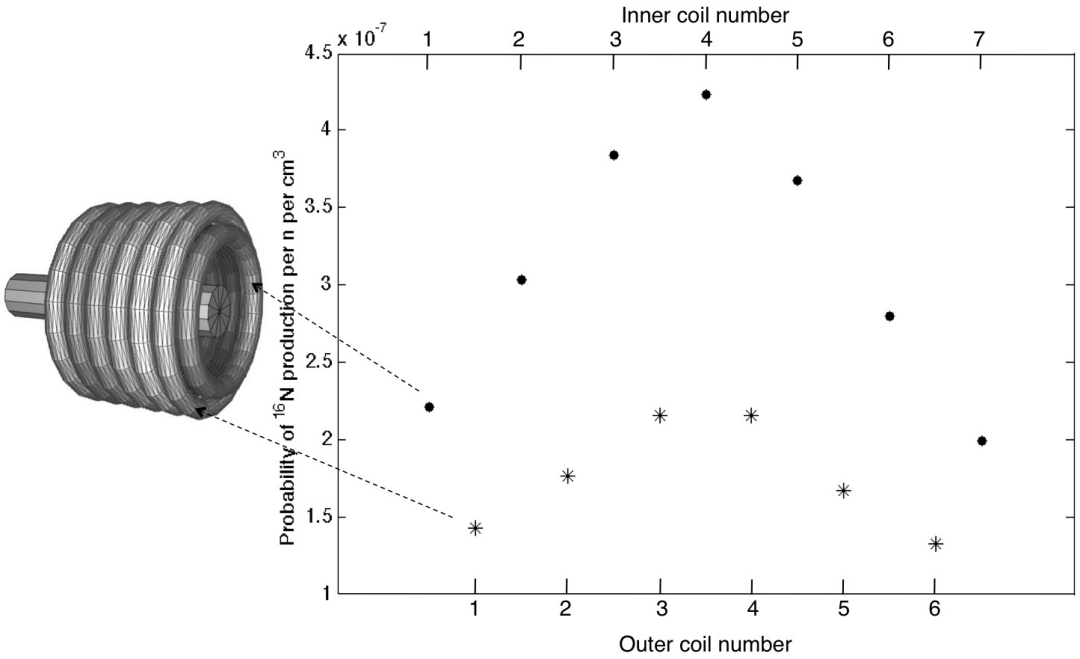

Figure 3.6: The ^{16}N production in the neutron activation loop was modeled as a nested set of 13 tori, 7 in the inner layer and 6 in the outer layer. The MCNPX simulated probability of ^{16}N produced per neutron per cm^3 for each coil of the irradiation loop is plotted. The simulation errors are smaller that the symbols. The volume weighted average value of all 13 tori is 2.4×10^{-7} ^{16}N/n/cm^3.

$$\frac{d^{16}N}{dt} = \sigma\phi^{16}O - \lambda^{16}N \tag{3.1}$$

$$\frac{d^{16}N}{dt} = -\lambda^{16}N \tag{3.2}$$

where σ is the cross section at 14 MeV, ϕ is the neutron flux and λ is the half life. Equation 3.1 applies to the water circulating on the side of the neutron activation loop and equation 3.2 applies to the water in the rest of the loop. The simulated 6.129 MeV gamma-ray flux as a function of the flow rate is shown at different location in

the loop in Figure 3.7.

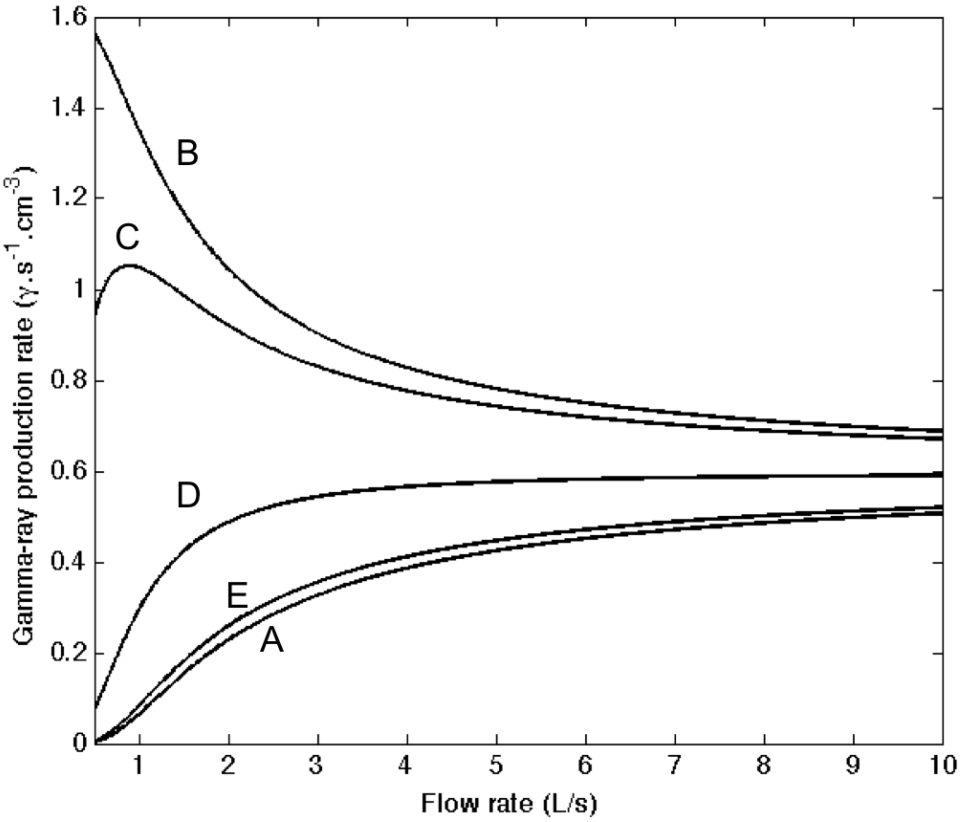

Figure 3.7: The 6.129 MeV gamma-ray production rate calculated as a function of the water flow rate at the beginning, 'A', and end, 'B', of the irradiation loop and at the beginning, 'C', middle, 'D', and end, 'E' of the emission loop.

Finally, the steady state activity of the gamma emission loop as a function of the water flow rate was estimated by integrating these results over the volume of the gamma emission loop. Figure 3.8 shows the activity of the gamma emission loop as a function of the flow rate on the assumption of a PNG output of 10^7 n/s at 14 MeV. The highest flow rate achievable with the Taco 2400-50 circulation pump, $\sim$2 L/s, was limited by the head pressure in the plumbing. The stability of the flow rate is very good; the observed variation is less than $\pm$0.01 L/s at 2 L/s. At this flow rate the 6.129 MeV gamma-ray rate of the gamma emission loop reaches about 85%

of its maximum value. A higher flow rate of ∼4 L/s is desirable to maximize the gamma-ray flux and to reduce any flux variation on flow rate. This flow rate can be achieved by using a more powerful pump that will be purchased and installed when funding is available.

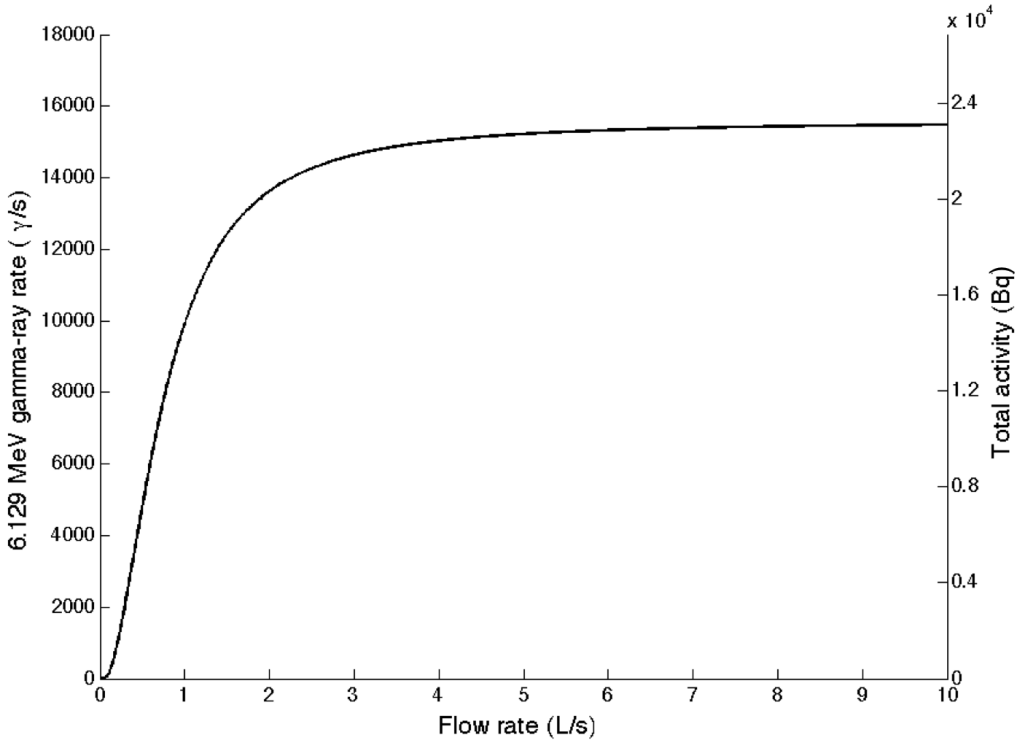

Figure 3.8: Isotropic 6.129 MeV gamma-ray rate and total isotropic activity of the gamma emission loop as a function of the water flow rate calculated on the assumption of a PNG output of 10^7 n/s.

3.3 Experimental Results

3.3.1 Quasi-Monoenergetic 6 MeV Gamma Results

Gamma-ray spectra were acquired with an Ortec HPGe detector, Model GMX30, on the neutron activation loop and gamma emission loop sides of the granite block. The front face of the HPGe detector was placed 10 cm from the forward end of the gamma emission loop and coaxially aligned. A natural radioactive background

spectrum was obtained with the PNG turned-off after waiting for about ten ^{16}N-beta-decay half-lives (∼70 s) until the short half-life isotopes had decayed. Figure 3.9 compares the gamma-ray spectra from the background-subtracted activation loop, emission loop, and ^{238}Pu/^{13}C source. The activation and ^{238}Pu/^{13}C source spectra were normalized to the 6.129 MeV peak intensity of the emission spectrum in order to compare the low energy continuum. The reduction in both the gamma-ray continuum and the number of peaks for the gamma emission loop spectrum below ∼5 MeV and above ∼6 MeV indicates the shielding effect of the granite block to the gamma rays produced in the granite and soil. The 6.129 MeV and 7.113 MeV photopeaks can be seen along with their single and double escape peaks. The 2.742 MeV photopeak and escape peaks are also visible in the spectra, however, these peaks overlap with the 2.2 MeV and 1.7 MeV neutron capture on H and Si peaks present in the granite, respectively. The 511 keV line is also visible.

3.3.2 Source Activity Results

The activity of the gamma emission loop, determined by the integral area under the 6.129 MeV photopeak, was estimated from the experimental data in Figure 3.9 using Igor Pro software [40]. The conversion from the HPGe activity to the total activity of the gamma emission loop was determined using MCNP-PoliMi [33] to simulate the gamma ray interaction probability in the HPGe detector assuming the number of gamma rays produced by the gamma emission loop is known. The ratio of gamma rays recorded by the HPGe to gamma rays emitted by the gamma emission loop was used with the experimental results to estimate the total activity of the gamma emission loop. The simulation took into account the geometry between the emission loop and the HPGe detector, the HPGe efficiency at 6.129 MeV, the gamma-ray attenuation of the water, and the ^{16}N decay time. The coaxial design of the gamma emission loop was simulated as two cylindrical volumes emitting isotropic

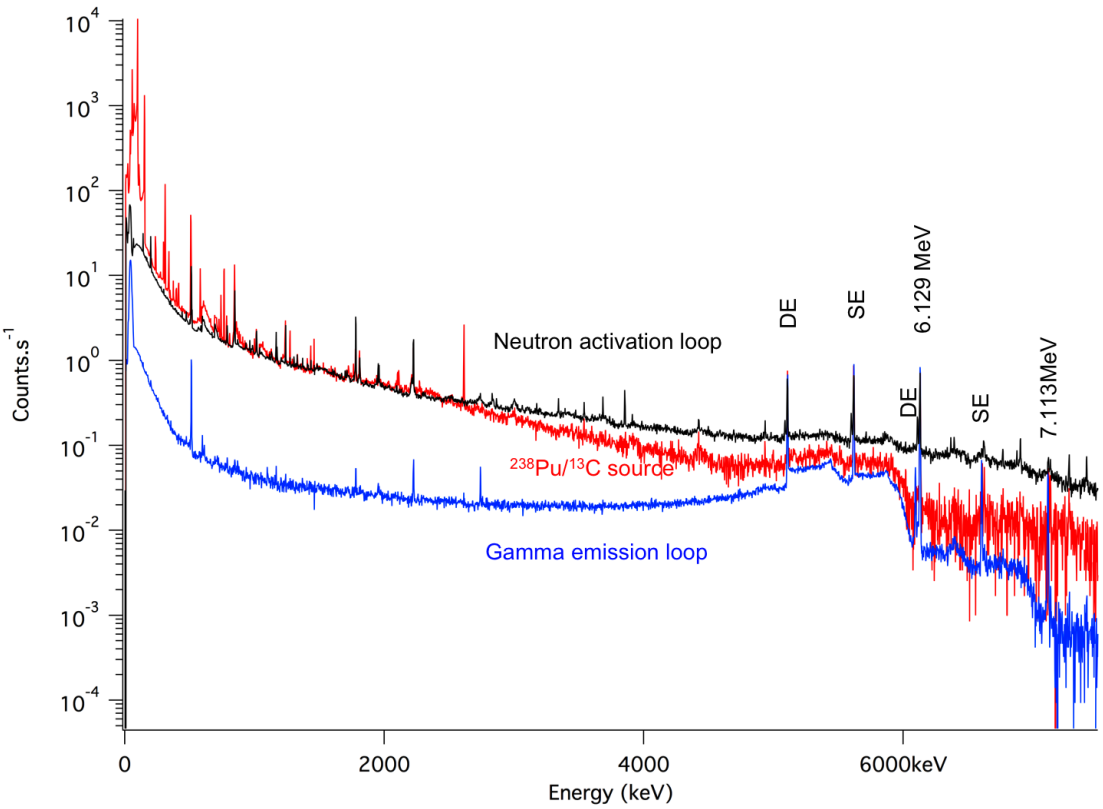

Figure 3.9: HPGe background subtracted gamma-ray spectra from the neutron activation loop (black), the gamma emission loop (blue) and the ^{238}Pu/^{13}C source (red). The spectra of the activation loop and ^{238}Pu/^{13}C source have been normalized to match the 6.129 MeV gamma-ray intensity of the gamma emission loop spectrum.

radiation. The decay time of the ^{16}N in the water was simulated by setting the source probabilities (SP card in MCNP-PoliMi) as an exponential function on the axial limits of the cylinders. The simulation required the two volumes to be treated separately because of the different flow directions. The results, in units of gamma rays detected in the HPGe per gamma ray emitted, were combined to get the total detection rate, taking into account the difference in flow velocities and volumes of the two cylinders. The simulation results show that the ratio of gamma rays recorded in the HPGe to gamma rays emitted by the gamma emission loop was 5.4×10^{-4}. The area under the 6.129 MeV photopeak shown in Figure 3.9 is 2.02 ± 0.01 gamma

rays/s. The total estimated gamma-ray rate at 6.129 MeV is $(3.74 \pm 0.03)\times10^3$ gammas/s and the total activity of the gamma emission loop is $(5.42 \pm 0.04)\times10^3$ Bq.

The difference between the simulated 6.129 MeV gamma-ray rate of 13×10^3 gamma/s and the experimentally measured rate is attributed to:

1) Uncertainty in the PNG neutron flux: The PNG neutron yield of 10^7 n/s used for the simulation was based on the calibration settings provided by the PNG manufacturer. These settings were also used for operation; however a direct measurement of the PNG neutron flux was not available at the time of this experiment. We plan to purchase a fast neutron monitor, which will provide an accurate measurement of the flux. Based only on the observed gamma-ray flux, the PNG neutron flux was $\sim0.4\times10^7$ n/s.

2) Non-uniform radial velocity profiles in the system: The calculation of the 6.129 MeV gamma-ray production rate was made on the assumption of uniform bulk motion of the water, 1.85 ± 0.01 L/s, in the pipes and the neutron activation and gamma emission loops. Our assumption of uniform radial velocity profile in the gamma emission loop would lead to an overestimate of the true gamma-ray flux. A more detailed simulation of the gamma emission loop including the radial dependence of the flow velocity would provide a better estimate of the 6.129 MeV gamma-ray production rate.

CHAPTER IV

3-D Position Sensitive Detector Technology

A detector in which the position of the interaction in 3-D is known would allow one to use Compton imaging techniques to measure the direction of the incoming gamma rays by the method described in chapter II. On a planet, it would be possible to discard a fraction of the gamma rays coming from the lander or rover thus improving the sensitivity of our instrument to the planetary surface by reducing the background without the need for an anticoincidence shield.

This chapter describes the operating principle of pixelated detectors by presenting some of the relevant physics processes, such as the concept of induced charge, that are necessary for a good understanding of the pixelated detector operation. The design and the specific electronic readout system are presented as well.

4.1 Pixelated Semiconductor Detector Design

4.1.1 Induced Charge

The charge induced on the electrodes by the motion of charge carriers in a detector can be calculated using the Ramo theorem [36] that states that the current induced on a given electrode is:

$$i = q\vec{\nu} \cdot \vec{E} \tag{4.1}$$

where q is the charge of the carrier, $\vec{\nu}$ is its velocity and $\vec{E}$ is the weighting field. The theorem can be used to calculate the induced charge on an electrode, which is equal to the product of the charge carrier q times the difference of the weighting potential $\Delta\phi$ from the beginning to the end of the carrier path:

$$Q = q\Delta\phi \tag{4.2}$$

The weighting potential function ϕ can be found by solving the Laplace equation for the geometry of the detector using the following boundary equations: the voltage on the electrode studied is set to 1; it is set to 0 on all the other electrodes and no space charge is present (the trapped charges are ignored).

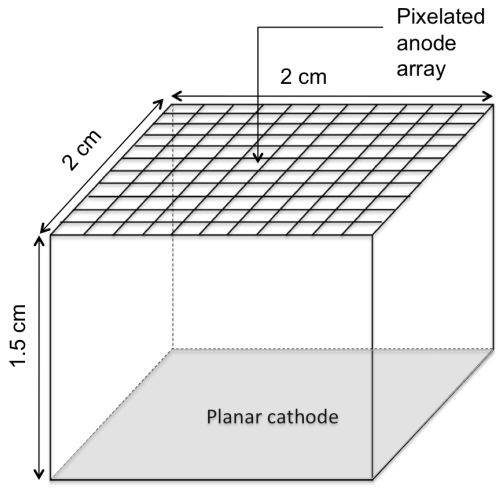

Figure 4.1: Detector with a pixelated anode array on the top surface and a planar cathode on the opposite side (bottom surface).

4.1.2 Detector Design

The detectors used in this study are large volume room-temperature semiconductor detectors that suffer severe hole trapping. For CdZnTe detectors, the hole mobility life-time product is about one order of magnitude lower than that of electrons [37]. To overcome the problem of hole trapping in thick semiconductor detectors, a 11 $\times$ 11 pixelated anode array and a planar cathode are deposited on opposite side of the crystal as shown in Figure 4.1. This geometry allows the collection of the electrons only and is referred to as single polarity charge sensing. The 3D interaction position of each gamma ray can be measured using pixelated detectors. The dimension of the crystal shown corresponds to the CdZnTe crystals that were used in this work. A grid is placed between the pixels to steer the charges to the pixels. A guard ring surrounds the pixelated array. The grid and guard ring are not shown in the figure.

He *et al.* [24] proposed a method of using the ratio of the cathode signal to the anode signal to obtain the interaction depth for pixelated detectors. Using Equation 4.2, it can be shown that, for a charge that moves from position x_i to x_f, the induced charge on electrode L can be written as:

$$\Delta Q_L = -q[\phi_{x_f} - \phi_{x_i}] \tag{4.3}$$

where ϕ corresponds to the weighting potential when electrode L is biased at unit potential (dimensionless), and all other electrodes grounded and all charges removed. The weighting potential as function of the detector thickness can be seen in Figure 4.2 for both the cathode and the collecting pixel. The weighting potential on the cathode (dotted line) is a linear function of the depth of interaction z. The charge induced on the cathode by the electrons travelling in the detector is linearly proportional to the depth of interaction in the detector. The weighting potential on the pixel (solid line)

remains close to zero until the depth of interaction z gets close to the anode where it suddenly increases to one.

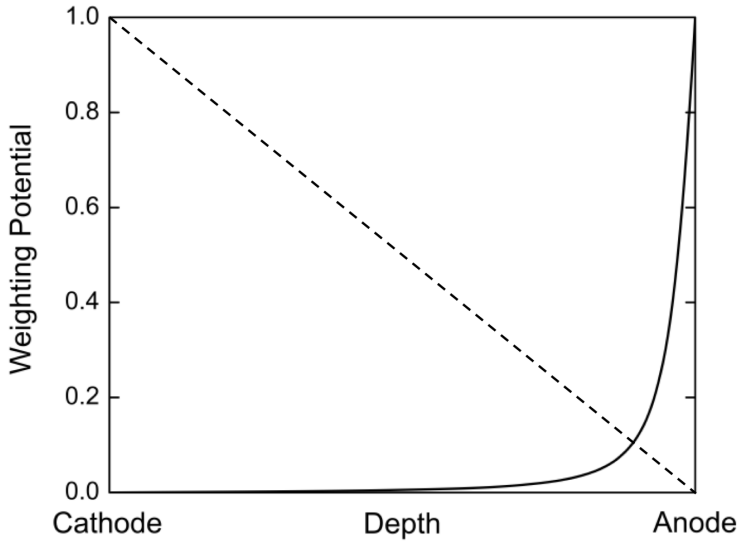

Figure 4.2: Weighting potential function for an anode pixel (solid line) and the planar cathode (dotted line).

Therefore, using Equation 4.3, for an interaction that occurred at depth z in the detector and not within about 1.72 mm of the pixel (which corresponds to the pixel pitch of the detector), it can be seen from Figure 4.2 that the induced charge on the pixel can be written as:

$$\Delta Q_{pixel} = -q[1 - 0] = -q \tag{4.4}$$

Similarly, the induced charge on the cathode is:

$$\Delta Q_{cathode} = -q[0 - z] = qz \tag{4.5}$$

From Equation 4.4, we can see that the charge induced on the pixel by the electrons travelling in the detector does not depend on the depth of interaction unless the

interaction occurs in the vicinity of the pixel. By reading out the induced charge on both the cathode and the pixels, one can measure the depth of interaction along the z-axis in the detector and the energy deposited. By using Equations 4.4 and 4.5, it can be shown that the ratio of the cathode to anode amplitude signals is:

$$\left|\frac{V_c}{V_a}\right| \propto \frac{ne_0 z}{ne_0} = z \tag{4.6}$$

where n is the number of electrons created by the gamma-ray interaction and z is the depth of interaction. The x and y positions are given by the pixel under which the gamma ray has interacted. It is then possible to use Compton imaging techniques with a single detector to measure the direction of the incoming gamma rays.

Figure 4.3: Picture of a 2 cm × 2 cm × 1.5 cm CdZnTe detector. The planar cathode can be seen on top of the detector. The detector's pixels are connected to pins through a substrate on which the crystal is supported. The crystal is coated in order to remain protected from the light.

A picture of one of the detectors used in this study is shown in Figure 4.3. The CdZnTe detectors were manufactured by Redlen Technologies, Inc. The CdZnTe detector possesses a planar cathode and an 11 × 11 pixelated anode array with a pixel pitch of 1.72 mm. The dimension of the crystal is 2 cm × 2 cm × 1.5 cm. The grid between the pixels is 100 μm wide and is 200 μm away from the pixels

around. All the electrodes are made of gold. The detector pixels are connected to pins through a substrate on which the crystal is supported. The crystal is coated in order to remain protected from the light.

4.2 Waveform Digitizer Readout System

A waveform digitizer readout system composed of a detector test box with electronic circuitry and digitizer cards was assembled to readout the pixels of the CdZnTe detector. By digitizing the waveform output of the preamplifiers, the shape is preserved and more deteailed analysis can be done.

4.2.1 Electronic Circuitry

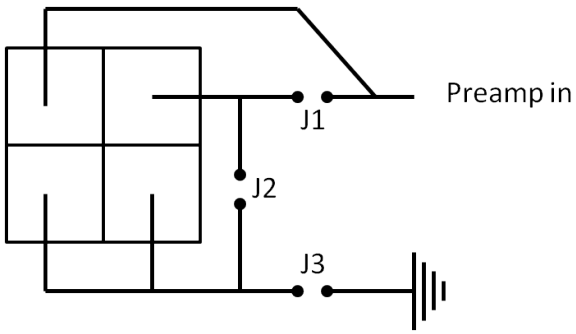

Open	Close	# of pixels to preamp
J1	J2, J3	1
J2	J1, J3	2
J3	J1, J2	4

Figure 4.4: A group of 4 adjacent pixels and the jumper configuration that allows the user to study 1, 2 or 4 pixels together.

A prototype box has been built to study the digitized preamplifier waveform output. It includes a printed circuit board designed to accommodate a total of 24 readout channels and preamplifiers. The detector test board has been designed to read out a large volume of the detector in order to increase the detection efficiency and study the effect of enlarging the size of the pixels on the energy and depth resolution. To study the effect of the pixel size on the energy and depth resolution, a series of jumpers has been added to the design so that the user can choose to couple 2 or 4 pixels together, or simply read out 1 pixel per channel. Figure 4.4

shows a group of 4 adjacent pixels and the jumper configuration needed to couple the pixels. If not coupled, the pixels are grounded. The current electronics does not allow for multiplexing which would allow the user to choose which individual pixel to study. Instead, the pixel configuration is fixed. Figure 4.5 shows the pixel mapping configuration of the 11 × 11 pixelated anode array. As shown in the table of Figure 4.4, the jumper configuration allows changes from 1 pixel to 2 coupled pixels or 4 coupled pixels. The pixel mappings for each of the 1 pixel, 2-coupled and 4-coupled pixel configurations are shown in Figure 4.5 (a), (b) and (c), respectively. The colored pixels are connected to preamplifiers while the white pixels are grounded.

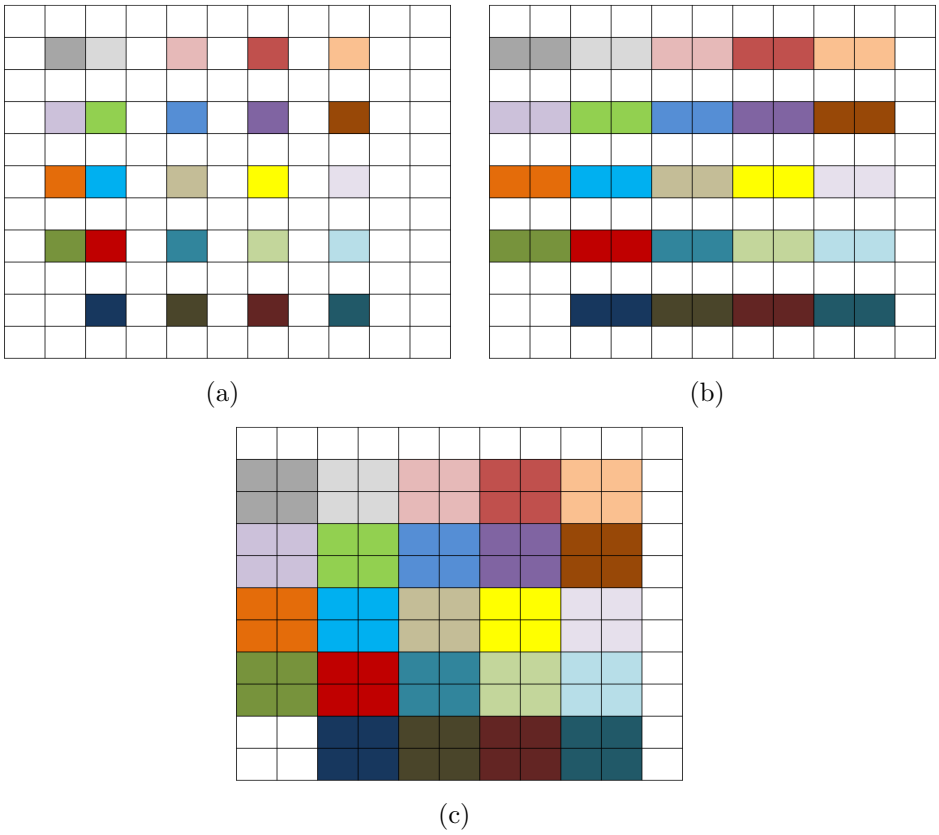

Figure 4.5: Pixel mapping: (a) 1 pixel map, (b) 2-coupled pixel map and (c) 4-coupled pixel map.

The HV bias to the detector's cathode and grid are filtered with an AC network. The charge sensitive preamplifiers are manufactured by Endicott Interconnect Technologies, Inc. They provide a rise time of 20 ns and a fall time of 1030 μs.

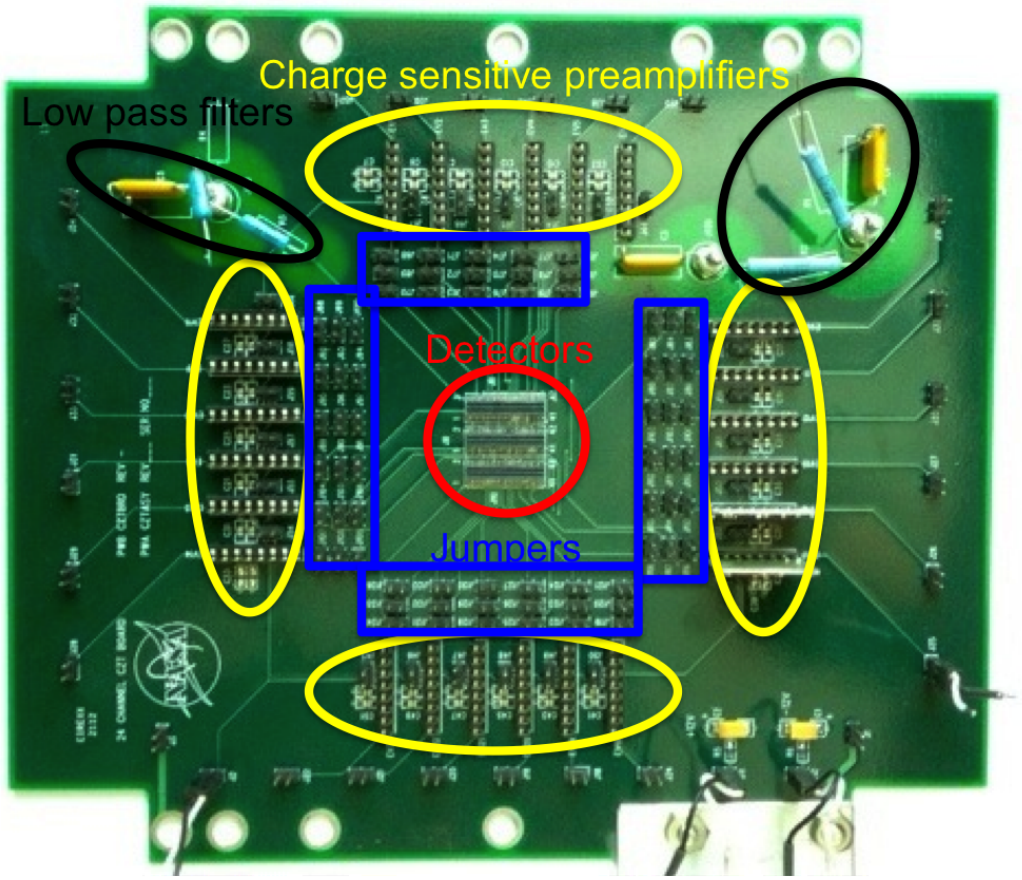

Figure 4.6: Picture of the 24-channel printed circuit board. Only 2 preamplifiers are shown in the picture.

Figure 4.6 is a picture of the printed circuit board before it was placed in the detector box. The detector sits in the middle. The pins of the detector substrate as shown in Figure 4.3, are connected to the preamplifiers through the series of sockets of the 3 connectors that are located in the middle of the board. That way, the detector can easily be removed and another one can be placed for testing. The series of jumpers seen around the detector are used to couple 2 or 4 pixels together, or simply read out 1 pixel per channel as shown in Figure 4.4. The series of connectors located on the outer perimeter of the board serve to connect the charge sensitive preamplifiers. In the same way a detector can easily be replaced, each preamplifier can be removed and replaced, in case of a problem, by disconnecting its pins from the connector's sockets. Finally, the low pass filter seen on top right and left corners of the board are used to

bias the cathode and the grid, respectively.

4.2.2 Digitizer System

The digitizer system is composed of digitizer cards, a chassis and a computer. Three eight-channel Ocotopus Compuscope cards manufactured by DynamicSignals LLC [14] are supported in the chassis and are synchronized to receive the 24 preamplifier outputs. The cards are configured as a Master/Slave set so that one can trigger each card from the channel that receives the signal. In other words, it is possible to identify and store only the channel that has triggered and discard the others. Consequently, it is possible to save space on the disk and speed up the signal processing code. The three cards seat in a chassis that is controlled by a PCI card in the main computer. The chassis offers the possibility to add 9 more cards so that more channels and therefore pixels can be read out in the future via one PC. The ADC resolution of the system is 14 bits and the waveforms are sampled at a rate of 100 MS/s or a sample every 10 ns. The software used to acquire the data was developed in the C language using the necessary Compuscope functions and environment variables provided by DynamicSignals LLC.

Figure 4.7 is a figure of the laboratory equipment for the CdZnTe detector readout system. It includes the CdZnTe detector test box, the 24-channel digital cards and the processing computer and the power supplies for the preamplifiers and cathode high voltage.

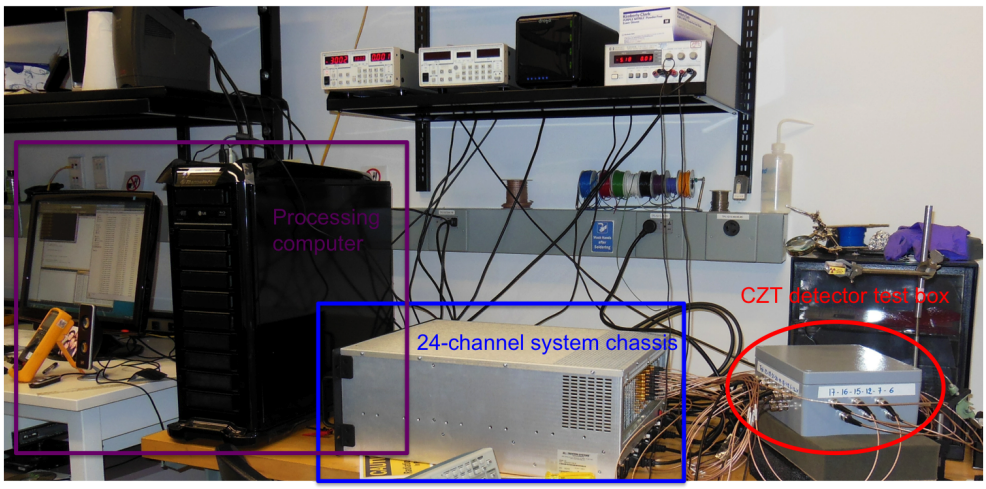

Figure 4.7: Picture of the CdZnTe detector readout system. It includes the CdZnTe detector test box, the 24-channel digital cards, the processing computer and the power supplies for the preamplifiers and cathode high voltage.

CHAPTER V

Spectroscopic Performance of Pixelated CdZnTe Detectors

Large volume pixelated CdZnTe detectors have demonstrated good energy resolution for energies below about 2-3 MeV. They can consistently achieve about 1% FWHM at 662 keV. At higher energies, charge sharing between pixels becomes a problem due to the relatively small size of the pixel compared to the electron cloud. In this chapter, the electron cloud diameter as a function of energy has been simulated using the MCNPX Monte Carlo code. The simulation shows that the electron cloud size is about two times the size of the pixel pitch for a 6 MeV gamma-ray interaction. As the energy of the gamma ray increases, the charge sharing effect becomes dominant. The electron cloud is then collected by multiple pixels, which reduces the spectroscopic performance of the detector due to the weighting potential cross talk. By digitizing the preamplifiers outputs, it is possible to calibrate the adjacent pixels to the collecting pixel in order to correct for the cross talk. Examples of weighting potential cross talk at high energies acquired at the 6 MeV Gamma Facility are shown and a solution for the correction is demonstrated. Using the CdZnTe 24-channel digital system presented in chapter IV, the spectroscopic performance of the detector at 662 keV from ^{137}Cs is presented for 1 pixel and 4 coupled pixels.

5.1 Simulations

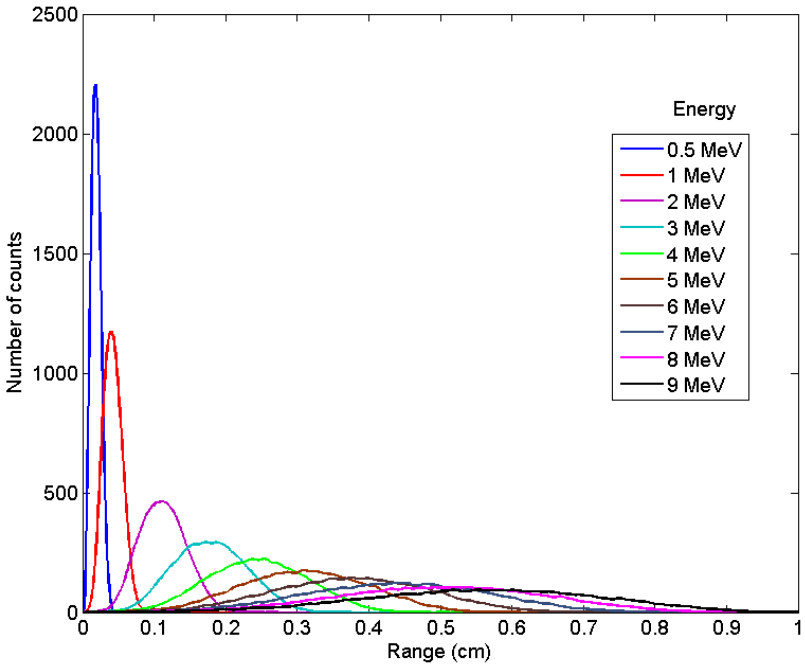

Figure 5.1: Electron cloud dimension for various energies.

5.1.1 Electron Cloud Size

When a photoelectric absorption occurs in a CdZnTe detector, an electron cloud is formed as the photoelectron ionizes the matter. As the energy of the photoelectron increases, the size of the electron cloud gets bigger. In pixelated detectors, if the electron cloud becomes larger than the size of the pixel, the electrons will be collected in both the pixel under which it is produced and its neighbor(s). As a consequence, the charge collected by the central pixel is less than the charge that was initially produced by the photoelectron and results in energy resolution degradation.

A simulation using the MCNPX Monte Carlo [41] code was undertaken to estimate the size of the electron cloud. The simulation tracks the secondary electrons produced by the photoelectrons. The longest distance between two electrons was calculated for

each track and reported in Figure 5.1 for various energies. Each distribution has a Gaussian shape. As the energy increases, the mean of the distribution increases and becomes wider. The mean of each distribution as a function of energy is shown in Figure 5.2. The electron cloud diameter as a function of energy in a CdZnTe detector was simulated for energies up to 10 MeV.

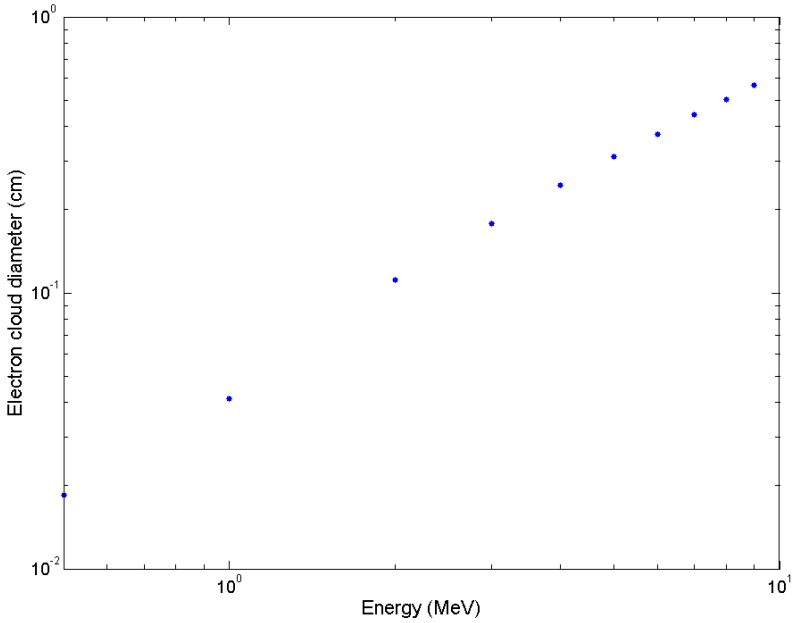

Figure 5.2: Electron cloud diameter as a function of energy.

From Figure 5.2, we can see that the electron cloud diameter is 3.6 mm at 6 MeV. The anode of the CdZnTe detector possesses an 11×11 pixelated array with 1.72 mm pitch. Therefore, the electron cloud is about 2 times the size of the pixel. In addition, as the electrons drift through the volume of the detector, the cloud diffuses. As a consequence, the electron cloud diameter further increases. The diffusion as been modeled in the next section.

5.1.2 Diffusion Model

As the electrons drift toward the anode, where they are collected, they diffuse. The diffusion effect increases the electron cloud diameter. The standard deviation of

the Gaussian-shaped charge carrier is given by equation (5.1) where D is the diffusion coefficient and t is the time elapsed.

$$\sigma = \sqrt{2Dt} \tag{5.1}$$

The diffusion coefficient is given by equation (5.2) where k_B is the Boltzmann constant, T is the temperature, q is the charge and μ is the electron mobility.

$$D = \mu \frac{k_B T}{q} \tag{5.2}$$

Finally, the velocity v can be expressed as the mobility μ times the electric field E:

$$v = \mu E \tag{5.3}$$

The electric field can be expressed as the voltage V divided by the detector thickness Z:

$$E = \frac{V}{Z} \tag{5.4}$$

Using Equations 5.3 and 5.4, the time t can be written as:

$$t = \frac{d}{v} = \frac{d}{\mu E} = \frac{dZ}{\mu V} \tag{5.5}$$

where d is the drift distance. Using Equations 5.5 into Equation 5.1, it becomes:

$$\sigma = \sqrt{\frac{2k_B T dZ}{qV}} \tag{5.6}$$

Figure 5.3 shows the additional increase in diameter as a function of depth of interaction and high voltage in a 15 mm thick CdZnTe detector.

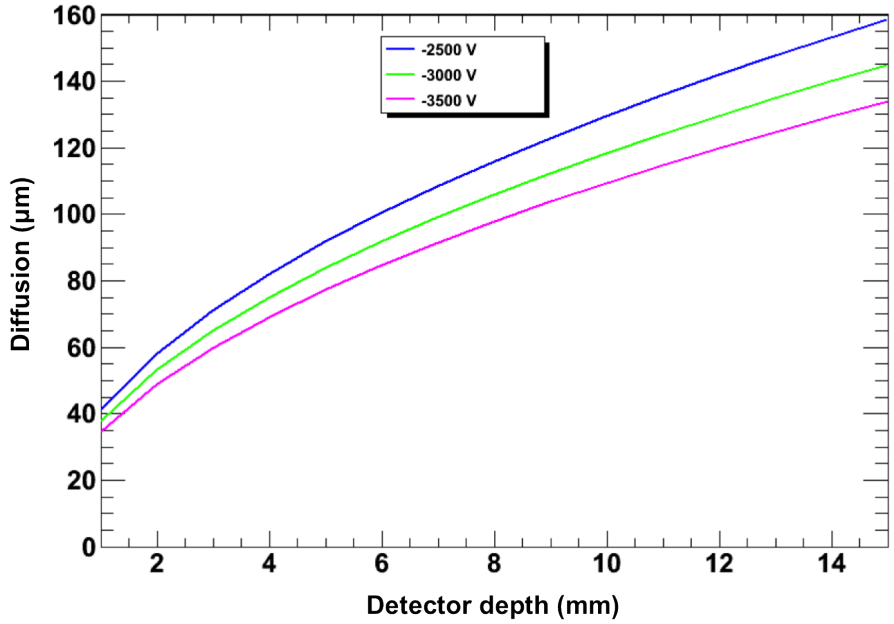

Figure 5.3: Diffusion as a function of depth at -2500 V (blue), -3000 V (green) and -3500 V (red) bias voltage in a 15 mm thick CdZnTe detector.

We can see from Figure 5.3 that the additional increase in diameter has little effect when energies are above 500 keV. Because at 3 MeV the electron cloud diameter is comparable to the pixel pitch of our detectors, we studied the influence of bigger pixels on the energy and depth resolution.

5.1.3 Digital Signal Processing Capabilities

In this work, the waveforms were digitized because it conserves the shape of the preamplifier outputs in order to analyze the details that a traditional peak-hold sys-

tem would lose.

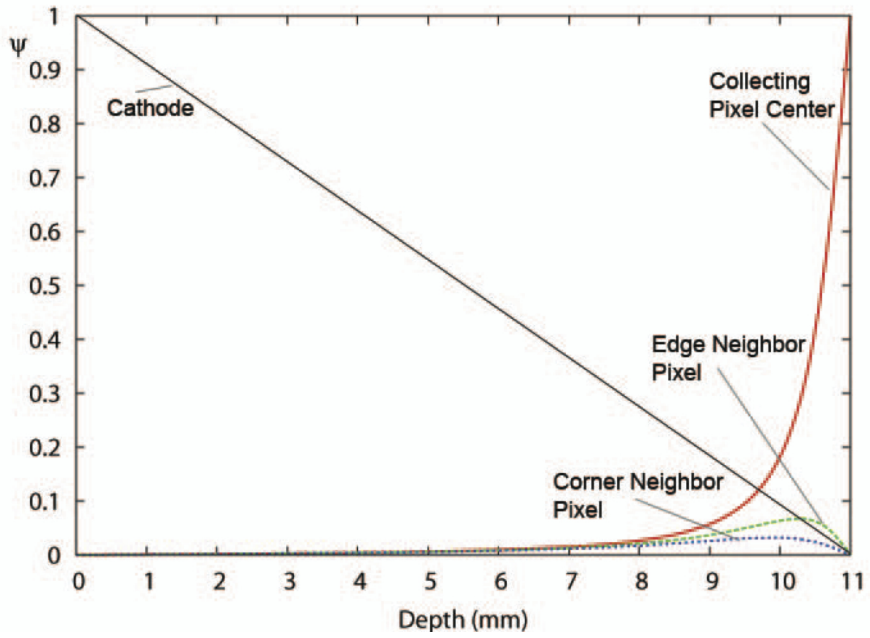

Figure 5.4: Multiple weighting potentials as a function of depth for the cathode, the collecting pixel, a cardinal neighbor pixel, and a corner pixel. The detector modeled in this simulation is an 11 mm thick pixelated HgI_2. [1]

Figure 5.4 shows the weighting potential function simulated with Maxwell 3d software [2] in a 11 mm thick pixelated HgI_2 [1]. The detector has the same electrode geometry as the pixelated CdZnTe detector used in this study. The pixelated anode is a 11 $\times$ 11 pixelated array with a planar cathode. It shows the weighting potential function as a function of depth of the detector for the adjacent pixels. From these results, we can see that when the charge is within about 2-3 mm of the collecting pixel it induces a signal on the adjacent pixel; however, the final weighting potential on the adjacent pixels is zero. Therefore, using Equation 4.3, if the initial interaction occurs close to the pixel, the induced charge on the adjacent pixel becomes negative. As a consequence, the preamplifier output waveform for such interactions shows a negative amplitude. This is referred to as weighting potential cross talk. Therefore, if the electron cloud is collected by multiple pixels due to its large size compared to the collecting pixel, the correction is not as simple as summing up the induced charge

on the adjacent pixels. One must compensate for the negative value induced on the adjacent pixel due to the weighting potential at that depth. It is possible to calibrate each adjacent pixel in order to correct for these negative values. Weighting potential cross talk correction methods can be found in reference [1].

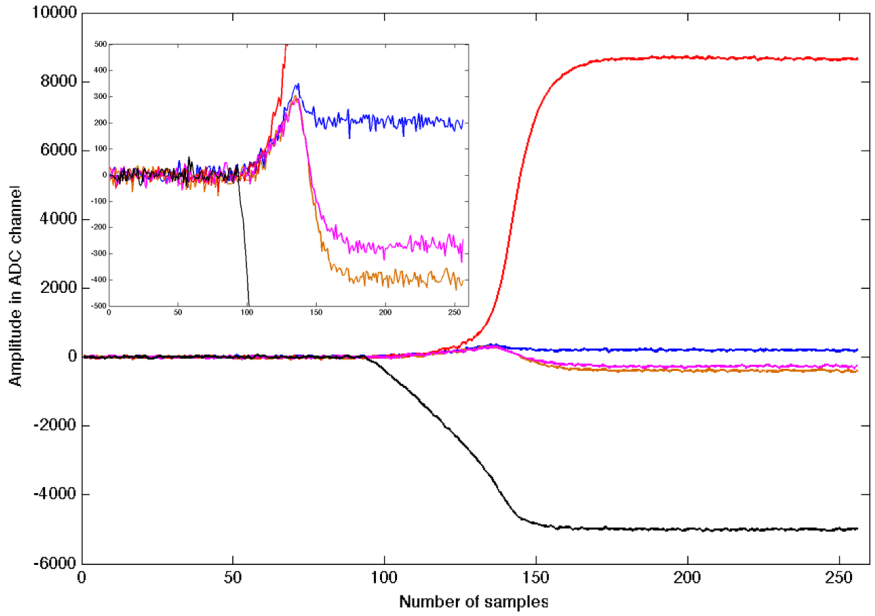

Figure 5.5: Experimental 5 MeV gamma-ray interaction in pixelated CdZnTe detector acquired at the 6 MeV Gamma Facility. The size of the electron cloud induces a negative amplitude on the adjacent pixels.

Figure 5.5 is an example of a waveform where a gamma ray deposited about 5 MeV in the detector and induced a negative signal on the adjacent pixels. This waveform was acquired with the 24-channel system at the 6 MeV Gamma Facility. This example shows the importance of digitizing the outputs and the capabilities of such technologies. However, due to the number of samples acquired by the system for each waveform, the dead time is more significant than for a traditional peak-hold system. The time and memory required to process the data is also greater than a traditional system. In the next section, the experimental data were acquired using the 24-channel system. The software developed to process the data can be used with the next generation ASIC. Gamma Medica, Inc. [21] has been developing ASICs capable

of digitizing the preamplifier outputs of pixelated CdZnTe detectors but the chips are not commercially available yet [21].

5.2 Data Processing Software

Assuming an electron-hole pair-creation energy of 4.64 eV in CdZnTe material [15] and a sensitivity of 3.6 mV/fC for the eV-5093 preamplifers [16], it was calculated that the amplitude at the preamplifier output of a 10 MeV gamma ray is 1.24 V. Therefore, the amplitude range of the GaGe Octopus Compuscope was set to ±2V. A sampling frequency of 100 MHz was chosen and the acquisition trigger was set to 2 or 3% of the amplitude range, depending on the pixel and its associated noise. Given the thickness of the detector of 1.5 cm, the electron mobility 1000 cm^2/V.s in CdZnTe [15] and a cathode bias voltage of -3500 V, it takes 0.64 μs for the electrons to travel from the cathode to the anode side of the detector. Therefore, each time a trigger is received, a total of 256 samples are acquired at a rate of 100 MS/s with 128 samples before and after the trigger. An example of pixel (pink) and cathode (black) waveforms is shown in Figure 5.6.

To process the data, a code using Matlab software [38] was developed. The way to process the data is as follows:

1) apply baseline correction

2) measure the amplitude for pixels and cathode

3) measure cathode to anode amplitude ratio

4) build 3D depth separated spectrum

5) perform energy calibration for each individual pixel at each depth

6) build spectrum

5.2.1 Baseline Correction

The mean of the first 50 samples are measured and the mean value is subtracted for each waveform. Figure 5.6 shows an example of baseline correction for a pixel (pink) and cathode (black) waveforms.

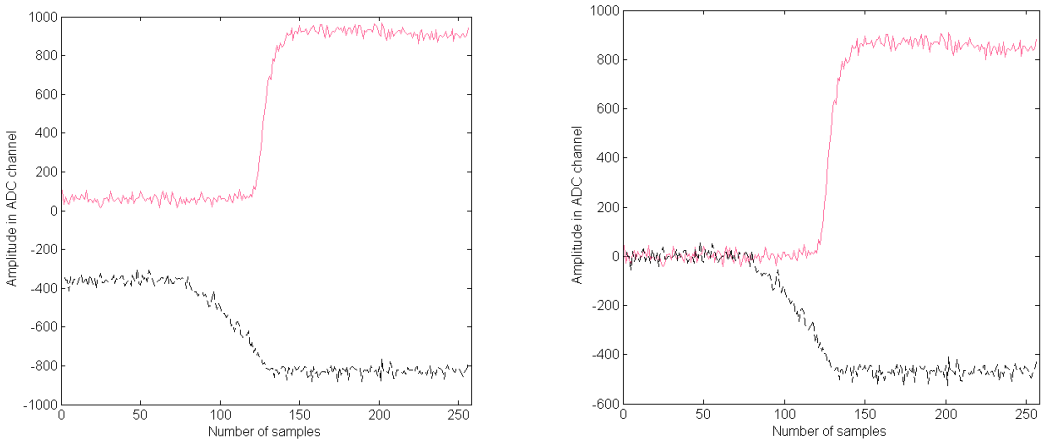

(a) (b)

Figure 5.6: Baseline correction example for pixel (pink) and cathode (black) waveforms. Non-corrected waveforms (a) and corrected waveforms (b) .

5.2.2 Waveform Amplitude

The mean of the first and last 50 samples are measured and the difference between the two mean values is used as the amplitude for each waveform.

5.2.3 3D Depth Separated Spectrum

As explained in chapter IV, the depth z at which the interaction occurs can be determined for a single pixel event by measuring the cathode over anode amplitude ratio using Equation 4.6. An energy spectrum can then be plotted for each depth of the detector and for each pixel. Figure 5.7 shows a ^{137}Cs 3D depth separated spectrum for 1 pixel and 4 coupled pixels. The y-axis represents the depth z of the detector, the x-axis is the energy deposited and the color scale represents the number of counts.

In this example, the thickness of the detector was divided into 60 depths and the thickness of the detector is 1.5 cm. Therefore, the z resolution of the detector is 0.25 mm. Depth 0 represents the anode side of the detector and depth 60 represents the cathode side. In Figure 5.6(b), it can be seen that the amplitude of the cathode and anode signal is about -500 and 900 ADC channel, respectively. The absolute value of the cathode over anode amplitude ratio is about 0.5. Therefore, the z depth for this event is $0.5 \times 60 = 30$ depth units. The energy in ADC channel number is simply the amplitude given by the anode. We observed that the 662 keV peak was located around channel 1300. Therefore, in order to have about a keV per bin, the amplitude of the anode signal was divided by two. In the example given in Figure 5.6(b), the amplitude in ADC channel given by the waveform is about 900. Therefore, the energy is 450 keV in the 3D depth separated spectrum.

5.2.4 Calibration

Figure 5.8 compares the centroid of the 662 keV photopeak from the 3D depth separated spectra shown in Figure 5.7 for 1 pixel and 4 coupled pixels. It can be seen that the position of the photopeak shifts as a function of depth. The 662 keV photopeak was fit by a gaussian function at each depth and the mean was reported in Figure 5.8. The shape of the centroid for 1 pixel (blue line) can be explained as follows: at small depths, which correspond to depths close to the anode side of the detector, the shape can be explained by the weighting potential function. As shown in Figure 4.2, the weighting potential of the pixel increases to one exponentially when the depth of interaction z is in the vicinity of the anode side. At large depths, which correspond to depths close to the cathode side of the detector, the shape can be explained by electron trapping. When an interaction occurs close to the cathode side of the detector, the electrons drift toward the anode and are more likely to get trapped than on the anode side of the detector. Therefore, the amount of charge collected

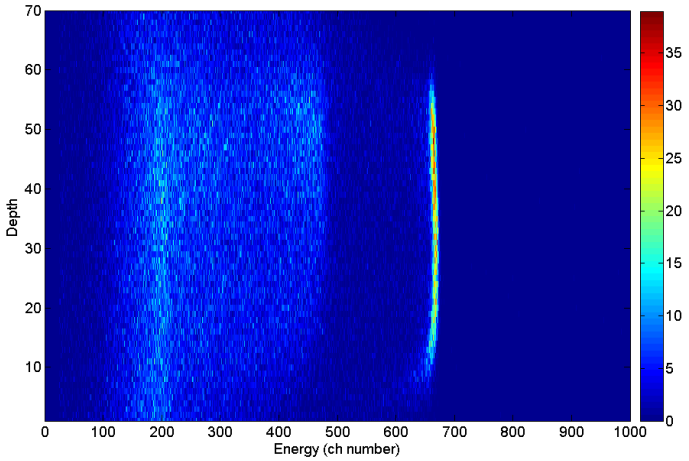

(a)

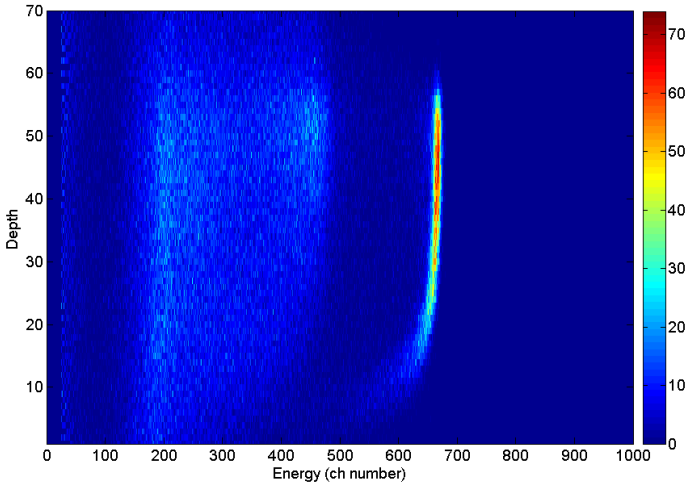

(b)

Figure 5.7: Experimental ^{137}Cs 3D depth separated spectrum for 1 pixel (a) and 4 coupled pixels (b).

for interactions that occur on the cathode side of the detector is smaller than on the anode side of the detector due to electron trapping.

The shape at small depths of the centroid for 4 coupled pixels can be explained similarly to that of 1 pixel. The difference takes place in the fact that the weighting potential function will rise slower than for 1 pixel because the pixel size for 4 coupled pixels is bigger. At large depths, the electron trapping is not observed. This can be due to the non-uniformity of each of the 4 pixels and also to the fact that the

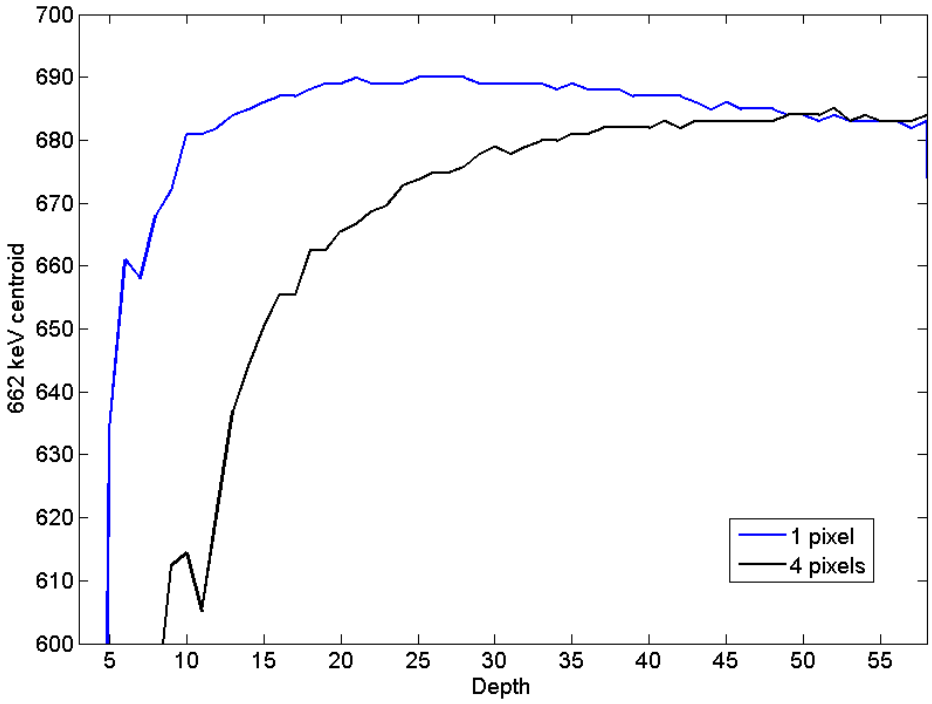

Figure 5.8: 662 keV photopeak centroid comparison for 1 pixel (blue) and 4 coupled pixel (black). Depth 0 represents the anode side of the detector and depth 60 represents the cathode side.

weighting potential rises so slowly that the effect is still present at depths in the middle of the detector.

The shift of the position of the photopeak as a function of depth created a gain variation that can be corrected for. Equation 5.7 for 1 pixel and 5.8 for 4 coupled pixels were used to fit the data:

$$f(z) = C - Bz - A.exp\left(-\frac{z}{\tau}\right) \qquad for\ 1\ pixel \tag{5.7}$$

$$f(z) = C - A.exp\left(-\frac{z}{\tau}\right) \qquad for\ 4\ coupled\ pixels \tag{5.8}$$

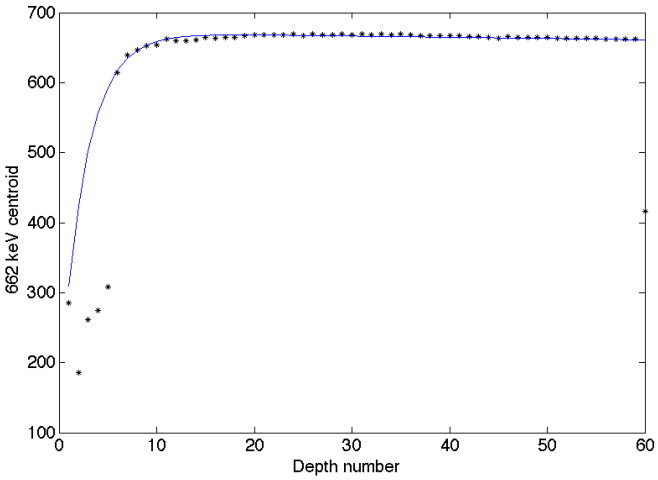

(a)

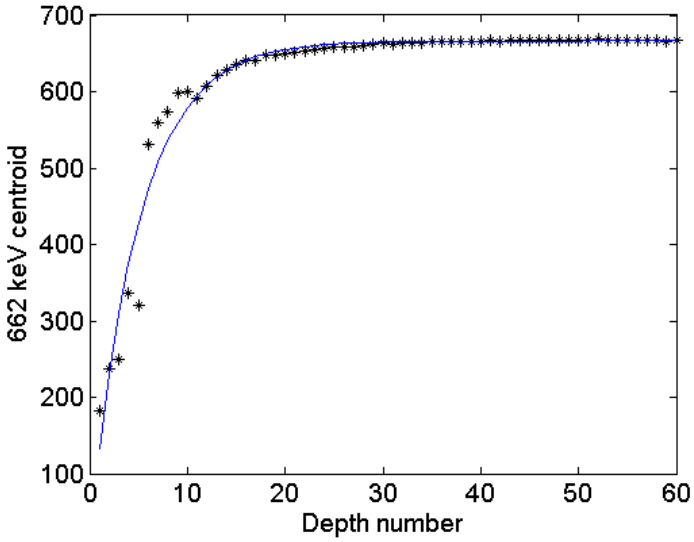

(b)

Figure 5.9: 662 keV photopeak centroid (stars) as a function of detector depth and fit function (blue line) for 1 pixel (a) and 4 coupled pixels (b).

Figure 5.9 shows the 662 keV photopeak centroid (stars) as a function of detector depth and fit functions (blue line) for 1 pixel (a) and 4 coupled pixels (b). Equations 5.7 and 5.8 were used to fit the data points of Figure 5.9 (a) and (b), respectively. The ouliers at small depths are due to the low number of counts in the photopeak at these depths in Figure 5.7.

In order to improve the spectroscopic performance of the detector, a gain cor-

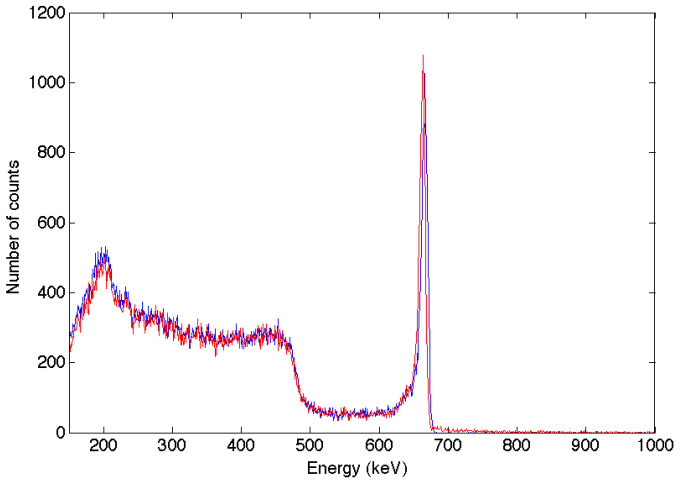

(a)

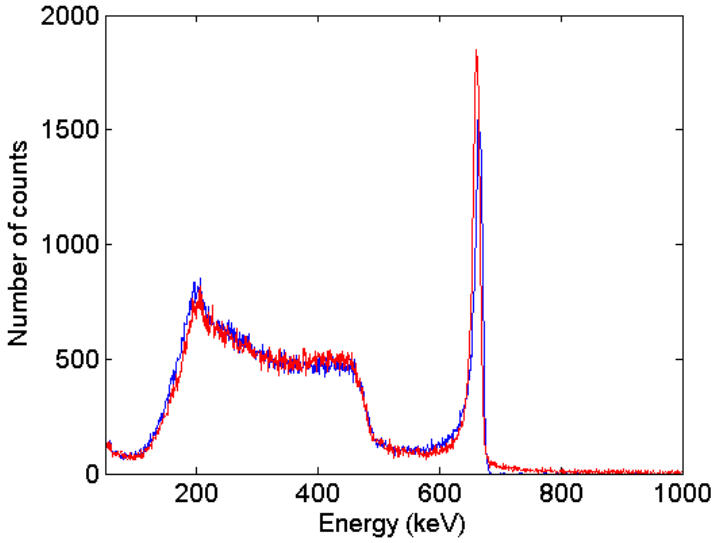

(b)

Figure 5.10: Experimental ^{137}Cs spectrum before (blue) and after (red) gain correction and calibration for 1 pixel (a) and 4 coupled pixels (b).

rection can be applied at each depth using the parameters from the fit functions. Figure 5.10 shows the ^{137}Cs spectra before and after the gain correction was applied to the data. The single pixel resolution is 1.4 % and 2.2 % FWHM at 662 keV for 1 pixel and 4 coupled pixel, respectively.

CHAPTER VI

Imaging Performance of Pixelated CdZnTe Detectors

We have seen in the previous chapter that as the energy of the gamma ray increases, the charge sharing effect becomes dominant and the electron cloud is collected by multiple pixels. As the pixel size increases, the effect of charge sharing decreases but the imaging efficiency and angular resolution of the detector are degraded due to the decrease in position resolution. Simulations were undertaken to produce images of point sources with increasing pixel size. The imaging capabilities of pixelated CdZnTe detectors can be used to locate the direction of radioactive sources. Therefore, it is possible to differentiate gamma rays coming from a source placed above the detector versus a source below the detector. In planetary science, this capability allows one to discard the gamma rays coming from a rover or lander on a planetary surface and thus increases the sensitivity of the detector to the gamma rays coming from the planetary surface. Simulations were undertaken to study the increase in sensitivity that pixelated CdZnTe detectors can achieve using Compton imaging techniques.

6.1 Compton Imaging

By increasing the size of the pixel pitch, we can reduce charge sharing at high energy and better spectroscopic performance can be achieved. However, the lateral position resolution is bigger with increasing pixel size thus affecting the imaging efficiency and the angular resolution of the detector. In this section, imaging efficiency and angular resolution of 662 keV photons are simulated.

6.1.1 Compton Efficiency

The efficiency of Compton imaging for a 2 cm $\times$ 2 cm $\times$ 1.5 cm pixelated CdZnTe detector with 1.72 mm pixel pitch and 3.44 mm pixel pitch was studied by simulating the number of the incoming photons that are Compton scattered and then photoelectrically absorbed within the detector. The simulations were performed using MCNP-PoliMi software [33] to measure the exact location and energy deposited of each interaction in the detector. The source is monenergetic producing 662 keV photons and placed at 1 m away from the center of the detector.

Figure 6.1 shows the number of times that a 662 keV photon deposited the full energy of 662 keV in the detector via the photoelectric process. This type of event is reported as a one-interaction event on the x-axis. The y-axis represents the number of counts. If a 662 keV photon was Compton scattered and then photoelectrically absorbed and the sum of the energy deposited is 662 keV, it is reported as a two-interaction event on the x-axis. The blue bars represent the Compton efficiency for a detector where the position of each photon is known with an accuracy of 100 μm. The green and red bars represent the Compton efficiency for a detector with 1.72 mm and 3.44 mm pixel pitch, respectively. If a two-interaction event occurs in the detector under the same pixel, it is not possible to distinguish the two photons. This type of event will be seen as a one-interaction event instead, with photon energy of the sum of the two-photon energies. Only two-interaction events can be used to reconstruct

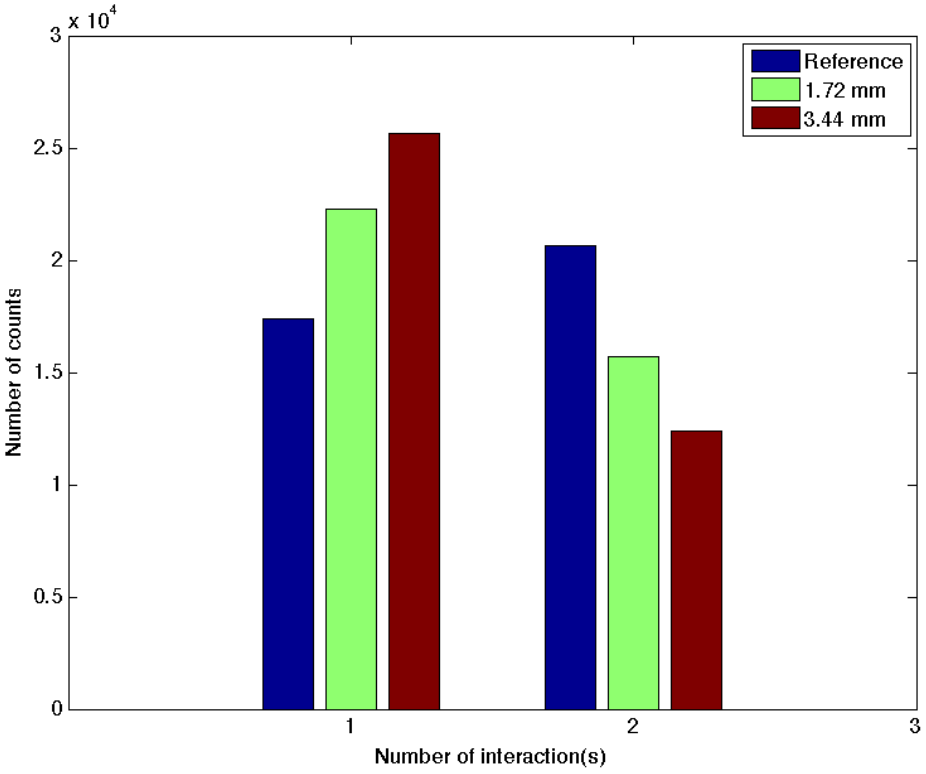

Figure 6.1: Interaction number in a 2 cm × 2 cm × 1.5 cm CdZnTe detector at 662 keV for a perfect detector, 1.72 mm and 3.44 mm pixel pitch pixelated detector.

the Compton ring for imaging. Therefore, two-interaction events that occur under the same pixel cannot be used to reconstruct the Compton ring for imaging. As the size of the pixel increase, the imaging efficiency of the detector decreases and the statistics of the point spread function are smaller.

6.1.2 Angular Resolution

The contributing factors to the angular resolution of the point spread function are the energy uncertainty due to the detector energy resolution, the Doppler effect in CdZnTe material and the position uncertainty due to the finite size of the pixels. The angle theta at which the scattered photon is deflected is measured as a function of the energies deposited in the detectors. Therefore, the energy uncertainty and

the Doppler effect result in an uncertainty in the measured photon scatter angle. The uncertainty in positions due to the finite pixel size of the detector results in an uncertainty in the measure of the cone axis.

6.1.2.1 Energy Uncertainty

The full width half maximum (FWHM) of a peak can be defined as [26]:

$$FWHM^2 = W_d^2 + W_e^2 \tag{6.1}$$

W_d^2 represents the inherent statistical fluctuation in the number of charge carriers created.

$$W_d^2 = 2.35^2 FE\epsilon \tag{6.2}$$

where F is the Fano factor, E is the energy and ϵ is the electron-hole pair creation energy. W_e^2 represents the electronic noise of the system. In semiconductor materials, the Fano factor is usually less than one, and the measured value for CdZnTe is around 0.1 [31]. However, other statistical factors can contribute to the energy resolution with pixelated CdZnTe detector, such as the depth uncertainty and electron trapping. To account for this effect, based on the measured resolutions at different gamma-ray energies, a Fano factor of unity was assumed. With the assumption of a Fano factor of 1, W_e^2 taken as 5 keV and the electron-hole pair creation energy as 4.64 eV [15], the overall $FWHM$ at 662 keV is 1%, which is what was observed experimentally for single pixel event with the 1 pixel 24-channel system. Therefore, the overall $FWHM$ can be written as follows:

$$FWHM = \sqrt{25 + 2.35^2 FE\epsilon} \tag{6.3}$$

The energy resolution is defined as:

$$\Delta E = \frac{FWHM}{E} \tag{6.4}$$

From the Compton formula, the photon scattering angle is given by:

$$\theta = arccos\left(1 + \frac{m_e c^2}{E_1 + E_2} - \frac{m_e c^2}{E_2}\right) \tag{6.5}$$

where E_1 and E_2 are energies of the electron and scattered photon, respectively.

The scattering angle uncertainty for a two-interaction event is calculated by applying the error propagation to Equation 6.5:

$$\Delta\theta = \frac{m_e c^2}{(E_1 + E_2)^2 E_2^2 sin\theta}\sqrt{E_2^4 \Delta E_1^2 + (E_1^2 + 2E_1E_2)^2 \Delta E_2^2} \tag{6.6}$$

Figure 6.2 shows the angular uncertainty as a function of the photon scattering angle for various energies. The angular uncertainty decreases with increasing energies because the resolution gets better as the energy increases.

6.1.2.2 Doppler Effect

The Compton formula as shown in Equation 6.5 is based on the assumption that the electron is free and at rest. Doppler broadening uncertainties take into account the effects of bound electrons in an atom on the angular distribution of the scattered photon. Bound electrons carry momentum, which can add or subtract to the mo-

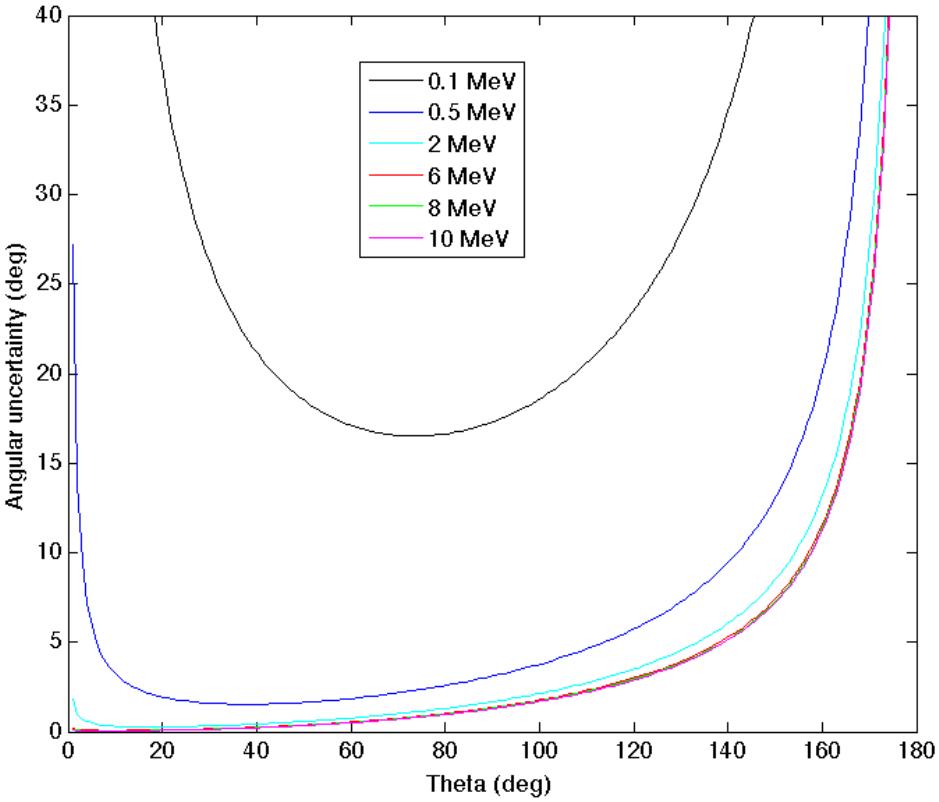

Figure 6.2: Angular uncertainty due to detector energy uncertainty for various initial photon energies.

mentum of the scattered photon. The Compton profiles are used to account for the effects of a bound electron on the energy distribution of the scattered photon. The analytical one-electron Compton profiles can be approximated by [12]:

$$J_i(p_z) = \sqrt{2}J_{i,0}\left(\frac{\sqrt{2}}{2} + \sqrt{2}J_{i,0}|p_z|\right) exp\left[\frac{1}{2} - \left(\frac{\sqrt{2}}{2} + \sqrt{2}J_{i,0}|p_z|\right)^2\right] \tag{6.7}$$

where $J_{i,0}$ is the value of the profile at $p_z = 0$ obtained from the tables of Hartree-Fock Compton profiles published by Biggs [8] and p_z is the projection of the electron momentum on the scattering vector defined as [3]:

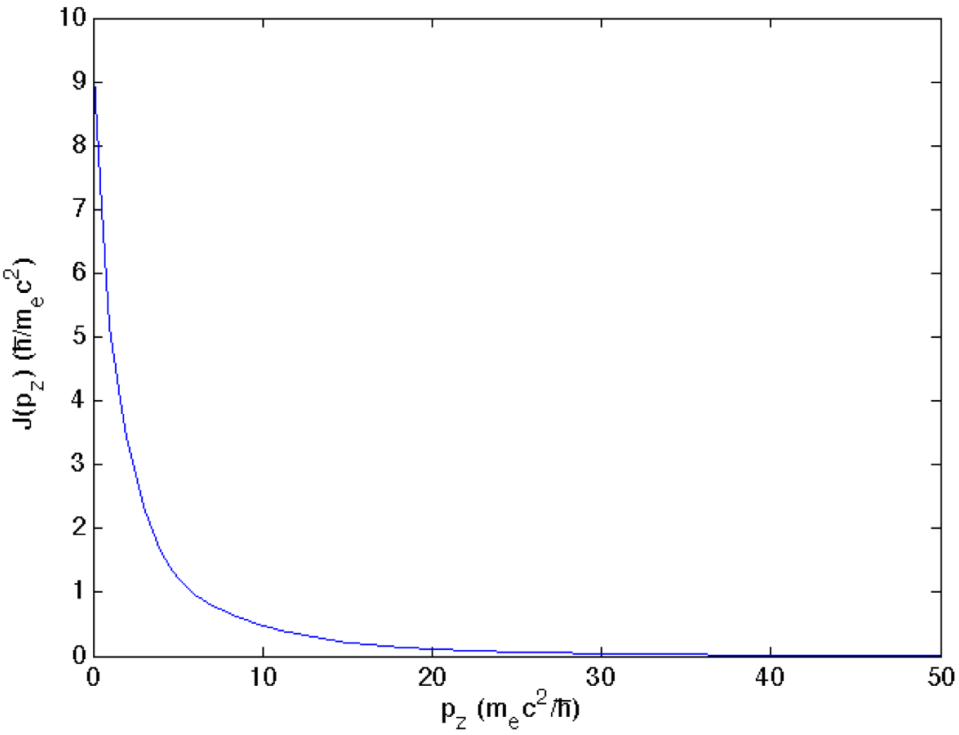

Figure 6.3: Compton profile for $Cd_{0.45}Zn_{0.05}Te_{0.5}$.

$$p_z = -137\frac{E_0 - E_2 - E_0E_2\frac{(1-cos\theta)}{m_ec^2}}{\sqrt{E_0^2 + E_2^2 - 2E_0E_2cos\theta}} \tag{6.8}$$

The analytical Compton profile $J(p_z)$ as a function of p_z for $Cd_{0.45}Zn_{0.05}Te_{0.5}$ is shown in Figure 6.3.

The energy distribution of the scattered photon is given by the double differential cross section [13]:

$$\frac{d\sigma}{d\Omega dE_2'} = \frac{1}{2}m_e r_0^2\sqrt{(E_2^2 + E_2'^2 - 2E_2E_2'cos\theta)}\frac{E_{2'}}{E_0}\left(\frac{E_2'}{E_0} + \frac{E_0}{E_2'} - sin^2\theta\right)J(p_z) \tag{6.9}$$

where E_2 is the energy of the scattered photon as defined in the Compton scattering formula. Equation 6.5, E_2' is the energy of the scattered photon in the case of an

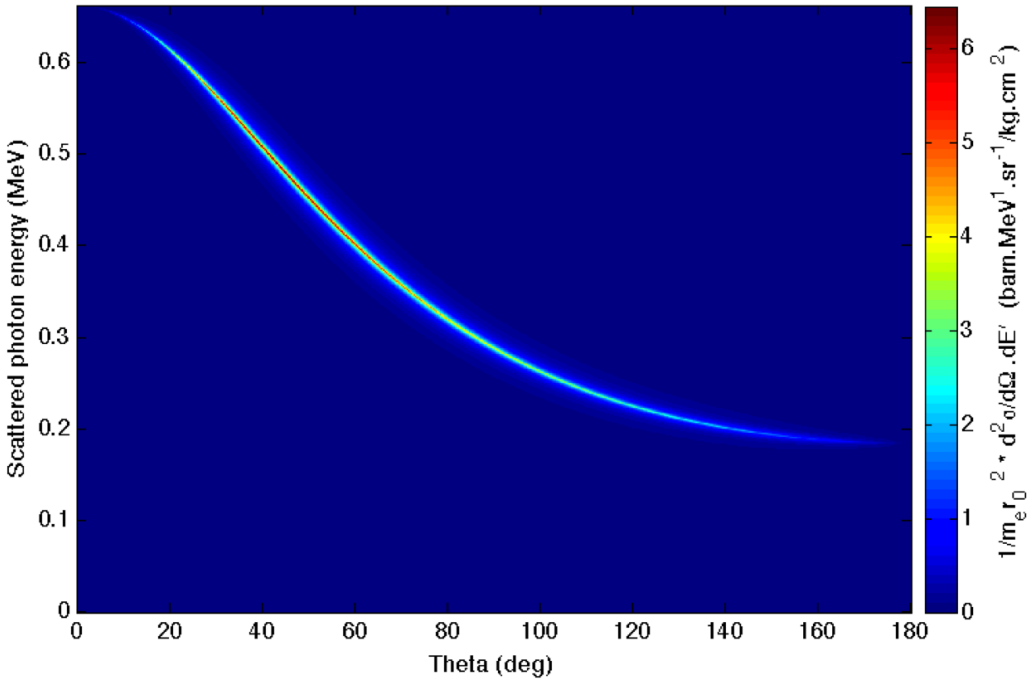

Figure 6.4: Double differential cross section for CdZnTe for 662 keV photons.

interaction with an electron bound to the atom and not at rest, E_0 is the energy of the initial photon, θ is the scattering angle of the photon and $\mathrm{J}(\mathrm{p}_z)$ is the Compton profile for element with atomic number Z.

Figure 6.4 shows the double differential cross section for CdZnTe at 662 keV for different scattered photon energies. The distribution for a given energy is non-Gaussian as shown in Figure 6.5 for various scattered photon energies. Therefore, the angular uncertainty was defined as the FWHM of the distribution.

The angular uncertainty as a function or the scattering angle θ can be seen in Figure 6.6. As the scattering angle increases, which corresponds to low scattered photon energies, the angular uncertainty increases.

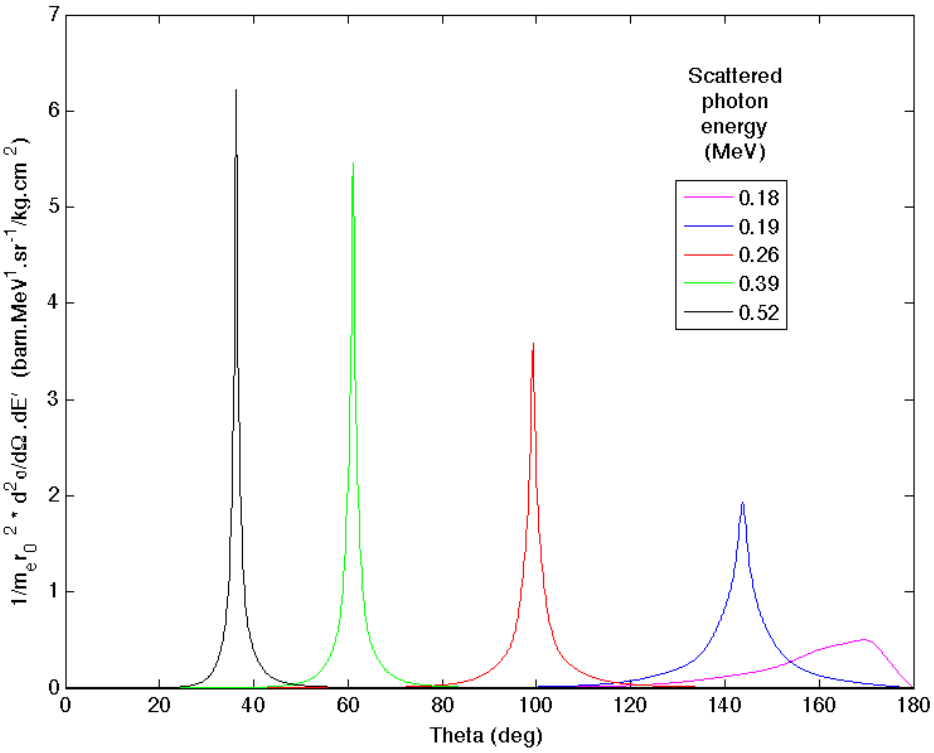

Figure 6.5: Double differiential cross section in CdZnTe for 662 keV for various scattered photon energies.

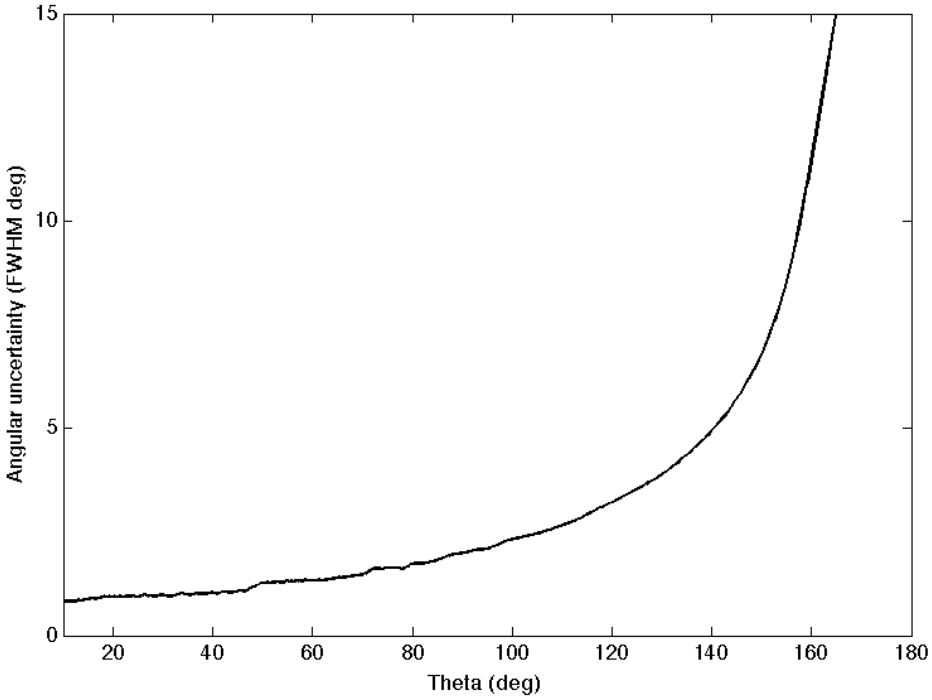

Figure 6.6: FWHM angular uncertainty as a function of the scattering angle θ for 662 keV photons in CdZnTe.

6.1.3 Position Uncertainty

The position resolution are about 1.72 mm on the lateral direction for the 1 pixel detector and 3.44 mm for the 4-coupled pixel detector. As explained in section 5.2.3, the resolution on the depth of interaction is about 0.25 mm. It is possible to use backprojection reconstruction if two interactions deposit energy in two different pixel in the detector. The x, y and z coordinates of the two interactions gives a measure of the cone axis direction. Therefore, the uncertainties in the x, y and z coordinates of each interaction introduces an uncertainty in the direction of the cone axis.

The azimuthal and altitude angles ϕ and θ, respectively can be written as:

$$\phi = arctan\frac{y_2 - y_1}{x_2 - x_1} \tag{6.10}$$

$$\theta = arctan\frac{z_2 - z_1}{\sqrt{(x_2 - x_1)^2 + (y_2 - y_1)^2}} \tag{6.11}$$

The uncertainties in the azimuthal and altitude angle are calculated by applying the error propagation to Equations 6.10 and 6.11:

$$\sigma_\phi^2 = \frac{1}{(x_2 - x_1)^2 + (y_2 - y_1)^2}\frac{p^2}{6} \tag{6.12}$$

$$\sigma_\theta^2 = \frac{\frac{p^2}{6}(z_2 - z_1)^2 + 2((x_2 - x_1)^2 + (y_2 - y_1)^2)\Delta z^2}{(x_2 - x_1)^2 + (y_2 - y_1)^2 + (z_2 - z_1)^2} \tag{6.13}$$

where p is the pitch of the pixel and Δz is the uncertainty in the depth of interaction. The factor $p^2/6$ is the square of the root mean square (RMS) resolution for a pixelated detector with pixel pitch p.

Xu *et al.* have shown that the angular uncertainty can be modeled if we introduce another angular uncertainty $\sigma_{\theta'}$ as shown in Figure 6.7 to be the angular uncertainty of the axis in the azimuthal direction before it is projected onto the x-y plane [42]:

$$\sigma_{\phi'} = 2arctan(tan(\sigma_\phi/2)sin\theta) \tag{6.14}$$

The uncertainty in the direction of the cone axis is then determined by the uncertainties in two orthogonal angular directions, which are $\sigma_{\phi'}$ and σ_θ. Assuming the spread of the backprojection cone at a specific direction β is Gaussian, the standard deviation is approximated by:

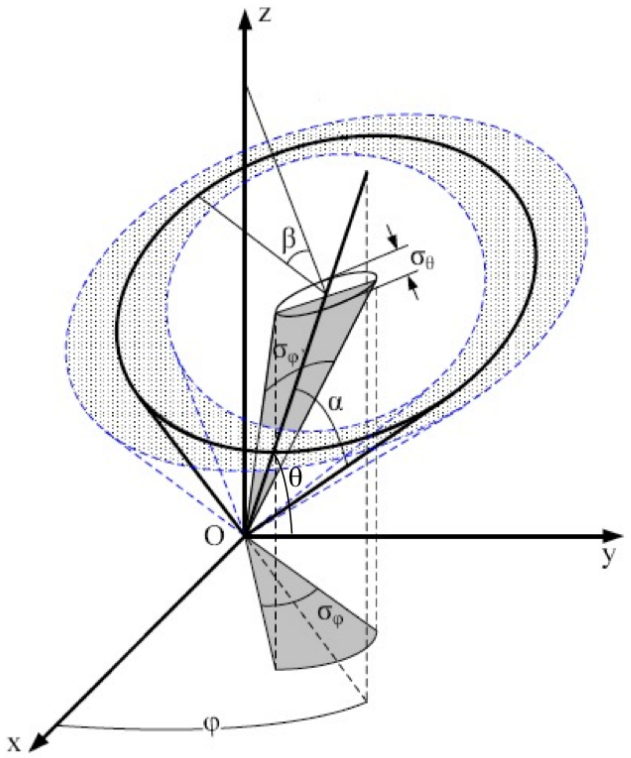

Figure 6.7: Angular uncertainty due to position uncertainties. The uncertainty in positions due to the finite pixel size of the detector results in an uncertainty in the measure of the cone axis.

$$\sigma_\beta = \sigma_\theta cos^2\beta + \sigma_{\phi'} sin^2\beta \tag{6.15}$$

Xu *et al.* compared this angular uncertainty model to simulations, and they found that this model is a good approximation except for very large and small scattering angles.

6.1.4 Point Spread Function Simulations

The simulated point spread functions for full energy deposition, two-interaction events are shown in Figure 6.8 for (a) a perfect detector where the interaction location of each photon is know with a 100 μm accuracy, (b) a 1.72 mm and (c) 3.44 mm pixel pitch pixelated detector, respectively. The detector is 2 cm $\times$ 2 cm $\times$ 1.5 cm. The sum of the energy deposited by each interaction is always 662 keV. The source is placed directly above the detector, 1 m away from its center.

The point spread functions show that the distribution in the azimuthal direction is not uniform for pixelated detectors of 1.72 mm and 3.44 mm pixel pitch. Figure 6.9 shows the cross section of the point spread function on the azimuthal direction for an altitude of 0°.

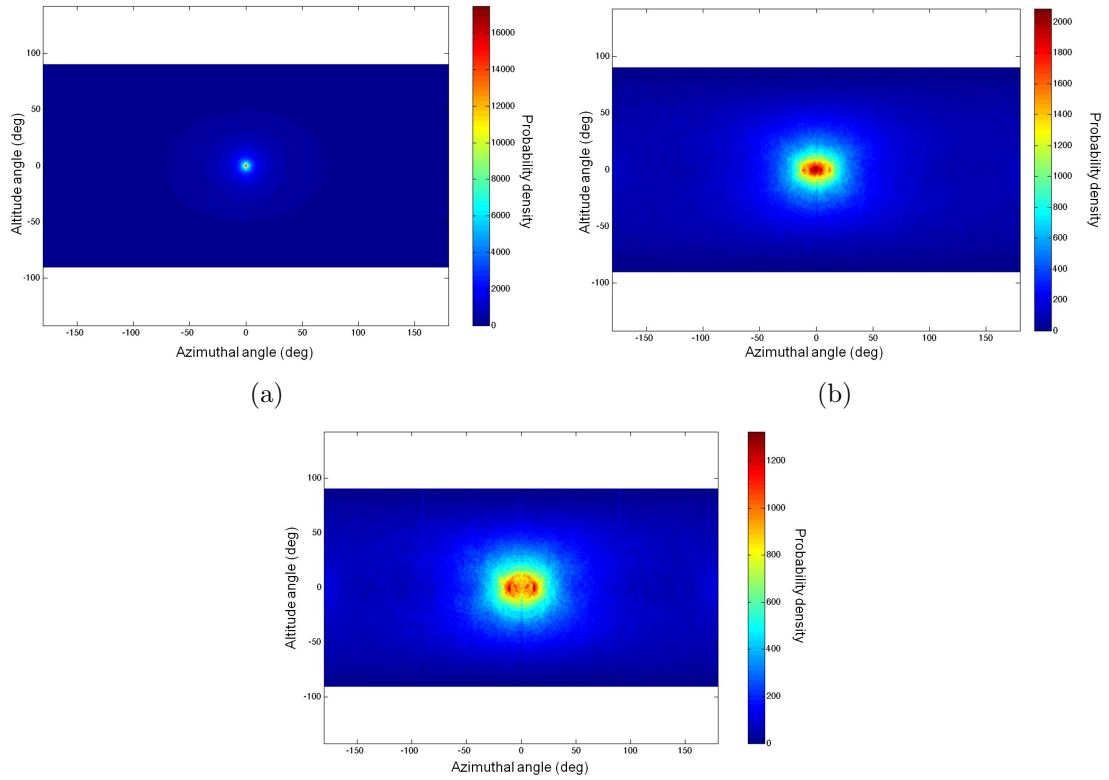

Figure 6.8: Simulated point spread function for (a) perfect detector ,(b) 1.72 mm and (c) 3.44 mm pixel pitch pixelated CdZnTe detector at 662 keV.

The shape of the distribution seen in Figures 6.8 (b) and (c) is caused by the lateral position resolution on the x- and y-axis. As a consequence, the events that occur in adjacent pixels cause the discretization of the azimuthal angle. For a set of a central pixel surrounded with 8 adjacent pixels, the azimuthal angles can take values of 0°, 45°, 90°, 135°, 180°, 225°, 270° and 360°. The distribution on the altitude angle does not suffer the same problem because the depth of the interaction is known with an accuracy of 0.1 mm.

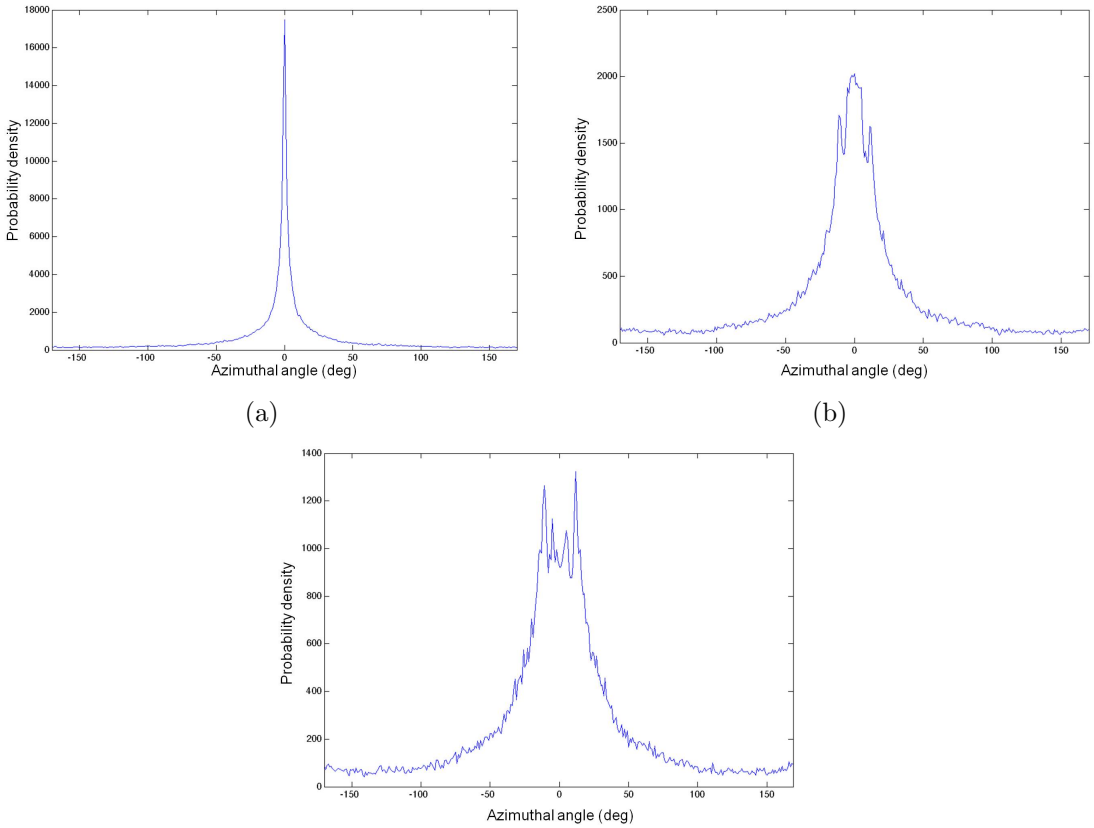

Figure 6.9: Cross section of the simulated point spread function on the azimuthal direction for an altitude of 0° for perfect detector (a), 1.72 mm (b) and 3.44 mm (c) pixel pitch pixelated CdZnTe detector.

In order to get a uniform distribution, the events that have a greater length than the pixel pitch are selected. Figure 6.10 shows the simulated point spread functions for a 1.72 mm pixel pitch CdZnTe detector when events with lengths greater than 1.72 mm (a), 3.44 mm (b) and 5.16 mm (c) are selected for the reconstruction. The corresponding scatter angle θ distribution is shown in Figure 6.11. As the length of the selected events increases, the θ distribution is more uniform. The number of θ angles with high values decreases, which correspond to scattered photon with low energies. Photons with higher energies can interact further away from the first interaction. Therefore, the two interactions are less likely to happen in adjacent pixels, thus increasing the uniformity of the azimuthal distribution.

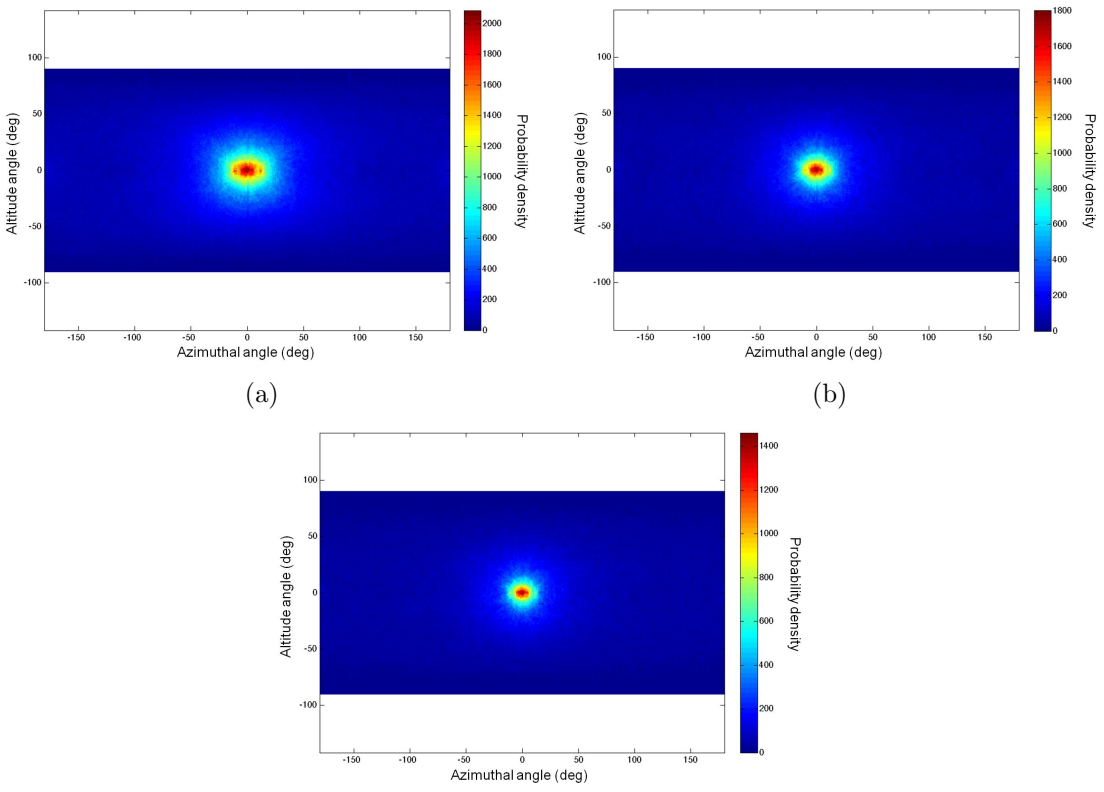

Figure 6.10: Simulated point spread function for 1.72 mm pixelated CdZnTe detector for events with lengths above 1.72 mm (a), 3.44 mm (b) and 5.16 mm (c).

To measure the angular resolution, the point spread functions where events with lenghts greater than 5.16 mm were chosen for the case of pixelated detectors. The angular resolution is measured as the angle at which 68% of the total number of counts is contained. It was measured to be 5°, 16° and 22° for the perfect detector, the 1.72 mm and 3.44 mm pixel pitch pixelated detector, respectively.

6.2 Sensitivity Study

The instruments in PING are designed so that the PNG and the neutron and gamma-ray detectors sit underneath the rover but are positioned as close as possible to the planetary surface. The imaging capabilities of pixelated CdZnTe detectors

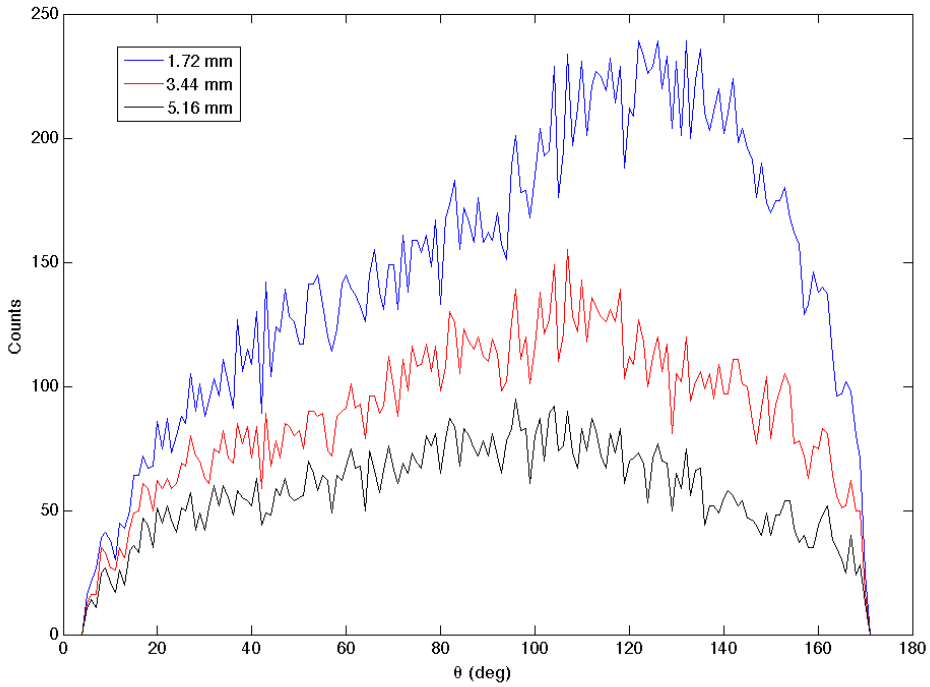

Figure 6.11: Scatter angle θ distribution for events with lengths greater than 1.72 mm, 3.44 mm and 5.16 mm.

make it possible to discard some of the gamma rays coming from the rover above therefore improving the sensitivity to the gamma rays coming from the planet below.

In order to study the improvement in sensitivity to the gamma rays originating from the planetary surface with pixelated CdZnTe detectors, we modeled a configuration in which the PNG is used to activate a slab of granite to produce characteristic gamma rays. We simulated only the prompt gamma rays that result from the activation of granite. These gamma rays result from the inelastic scattering reactions with the elements in the granite. This configuration corresponds to the inelastic scattering reaction time configuration window shown in red in Figure 2.4. A ^{137}Cs source is placed above the CdZnTe detectors in order to characterize the number of gamma rays coming from the source that can be rejected from the energy spectrum acquired by the CdZnTe detectors using Compton imaging. This configuration was chosen because it can be reproduced at our test facility at GGAO. This simulation model

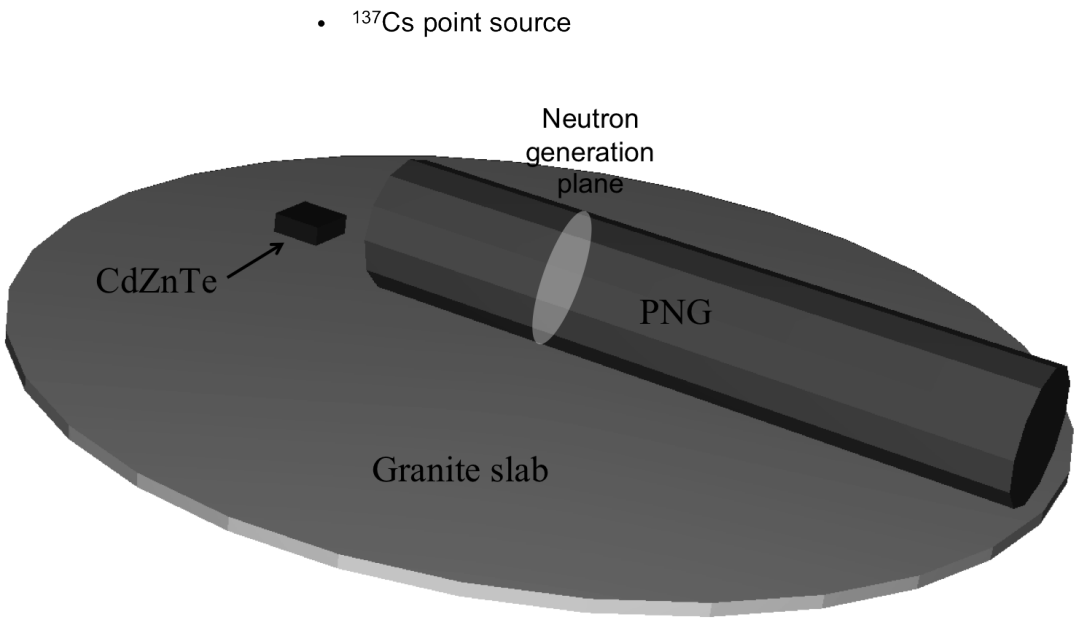

Figure 6.12: Geometry of the model used in the sensitivity simulation.

includes the following components:

1) A slab of granite rests 2 cm below the detector. It is 2 cm thick and 40 cm in radius.

2) A ^{137}Cs point source is placed 50 cm above the detector,

3) The PNG tube. The detector is placed 20 cm away from the origin of the neutron generation plane. The neutrons are emitted from the center of the plane.

4) The detector is an array of 2 × 2 large volume pixelated CdZnTe crystals of 2 cm × 2 cm × 1.5 cm each. The pixel pitch is 1.72 mm.

The geometry of the model used in the simulation is shown in Figure 6.12.

The main component of granite is SiO_2 and represents above 70% of its composition. Therefore, for simplicity, the material for our granite slab was modeled as 100% SiO_2. Figure 6.13 shows the simulated response of the detectors to both the SiO_2 slab and the PNG together (black spectrum), and the ^{137}Cs source (blue spectrum), separately. The black spectrum shown in Figure 6.13 is the response of the detectors

to the elements that are not above the detectors and therefore is used as a reference. It will be referred to as the reference spectrum. The sum of the two spectra is the response of the detector to the first three components described above and is shown in Figure 6.15 in red. In the rest of the discussion, it will be referred to as as the summed spectrum. By using Compton imaging techniques, we expect to reject gamma rays from the summed spectrum so that the resulting spectrum is as close as possible to the reference spectrum. In this simulation, the energy uncertainties, the Doppler effect and the position uncertainties due to the pixels of the detectors were modeled.

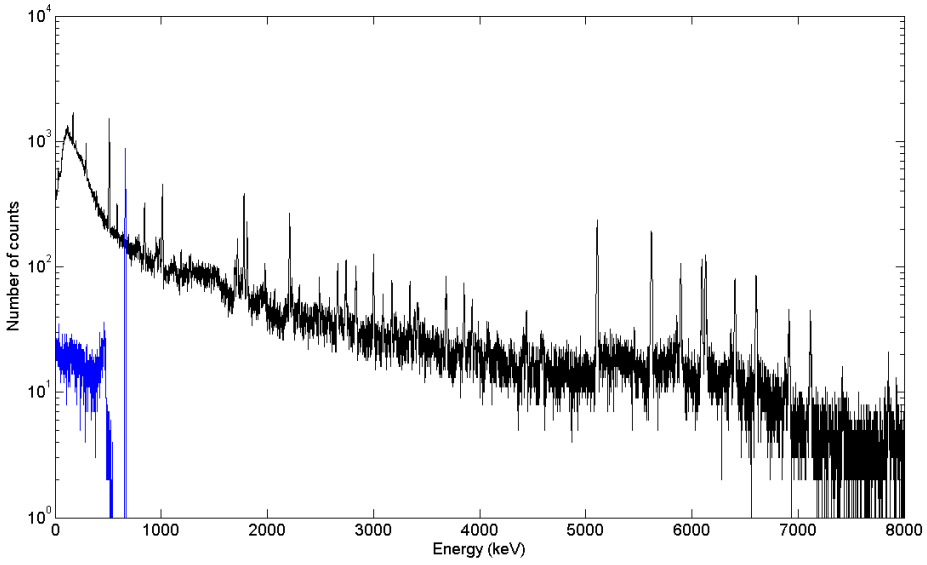

Figure 6.13: CdZnTe detector response to both activated SiO_2 and PNG and ^{137}Cs.

6.2.1 Full-energy Compton Rejection Method

The methodology to study the sensitivity improvement achieved with the detectors is as follows: the elements from the gamma-ray lines are identified. In this scenario, the 662 keV ^{137}Cs line is not expected to be in the spectrum from the granite slab. Therefore, the 662 keV photopeak is used to produce an image that shows that there is a ^{137}Cs source above the detectors. The full-energy two-interaction events from

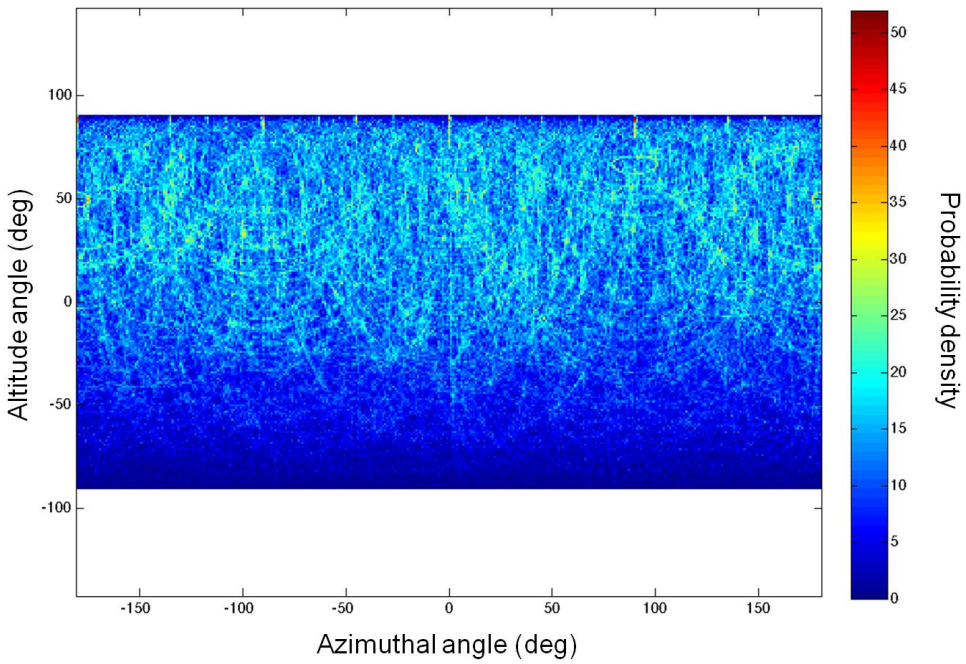

(a)

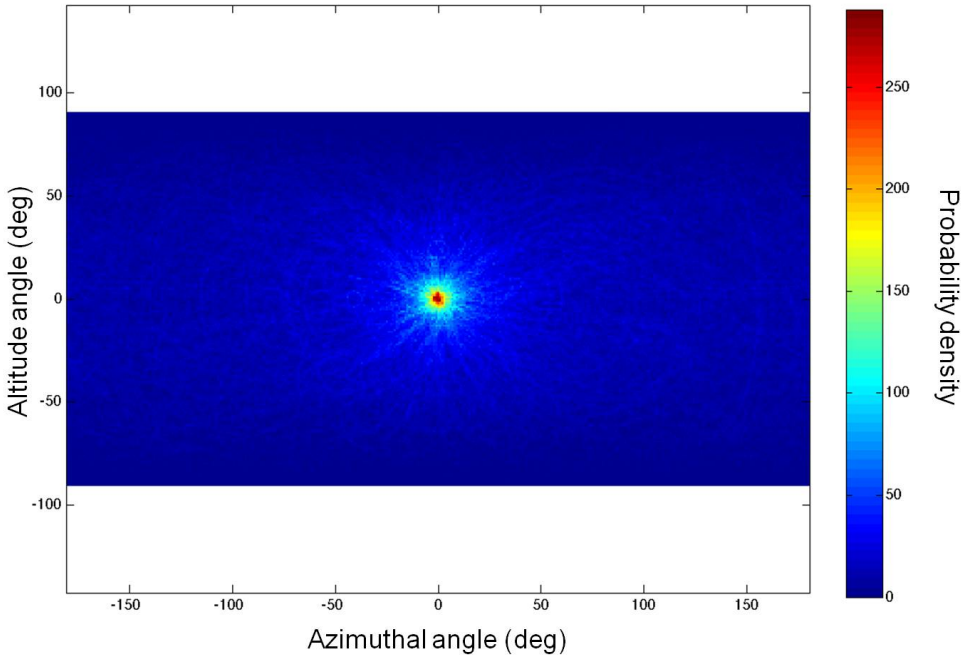

(b)

Figure 6.14: Simulated image produced using 662 keV full-energy two-interaction events. Figure 6.14(b) is the same image but the x-, y- and z-axis were rotated to place the source at the center of the image.

the photopeak are used to produce an image, as shown in Figure 6.14. From Figure 6.14(a), we can see that the source is at 90° on the polar angle of the detector which is why the point spread function is so wide. In Figure 6.14(b), we rotated the x- , y- and z-axis so that the source would be located at (0,0) in the image. The gamma rays that produce a ring contained within 16° of the center location (0,0), which is the angle at which 68% of the total number of counts is contained as defined in section 6.1.4, are coming from a source above the granite. They are therefore discarded from the summed spectrum (in red in Figure 6.14). The subtracted spectrum (in blue) can be seen in Figure 6.15. In order to see the improvement in the 662 keV photopeak, a zoom on the low energy part of the spectrum is shown in Figure 6.15(b). The y-axis is linear as opposed to the plot in Figure 6.15(a) where the scale is logarithmic. It is important to emphasize that using this technique, the gamma rays that undergo only a photoelectric process at 662 keV cannot be rejected because they are not imaged. To make further improvements in the sensitivity, the imaging ratio method was developed.

6.2.2 Imaging Ratio Method

The imaging ratio method uses the ratio of events originating from below the detector to those originating from above at a specific energy using the Compton imaging techniques with full-energy two-interaction events. Because the detector geometry is the same for all interaction types, then this ratio is also a measure of the ratio of all gamma rays originating from below to those originating from above for all interaction types. Therefore, once this ratio is measured, we multiply the total area under the 662 keV photopeak from the summed spectrum (including the background) by this ratio to obtain the number of counts of that peak that come from the gamma rays originating from below. In this work, we considered that the full-energy two-interaction events coming from above the detectors were within 16 degrees

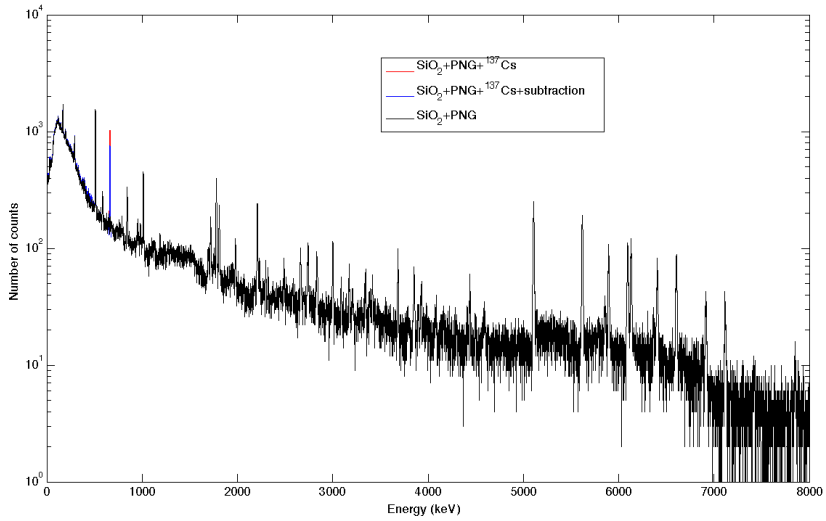

(a)

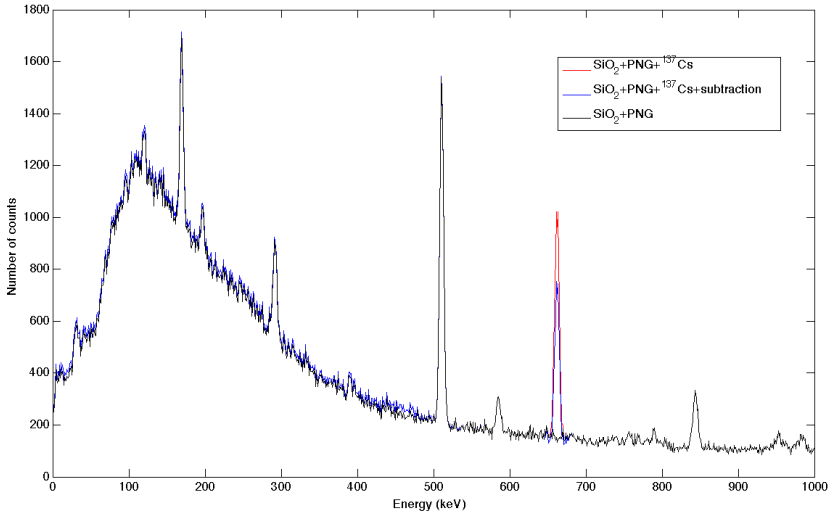

(b)

Figure 6.15: CdZnTe detector response to activated SiO_2, PNG and a source of ^{137}Cs. The figure shows the improvement in sensitivity that is achieved using Compton imaging techniques. Figure (b) is a zoom on the low energy part of the spectrum.

of the center location (0,0). If not within 16 degrees, the events were considered to be coming from below. The ratio of the events originating from below the detector to those originating from above is:

$$R = \frac{events\ originating\ from\ below\ the\ detector}{events\ originating\ from\ above\ the\ detector} = 0.46 \tag{6.16}$$

6.2.3 Analysis

In this analysis, we will show that the using the imaging ratio method, the area under the 662 keV peak can be reduced so that the amplitude given by the centroid at 662 keV is about 1 sigma above the noise. It will be demonstrated that the contribution of the downward-going-gamma rays can be eliminated so that the residual is consistent with fluctuations in the background.

In a gamma-ray spectrum, the continuum is produced from many sources, including the gamma rays that scatter from the lander or the rover. Therefore, in the analysis of gamma-ray spectra measured by the GRS, it is important to accurately establish the shape of the continuum so that the counts in the peaks above this continuum can be correctly determined [17]. The continuum under a peak is usually determined by assuming a slowly varying low-order polynomial fit to nearby energies that contain no peak [17]. In this analysis, we used the summed spectrum (in red in Figure 6.15) to fit a polynomial of degree 2 to the data. Figure 6.16 shows the polynomial fit to the data (blue line). In order to get the best fit to the background data, only the data points shown in red were used for the polynomial fit.

We then subtracted the counts below the background fit from both the summed spectrum and the subtraction spectrum that were shown in Figure 6.15 in red and blue, respectively. The data points that were negative were assumed to be 0 because they are physically not possible. Figure 6.17 shows the results of this background subtraction.

In order to quantify the sensitivity improvement of the full-energy Compton rejection method, we fit Gaussian functions to the data shown in Figure 6.17 and measured

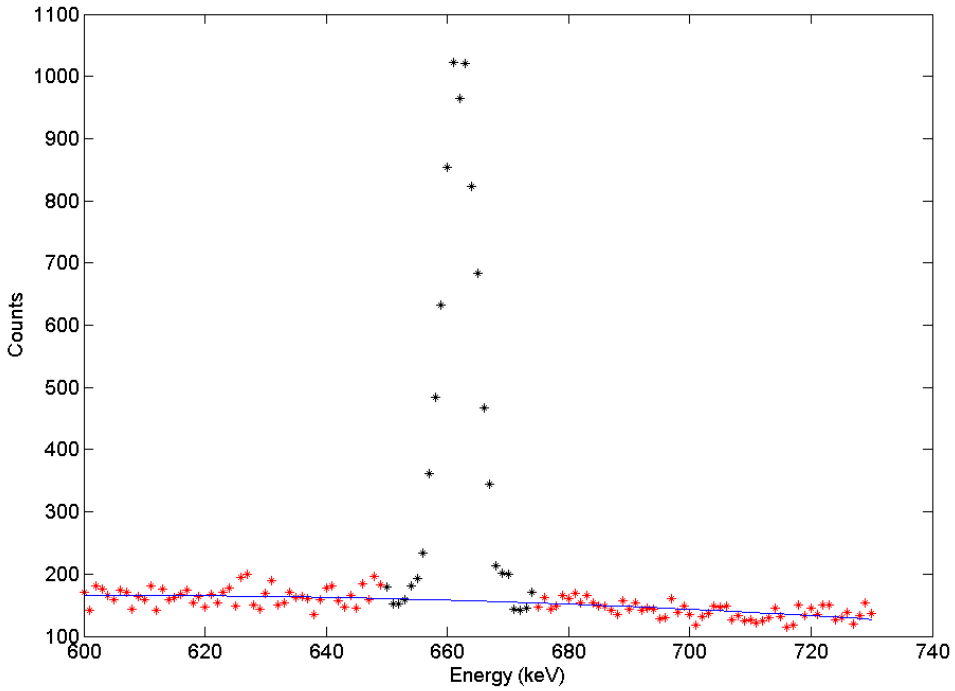

Figure 6.16: Second degree polynomial fit used to fit the data. To get the best fit to the background data points, only the data points shown in red were used.

the area under the peaks. From these Gaussian fits, the areas under the background subtracted peaks were obtained and from the polynomial fit of the background, the areas under the background fit was obtained. Table 6.1 summarizes these results.

Table 6.1: Area under the 662 keV photopeak (number of counts)

Summed spectrum	Subtraction spectrum	Background
6212	4091	4308

In order to make sense of the area under the background fit, we used the same energy interval that was used for the Compton image shown in Figure 6.14. The sum of the area under the summed spectrum Gaussian peak and the area under the background fit is about 10520 from Table 6.1. We multiplied this area by 0.46 which corresonds to the ratio measured in Equation 6.16. The background area was subtracted from the area obtained after multiplication because it represents the

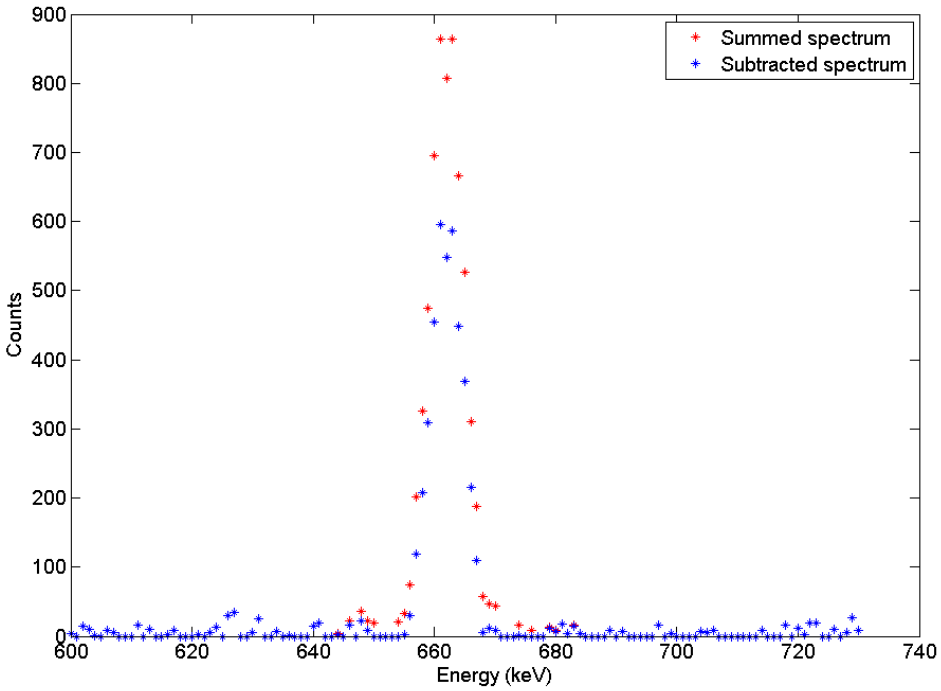

Figure 6.17: Background subtracted summed (red) and subtracted (blue) spectra.

sensitivity of the detectors to the ^{137}Cs from below using the imaging capabilities if we did not know that there was no cesium in the subsurface of the soil. We call that background subtracted area the 'residual' area. Table 6.2 shows the area estimates.

Table 6.2: Imaging ratio method area (number of counts)

Ratio × (Area under summed spectrum + Area under background)	'Residual' area
4816	508

We used this 'residual' area with the known centroid of 662 keV of ^{137}Cs (since it was identified) and the known FWHM at this energy to plot the Gaussian peak that it would represent. Figure 6.18 compares the Gaussian peak deduced from the 'residual' area to the Gaussian fits to both the summed spectrum and the subtracted spectrum. From this Figure, it is clear that the sensitivity of the detectors to the

^{137}Cs source placed above them has been significantly reduced.

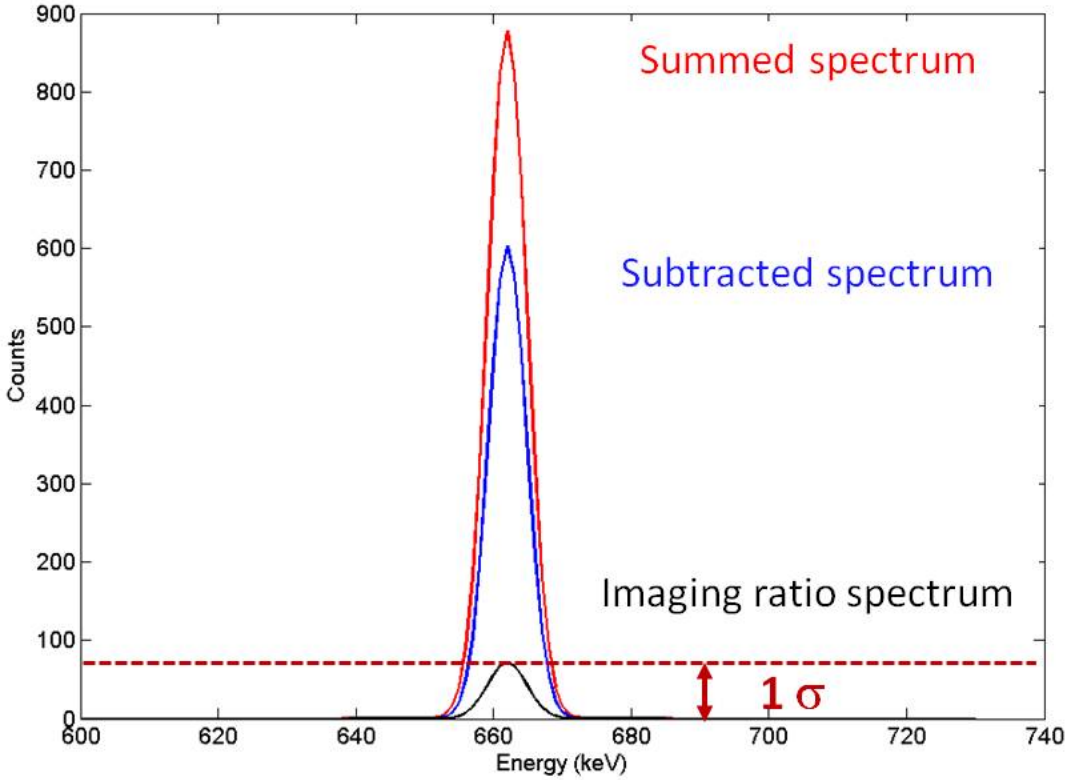

Figure 6.18: Gaussian functions from the summed spectrum fit (red), subtracted spectrum fit (blue) and deduced from the imaging ratio method 'residual' area.

Finally, the standard deviation σ_N on the area net counts N from the Gaussian peaks in Figure 6.18 is calculated as [27]:

$$\sigma_N = \sqrt{\sigma_T^2 + \sigma_B^2} = \sqrt{T + B} \tag{6.17}$$

where T is the total number of counts and B is the area under the background fit and σ_T and σ_B are their respective standard deviations. In this analysis, the total number of counts is the sum of the area under the Gaussian peak for each peak and the area under the background. Table 6.3 summarizes the net counts from the area under the Gaussian peak shown in Figure 6.18 and the associated uncertainties.

Table 6.3: Area under the Gaussian peaks and their uncertainty. The color refers to the Gaussian functions of Figure 6.18

	Red Gaussian (Summed spectrum)	Blue Gaussian (full-energy Compton rejection method)	Black Gaussian (imaging ratio method)
Net counts	6212 ± 122	4091 ± 112	508 ± 95
Uncertainty (%)	1.96	2.8	18.8

The amplitude given by the black Gaussian function at the centroid (662 keV) is 71.8± 13.5 counts. We have measured that σ_B is about 65 counts. Therefore, the amplitude at 662 keV given by the black gaussian is about 1 sigma above the noise. As a conclusion, the imaging ratio method has shown that the downward-going-gamma rays can be eliminated so that the residual is consistent with fluctuations in the background.

CHAPTER VII

Summary and Future Work

7.1 Summary

The Probing *In situ* with Neutrons and Gamma-rays (PING) instrument, developed at NASA Goddard Space Flight Center (GSFC) by the neutron/gamma-ray group, is a technology used to determine the subsurface elemental composition of a planet. It uses a pulsed neutron generator to excite the solid materials of a planet and measures the resulting neutron and gamma-ray emissions with its detector system. Using fast neutrons as an excitation source to probe the subsurface of a planetary body removes the need to drill into the solid surface. The neutron and gamma-ray detector system measures the energy distribution of the resulting neutrons and gamma rays. The energy distribution of the resulting neutrons is a measurement of the content of hydrogen. The energy of the resulting gamma rays is characteristic of each isotope with which the neutrons have interacted and the intensity of the gamma rays produced by nuclear reactions varies in proportion to the concentration of the elements and the flux of particles that cause the nuclear reactions. Therefore, the neutron and gamma-ray detector system on PING is a key to determining the elemental composition of a planet.

To enable low-cost missions, planetary science has a critical need for miniaturized instruments with *in situ* sensors that can be deployed on surface landers, rovers and

orbiting platforms. A key objective of NASA is to develop instruments with reduced mass, volume and power consumption. The NASA GSFC neutron/gamma-ray group is currently developing the Imaging Gamma-Ray Spectrometer (IGS), the next generation light and compact high resolution and sensitivity instrument on PING. The spectroscopic and imaging performance of pixelated CdZnTe detectors as the innovative technology for IGS were investigated. This technology gives IGS the advantages of low mass and low power imaging with large field of view and high-resolution spectroscopy. These advantages are obtained at room temperature thus eliminating

1) the need for a cryogenic cooler,

2) an anticoincidence shield to reduce the background, and

3) a collimator to reject secondary gamma rays originating from the spacecraft or environment.

Indeed, with their pixelated arrays, CdZnTe detectors can identify tracks left by charged particles and use Compton imaging techniques to distinguish gamma rays coming from above, from the spacecraft for example, to those coming from below, from the planet.

It is necessary for planetary exploration to detect elements such as oxygen. Neutron activation on oxygen results in the production of a 6.129 MeV gamma-ray line with 67% probability. In order to characterize and calibrate the IGS at this energy, which is a region where there is a lack of gamma-ray sources, we designed and built the NASA GSFC 6 MeV Gamma Facility. The facility uses neutron absorption on oxygen to provide a quasi-monoenergetic source of 2.742, 6.129 and 7.117 MeV gamma rays suitable for characterization and optimization of a wide range of gamma-ray instruments for planetary science and imaging telescopes for astrophysics. Comparison to a ^{238}Pu/^{13}C with similar 6.129 MeV gamma-ray rate shows that the 6 MeV Gamma Facility has a reduced low-energy gamma-ray continuum by a factor of 30 and a 6.129 MeV gamma-ray rate a 100 times higher.

The spectroscopic performance of a large volume single crystal pixelated CdZnTe detector was studied by designing a detector box to read out a large volume of the detector. The performance of the crystal showed a single pixel energy resolution of 1.4% FWHM at 662 keV. However, above 2 MeV, simulations have shown that the electron cloud form in the detector becomes larger than the size of the pixel of the detector. Using digital system processing to readout the system, it is possible to calibrate the adjacent pixels responsible for cross talk and correct for incomplete charge collection.

The Doppler effect, the energy and position resolution of pixelated CdZnTe detectors are contributing factors to the angular resolution of the detectors. It was shown that the position resolution is the main contributing factor to the angular resolution. Simulations have shown that with a pixel pitch of 1.72 mm, pixelated CdZnTe detectors have an angular resolution of 16° at 662 keV using backprojection reconstruction. A planetary science demonstration configuration was modeled and Compton imaging techniques were used to reject gamma rays from a source placed above the detectors using full-energy Compton rejection method and imaging ratio method. The second technique, the imaging ratio method, has shown that the gamma rays coming from the source placed above the detectors can be eliminated from the energy spectrum so that the residual is consistent with fluctuations in the background thus improving the sensitivity of the detectors to the gamma rays originating from the planet below.

As a conclusion, this work has shown that pixelated CdZnTe detectors have the advantages of high-resolution spectroscopic performance, room-temperature operation thus eliminating the need for a cryogenic cooler, and Compton imaging capabilities to reject secondary gamma rays originating from the spacecraft or environment. Simulations have demonstrated that it is possible to reject a significant fraction of the gamma rays coming from a point source above the detectors thus increasing the sensitivity of the measurement to the planet surface below. Therefore, an array of

pixelated CdZnTe detectors is a good candidate to meet the goals of reduced mass, volume and power consumption as imposed by the NASA requirements. However, the size of the electron cloud remains a problem at high energy and contributes to energy resolution degradation. In order to study the possibility of pixelated CdZnTe detectors at high energy, it is necessary to increase the detection volume of CdZnTe detectors. In the near future, we will receive an array of 2 × 2 pixelated CdZnTe detectors that we are going to

1) characterize using a monoenergetic beam of 6.129 MeV gamma rays at the 6 MeV Gamma Facility and

2) study at our test facility at GGAO in a planetary science demonstration configuration.

7.2 Future Work

The IGS has been successfully chosen to be funded by the NASA GSFC Internal Research and Development program. The work plan includes the purchase of hardware equipment for the IGS, the development of the NASA imaging code based on this work and background reduction experiments conducted at GGAO. The hardawre equipement for the IGS prototype will be purchase from H3D, Inc. [23]. Details of the IGS design and future experiments at GGAO are given in this section.

7.2.1 Instrument Design

The CdZnTe Detector Module (DM) is the smallest unit of this modular system. It consists of a single 2 cm × 2 cm × 1.5 cm CdZnTe crystal that is plugged into a small printed circuit board containing an ASIC. The ASIC produces analog energy and timing data for the single cathode and 121 anode signals. These DMs are in turn plugged into a Detector Array (DA) printed circuit board with four sockets to make a 2 × 2 array. A small PCB which filters HV noise, distributes the cathode

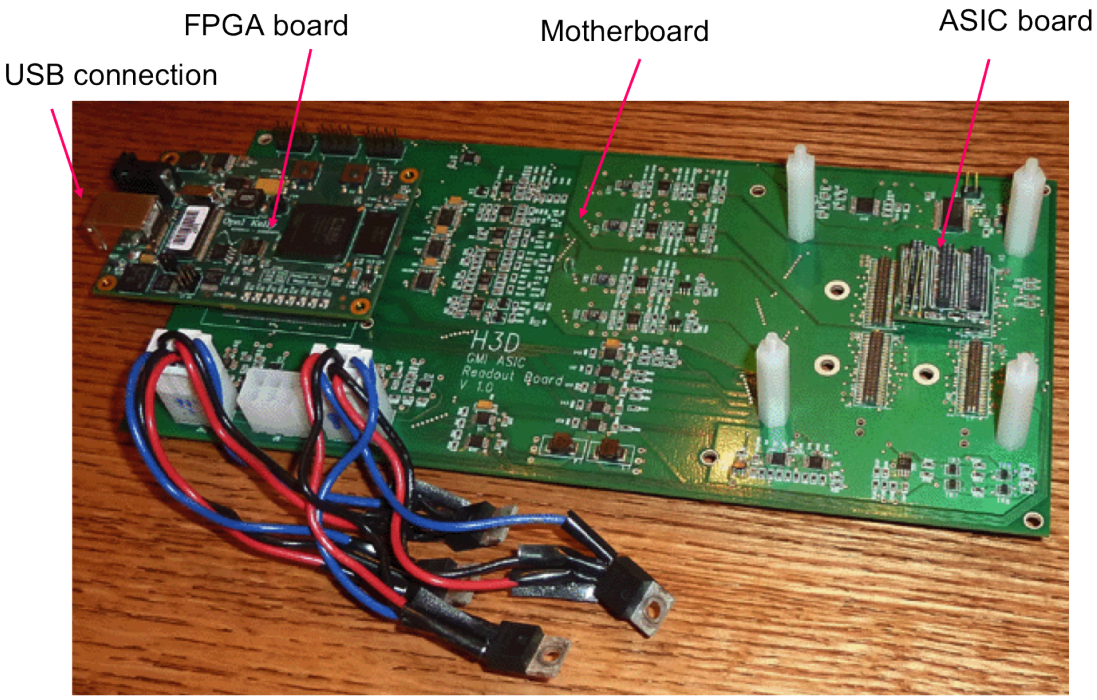

Figure 7.1: Photograph of the 2 × 2 CdZnTe array printed circuit board to be received. The printed circuit board includes the possibility to plug 2 CdZnTe detector/ASIC, a motherboard, an FPGA and a USB connection. The hardawre equipement for the IGS prototype will be purchase from H3D, Inc. [23].

and grid HV to the detectors and connect the cathode signal to the ASICs, sits above the detectors. In addition, an internal HV generator board generates the -3000V cathode bias and up to -200V grid bias for the four detectors. There is also a low-voltage power regulation board that does the filtering/isolation for the power rails of different system components. Finally, there is a FPGA card that directly plugs into the motherboard and provides USB 2.0 connection to a PC. The different printed circuit boards to receive are shown in Figures 7.1 and 7.2. The detector box and assembly of the boards will be designed at NASA after delivery of the boards.

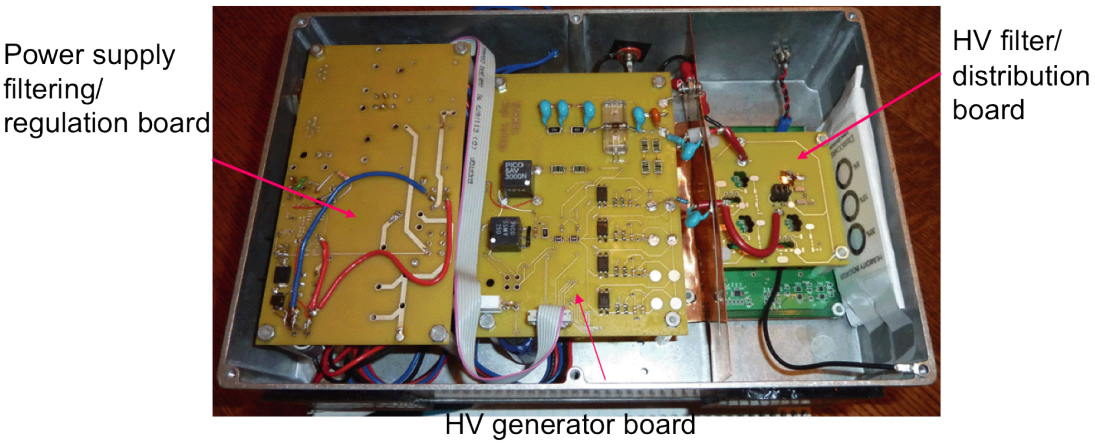

Figure 7.2: Photograph of the power supply/filtering/regualtion board, the HV filter distribution board and HV generator board to be received. The detector box and assembly of the boards will be designed at NASA after delivery of the boards. The hardware equipement for the IGS prototype will be purchased from H3D, Inc. [23].

7.2.2 Future Experiment

Once the IGS is assembled and fully functional, we will demonstrate its utility. First, radioactive sources of gamma rays will be used in the laboratory to both test the IGS imaging capabilities and to demonstrate high spectroscopic performance. Then, we will use IGS as part of our planetary science PING instrument where it will be used with the PNG at the GGAO facility. We will use the neutron-induced emission of characteristic gamma rays from materials to perform background rejection, extended source imaging and elemental composition mapping of granite and basalt blocks in the experimental configuration illustrated in Figure 7.3. In this figure, the IGS is situated on top of the basalt monument next to the PNG and underneath a structure that puts mass above the IGS. For planetary science applications, this configuration represents a neutron-gamma instrument measuring the composition of the material below, but using the IGS imaging capabilities to ignore the gamma rays coming from a rover structure above the PING gamma ray/neutron elemental composition instrument. The ability to differentiate between gamma rays coming from above from those coming

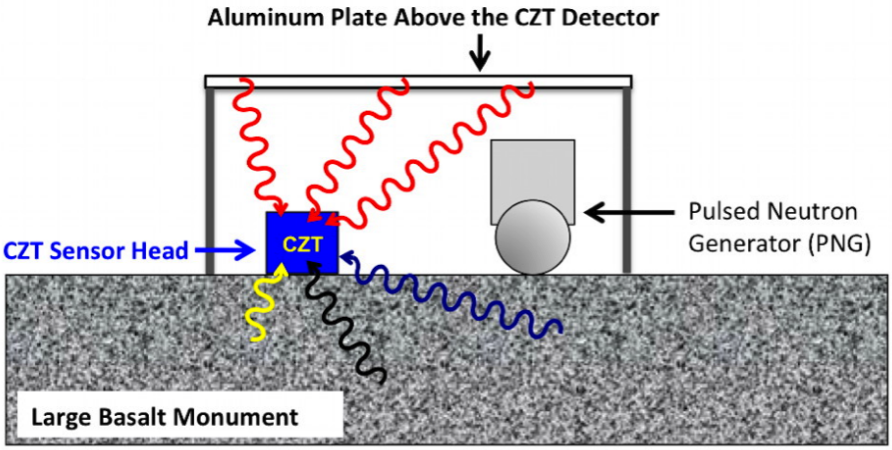

Figure 7.3: IGS used as the gamma-ray spectrometer as part of the PING instrument. Here IGS detects the characteristic gamma rays coming from elements that have been activated by the nearby pulsed neutron generator. The aluminum structure above the IGS CdZnTe detectors represents a planetary rover.

from below is extremely valuable for background reduction in these planetary science measurements. The imaging code to perform the background rejection will include the full-energy Compton rejection and the imaging ratio methods developed in this work.

APPENDICES

APPENDIX A

Differential Pair Production Cross Section: No Screening Effect

The differential pair production cross section without corrections for screening effect were calculated using the following equation [6]:

$$\phi(E_+)dE_+ = \frac{Z^2}{137} r_0^2 \frac{dE_+}{(h\nu)^3}(E_-^2 + E_+^2 + \frac{2}{3}E_-E_+)4(log\frac{2E_-E_+}{h\nu mc^2} - \frac{1}{2}) \qquad \text{(A.1)}$$

where E_+ and E_- are the kinetic energies of the positron and the electron, respectively. $h\nu$ is the energy of the initial photon, Z is the atomic number of the material, r_0 is the classical radius of the electron and mc^2 is the rest mass of the electron.

APPENDIX B

Differential Pair Production Cross Section: Screening Effect

The differential pair production cross section with corrections for screening effect were calculated using the following set of equations [5, 6]:

For complete screening (γ=0):

$$\phi(E_+)dE_+ = \frac{Z^2}{137}r_0^2\frac{dE_+}{(h\nu)^3}\left[(E_-^2 + E_+^2 + \frac{2}{3}E_-E_+)log(183Z^{-\frac{1}{3}}) + \frac{E_-E_+}{9}\right] \quad \text{(B.1)}$$

if $\gamma < 2$:

$$\phi(E_+)dE_+ = \frac{Z^2}{137}r_0^2\frac{dE_+}{(h\nu)^3}\left[(E_-^2 + E_+^2)(\phi_1(\gamma) - \frac{4}{3}log(Z)) + \frac{2}{3}E_-E_+(\phi_2(\gamma) - \frac{4}{3}log(Z))\right] \quad \text{(B.2)}$$

if γ is between 2 and 15:

$$\phi(E_+)dE_+ = \frac{Z^2}{137}r_0^2\frac{dE_+}{(h\nu)^2}(E_-^2 + E_+^2 + \frac{2}{3}E_-E_+)4(log\frac{2E_-E_+}{h\nu mc^2} - \frac{1}{2} - c(\gamma)) \quad \text{(B.3)}$$

if $\gamma \gg 1$ (no screening):

$$\phi(E_+)dE_+ = \frac{Z^2}{137} r_0^2 \frac{dE_+}{(h\nu)^3}(E_-^2 + E_+^2 + \frac{2}{3}E_-E_+)4(log\frac{2E_-E_+}{h\nu mc^2} - \frac{1}{2}) \tag{B.4}$$

where E_+ and E_- are the kinetic energies of the positron and the electron, respectively. $h\nu$ is the energy of the initial photon, Z is the atomic number of the material, r_0 is the classical radius of the electron and mc^2 is the rest mass of the electron. The function $\phi_1(\gamma)$, $\phi_2(\gamma)$ and c(γ) are shown in Figures B.1 and B.2, respectively.

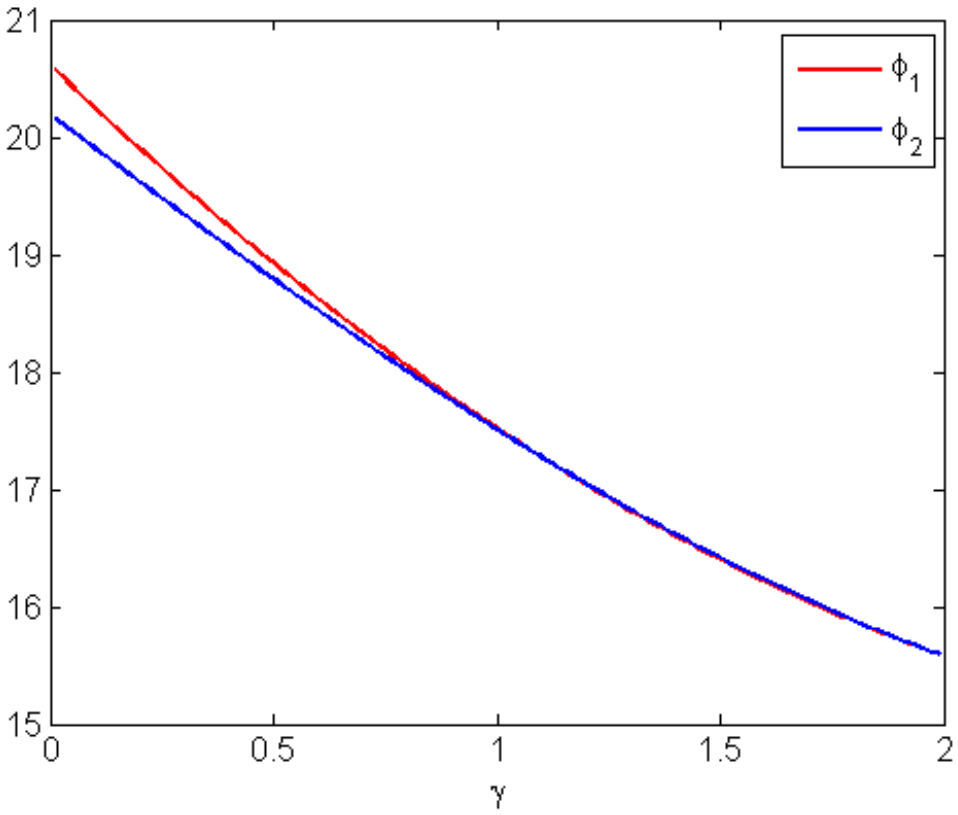

Figure B.1: $\phi_1(\gamma)$ and $\phi_2(\gamma)$ as functions of γ.

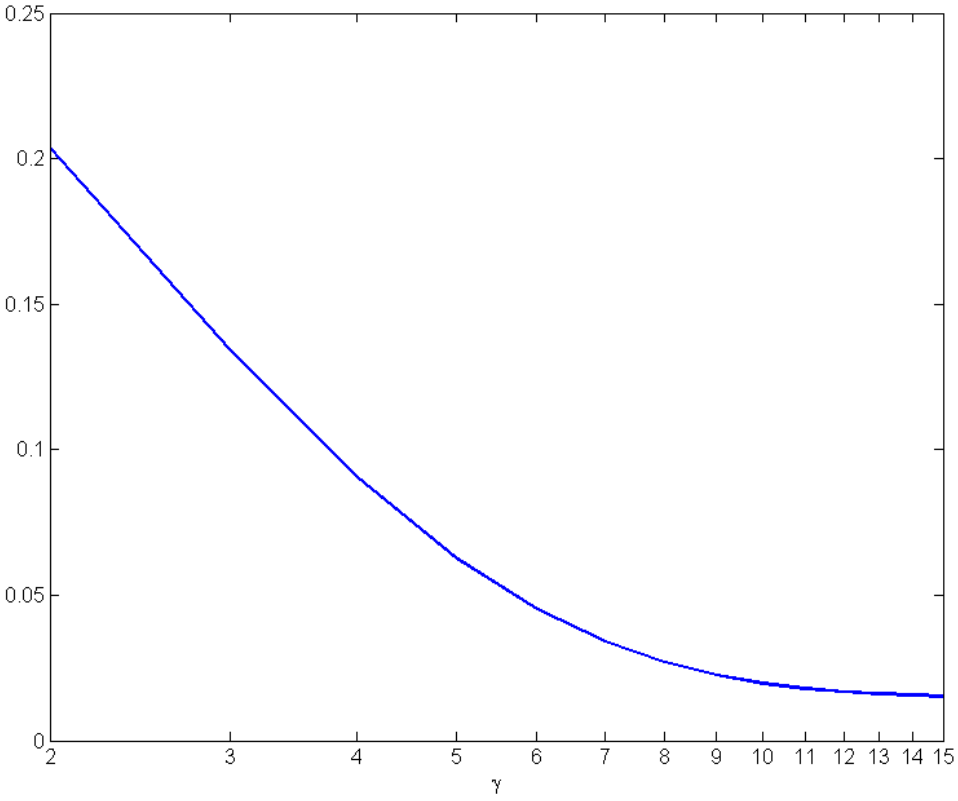

Figure B.2: c(γ) as function of γ.

APPENDIX C

Differential Pair Production Cross Section: Exact Calculations

The exact formulation used to calculate the differential pair production cross section at low energies follows [6]:

$$\begin{aligned}\phi(E_-)dE_- &= \frac{Z^2}{137}r_0^2 p_- p_+ \frac{dE_+}{k^3}\left\{-\frac{4}{3} - 2E_-E_+\frac{p_-^2+p_+^2}{p_-^2p_+^2}\right. \\ &+\mu^2\left(\frac{\epsilon_-E_+}{p_-^3}+\frac{\epsilon_+E_-}{p_+^3}+\frac{\epsilon_-\epsilon_+}{p_-p_+}\right)+\left[\frac{k^2}{p_-^3p_+^3}(E_-^2E_+^2+p_-^2p_+^2)-\frac{8}{3}\frac{E_-E_+}{p_-p_+}\right]L \\ &\left.-\frac{\mu^2k}{2p_-p_+}\left[\frac{E_-E_+-p_-^2}{p_-^3}\epsilon_-+\frac{E_-E_+-p_+^2}{p_+^3}\epsilon_++\frac{2kE_-E_+}{p_-^2p_+^2}\right]L\right\}\end{aligned}$$

with

$$\epsilon_+ = 2log\frac{E_++p_+}{\mu} \quad \epsilon_- = 2log\frac{E_-+p_-}{\mu} \quad L = 2log\frac{E_-E_++p_-p_++\mu^2}{\mu k}$$

where E_+ and E_-, p_+ and p_- are the kinetic energies and momentums of the positron and the electron, respectively. $k{=}h\nu$ is the energy of the initial photon, Z is the atomic number of the material, r_0 is the classical radius of the electron and $\mu{=}mc^2$ is the rest mass of the electron.

BIBLIOGRAPHY

BIBLIOGRAPHY

[1] Anderson, S. (2011), Event Classification for 3-D Position Sensitive Semiconductor Detectors, Ph.D. thesis, University of Michigan.

[2] Ansys, Inc. (2012), Ansys Maxwell, http://www.ansys.com.

[3] Avneet, S., and X-5 Monte Carlo Team (2005), Doppler Energy Broadening for Incoherent Scattering in MCNP5, *Doc. LA-UR-04-0487*.

[4] Barthelmy, S., et al. (2005), The Burst Alert Telescope (BAT) on the SWIFT Midex Mission, *Space Science Reviews*, *120*, 143–164.

[5] Bethe, H. (1934), The Influence of Screening on the Creation and Stopping of Electrons, *Mathematical Proceedings of the Cambridge Philosophical Society*, *30*, 525–539.

[6] Bethe, H., and W. Heitler (1934), On the Stopping of Fast Particles and on the Creation of Positive Electrons, *Proceedings of the Royal Society of London. Series A, Containing Papers of a Mathematical and Physical Character*, *146*, 83–112.

[7] Bhattacharya, D., T. O'Neill, A. Akyuz, J. Samimic, and A. Zych (2009), Prototype TIGRE Compton Gamma-Ray Balloon-Borne Telescope, *New Astronomy Reviews*, *48*, 287–292.

[8] Biggs, F., L. Mendelsohn, and J. Mann (1975), Hartree-Fock Compton profiles for the elements, *Atomic Data and Nuclear Data Tables*, *16*, 201–309.

[9] Bodnarik, J., L. Evans, S. Floyd, L. Lim, T. McClanahan, M. Namkung, A. Parsons, J. Schweitzer, and J. Trombka (2010), A Unique Outside Neutron and Gamma Ray Instrumentation Development Test Facility at NASA's Goddard Space Flight Center, *Proceeding 41st Lunar and Planetary Science Conference*, pp. 2581–2583.

[10] Brookhaven National Laboratory (2012), Evaluated nuclear data file (endf), http://www.nndc.bnl.gov/exfor/endf00.jsp.

[11] Brookhaven National Laboratory (2012), National nuclear data center, http://www.nndc.bnl.gov.

[12] Brusa, D., G. Stutz, J. Riveros, J. Fernandez-Varea, and F. Salvat (1996), Fast sampling algorithm for the simulation of photon Compton scattering, *Nuclear Instruments and Methods in Physics Research Section A379*, *379*, 167–175.

[13] Cesareo, R. (1992), Interaction of keV photons with matter and new applications, *Physics Report*, *213*, 117.

[14] DynamicSignals LLD, Inc. (2012), Gage, http://www.gage-applied.com/.

[15] Endicott Interconnect Technologies, Inc. (2012), http://www.evmicroelectronics.com/czt.html.

[16] Endicott Interconnect Technologies, Inc. (2012), Single Charge-Sensitive Hybrid Preamplifiers, http://www.evmicroelectronics.com/ev509.html.

[17] Evans, L., R. Reedy, R. Starr, K. Kerry, and W. Boynton (2006), Analysis of gamma ray spectra measured by Mars Odyssey, *Journal of Geophysical Research: Planets (1991-2012)*, *111*.

[18] Evans, R. D. (1982), *The Atomic Nucleus*, 695-701 pp., Krieger, New York.

[19] Feldman, W., B. Barraclough, K. Fuller, D. Lawrence, S. Maurice, M. Miller, T. Prettyman, and A. Binder (1999), The Lunar Prospector gamma-ray and neutron spectrometers, *Nuclear Instruments and Methods in Physics Research A 422*, pp. 562–566.

[20] Fermi/LAT Collaboration (2004), The Large Area Telescope on the Fermi Gamma-ray Space Telescope Mission, *The Astrophysical Journal*, *697*, 1071–1102.

[21] Gamma Medica, Inc. (2012), Gamma Medica, http://www.gammamedica.com/.

[22] Grau, J., J. Schweitzer, J. Draxler, and J. Lauterjung (1993), Elemental Logging in the KTB Pilot Hole. 1: NaI-based Spectrometry, *Nuclear geophysics : a journal of nuclear techniques in the earth and environmental sciences, minerals exploration, mining and process control*, *7*, 173–187.

[23] H3D, Inc. (2012), H3D, http://www.h3dgamma.com/.

[24] He, Z. (2000), Review of the Shockley-Ramo theorem and its application in semiconductor gamma-ray detectors, *Nuclear Instruments and Methods in Physics Research A*, *463*, 250–267.

[25] Hunter, S. D., et al. (2012), Development of a telescope for medium-energy gamma-ray astronomy, *Proceedings of SPIE*, pp. 873–880.

[26] Knoll, G. F. (2000), *Radiation Detection and Measurement*, 3rd ed., 417 pp., John Wiley & Sons, United States of America.

[27] Knoll, G. F. (2000), *Radiation Detection and Measurement*, 3rd ed., 87-88 pp., John Wiley & Sons, United States of America.

[28] Kroupa, M., et al. (2011), Wide energy range gamma-ray calibration source, *Journal of Instrumentation*, pp. 298–301.

[29] Mitrofanov, I., et al. (2010), Hydrogen Mapping of the Lunar South Pole Using the LRO Neutron Detector Experiment LEND, *Science Magazine*, *330*, 483–486.

[30] National Institute of Standards and Technology (2012), Xcom: Photon cross sections database, http://www.nist.gov/pml/data/xcom accessed.

[31] Niemel, A., and H. Sipila (1994), Evaluation of CdZnTe detectors for soft x-ray applications, *IEEE Transactions on Nuclear Science*, *41*, 1054–1057.

[32] Nowicki, S., S. Hunter, and A. Parsons (2012), Development of a quasi-monoenergetic 6 MeV Gamma Facility at NASA Goddard Space Flight Center, *Nuclear Instruments and Methods in Physics Research A*, *705*, 111–116.

[33] Padovani, E., and S. Pozzi (2005), MCNP-PoliMi ver. 1.0 User's Manual, *Library of Nuclear Engineering Department Politecnico di Milano Via Ponzio 34/3*.

[34] Parsons, A., et al. (2011), Active Neutrona and Gamma-Ray Instrumentation for In Situ Planetary Science Applications, *Nuclear Instruments and Methods in Physics Research A*, *652*, 674–679.

[35] Pelowitz, D. (2008), MCNPX User's Manual, *Doc. LA-CP-07-1473*.

[36] Ramo, S. (1939), Currents induced by electron motion, *Proceedings of the I.R.E.*, pp. 584–585.

[37] Spieler, H. (2005), *Semiconductor Detector Systems*, 339 pp., Oxford University Press, New York, NY.

[38] The MathWorks, Inc. (2010), Matlab, http://www.mathworks.com/products/matlab/.

[39] Vourvopoulos, G., and P. Womble (2001), Pulsed Fast/Thermal Neutron Analysis: a Technique for Explosives Detection, *Talanta*, *54*, 459–468.

[40] WaveMetrics, Inc. (2012), Igor pro software v.6.22a, http://www.wavemetrics.com.

[41] X-5 Monte Carlo Team (2005), MCNP A General Monte Carlo N-Particle Transport Code, *Doc. LA-UR-03-1987*.

[42] Xu, D. (2006), Gamma-ray Imaging and Polarization measurement using 3-D position-sensitive CdZnTe detectors, Ph.D. thesis, University of Michigan.